Narodowe Centrum Badań Jądrowych
National Centre for Nuclear Research
ŚWIERK

Ewelina Kucal

Doctoral Thesis

Modeling of neutron radiation damage in ceramic construction materials for the Dual Fluid Reactor using heavy ions

A thesis submitted in fulfilment of the requirements
for the degree of Doctor of Physical Sciences
in the National Centre for Nuclear Research

Supervisor:
prof. dr hab. Konrad Czerski
Auxiliary supervisor:
dr Cyprian Mieszczyński

Warsaw 2023

Acknowledgments

First of all, I would like to thank Prof. Konrad Czerski for his scientific supervision, patience, and support during the work on this doctoral thesis. Furthermore, I would like to thank my auxiliary supervisor, Dr. Cyprian Mieszczyński for his valuable comments and help.

I would also like to sincerely thank Dr. Przemysław Jóźwik and Dr. Renata Ratajczak for their support in my experimental work. Gratitude is also owed to Dr. Shavkat Akhmadaliev and Dr. Rene Heller for assistance in experimental part of this work. I would also like to acknowledge Prof. Christian Dufour and Prof. Marcel Touldemonde for hosting me in ENSICAEN in France, for sharing knowledge and experience.

Gratitude is also owed to Prof. Mariusz Dąbrowski and Dr. Karol Kowal for initiating and supervising the PhD4GEN project. I would like to extend my gratitude to my colleagues from the PhD4GEN group for their support, sharing of challenges, and experiences. Special thanks are due to Mateusz and Tomasz for their valuable advice in programming and in general software-related matters. I would like to thank all UZ3 people and everyone with whom I collaborated during my PhD for being helpful in many areas.

I would like to thank my mother and sister for their constant support and belief in me throughout my entire life. I would like to express my gratitude to my friends for their support and motivation during the writing of this paper.

Abstract

The Dual Fluid Reactor (DFR) is a new concept of a high-temperature reactor using fast neutrons. In the DFR, both the fuel and the coolant are liquid. As a fuel, molten salts or liquid metals are considered, while lead or lead-bismuth may be used as coolants. DFR is extremely economical due to its high power density, and thanks to its high efficiency, DFR can reduce the production prices of electricity, industrial heat and hydrogen. Construction materials for DFR must be resistant to very high temperatures, corrosion and radiation, which is why ceramic materials such as silicon carbide, zirconium carbide and titanium carbide are considered. Investigating new materials for use in the nuclear industry is time-consuming and very expensive due to neutron irradiation in the reactor. It is possible to use heavy ions instead of neutrons to study radiation damage. In this way, the exposure time is reduced from dozens of years to a few days.

This work focuses on examining the possibility of using ions as a surrogate for neutron radiation damage in silicon carbide. Despite the fact that the impact of radiation on this material has been the subject of research since the mid-last century, not everything is fully understood yet. As ions pass through the matter, they lose their energy through collisions with atoms or through interactions with electrons leading to ionization and excitation. At low energies, nuclear losses dominate, and at high energies, electronic losses prevail. Electronic energy loss may lead to a significant increase in temperature in the ion path, resulting in local melting and amorphization or annealing of defects. For intermediate energies (ranging from several hundred keV to several tens of MeV), a coupling of nuclear and electronic energy loss effects can be expected. Additionally, swift heavy ions can produce in the target material ion tracks leading to local melting and changes of the crystal structure, which can be described within a thermal spike model. The aim of this work is to improve the understanding of ion radiation damage formation in SiC, precisely in this energy range.

The basis of the research was an experiment involving the bombardment of a single crystal of silicon carbide with Si and C ions of different energies to obtain various number of crystal defects at different stopping power values. Both the case when the ion energies are very low and nuclear losses dominate, as well as the case when the ion has high energies and electronic losses dominate, were considered. The number of crystal defects and their depth distributions were experimentally determined using the Rutherford backscattering spectrometry in channeling mode and compared with Monte Carlo simulations performed applying the McChasy code. The effect of the deposited energy in silicon carbide samples was investigated through calculations based on both the thermal spike model and a molecular dynamics approach. The results showed that electronic energy deposition can heat the centre of the ion path and repair crystal lattice defects. This effect was also confirmed experimentally by externally heating the targets during irradiation and annealing the targets after irradiation, supporting the use of SiC ceramics as a construction material for future high-temperature nuclear reactors.

Streszczenie

Reaktor Dwupłynowy (ang. Dual Fluid Reactor - DFR) jest nową koncepcją reaktora wysokotemperaturowego wykorzystującego prędkie neutrony. W DFR zarówno paliwo, jak i chłodziwo, są płynne. Jako paliwo brane są pod uwagę stopione sole lub ciekły metal, natomiast chłodziwem może być ołów lub ołów z bizmutem. DFR jest niezwykle ekonomiczny ze względu na dużą gęstość mocy, a dzięki swojej wysokiej efektywności może zredukować ceny produkcji energii elektrycznej, ciepła przemysłowego oraz wodoru. Materiały konstrukcyjne dla DFR muszą być odporne na bardzo wysokie temperatury, korozję oraz promieniowanie, dlatego brane są pod uwagę materiały ceramiczne takie jak węglik krzemu, węglik cyrkonu oraz węglik tytanu. Badania nowych materiałów dla przemysłu jądrowego zajmują bardzo dużo czasu i są bardzo kosztowne, ze względu na napromieniowanie neutronami w reaktorze. Do badania zniszczeń radiacyjnych możliwe jest jednak użycie ciężkich jonów zamiast neutronów. W ten sposób redukuje się czas napromieniowania z dziesiątek lat do kilku dni.

Niniejsza praca skupia się na zbadaniu możliwości wykorzystania jonów do symulacji uszkodzeń spowodowanych promieniowaniem neutronowym w węgliku krzemu. Pomimo, że wpływ promieniowania na ten materiał jest przedmiotem badan od połowy zeszłego stulecia, to wciąż nie wszystko jest w pełni zrozumiane. Podczas przejścia przez materiał, jony tracą swoją energię przez kolizje z atomami lub przez jonizację i ekscytację elektronów. W przypadku niskich energii jonów dominują straty jądrowe, a przy wysokich energiach straty elektronowe. Dla energii pośrednich (w zakresie od kilkuset keV do kilkudziesięciu MeV) można spodziewać się wzajemnego oddziaływania efektów strat jądrowych i elektronowych. Dodatkowo szybkie, ciężkie jony mogą wytwarzać w materiale docelowym ścieżki jonowe, poprzez lokalne stopnienie i zmiany w strukturze krystalicznej, co może być wyjaśnione za pomocą modelu ‘thermal spike’. Celem tej pracy jest lepsze zrozumienie skutków promieniowania jonowego w SiC właśnie w tym zakresie energii.

Podstawę przeprowadzonych badań stanowił eksperyment związany z naświetlaniem węglika krzemu jonami Si oraz C o rożnych energiach (dla uzyskania rożnych wartości strat elektronowych). Rozważono zarówno przypadek, gdy energie jonu są bardzo niskie i dominują straty jądrowe, a także gdy jon ma wysokie energie i dominujące są straty elektronowe. Liczbę defektów i ich rozkłady głębokościowe wyznaczono eksperymentalnie za pomocą spektrometrii rozpraszania wstecznego jonów w trybie kanałowania (RBS/C) i porównanie z symulacjami Monte Carlo wykonanymi przy użyciu kodu McChasy’ego. Wpływ strat elektronowych w węgliku krzemu zbadano za pomocą obliczeń opartych zarówno na modelu ’thermal spike’, jak i poprzez symulacje dynamiki molekularnej. Wyniki pokazały, że straty elektronowe mogą doprowadzić do podgrzania ścieżki jonów i naprawić defekty sieci krystalicznej. Efekt ten potwierdzono również eksperymentalnie poprzez przeprowadzenie naświetlań w wysokiej temperaturze oraz wygrzanie węglika krzemu po napromieniowaniu, co jednocześnie sprzyja zastosowaniu SiC jako materiału konstrukcyjnego przyszłych wysokotemperaturowych reaktorów jądrowych.

Contents

Chapter 1

Introduction

1.1 Motivation

Nowadays, power engineering plays an important role in human life and has a huge impact on its quality. Currently, the world's largest amount of electricity is produced from fossil fuels. The global path to achieve net-zero emissions by 2050 requires significant changes in energy production. Nuclear energy is one of the most important inventions for generating large amounts of energy and allows for electrical energy production in an effective way with an emission-free manner. Moreover, the high-temperature reactors currently being developed may increase the efficiency of energy production and also make nuclear power an ideal source of industrial heat.

An important aspect in the development of new technological solutions for nuclear reactors (especially high-temperature ones) is novel high-temperature materials. With the development of science and industry, the availability of materials, as well as knowledge about them, increases. Since the conditions in nuclear reactors are considered extreme: high temperature, possible corrosion and exposure to radiation, the construction materials of nuclear reactors must meet a number of requirements. When new materials are introduced to the nuclear industry, they must be properly tested to ensure that they will withstand these conditions throughout the operational life of the reactor. One property that is quite demanding to study is resistance to neutron radiation, which is time- and capital-intensive. This requires appropriate infrastructure, and the need to place samples in the reactor and carry out appropriate procedures after their removal. Therefore, one of the proposals is the possibility of replacing neutron radiation with ionic radiation in order to simulate material defects. This raises the question of similarities and differences in defects caused by both types of radiation. In the case of neutron radiation, impurities resulting from transmutation may be an important aspect, while ionic radiation is charged and can deposit the energy into electrons, causing the material to anneal.

Dual Fluid Reactor (DFR) is a novel concept of a very high-temperature reactor distinguished by its high efficiency [1] [2] [3]. It is a fast nuclear reactor with liquid fuel and liquid coolant. The DFR reactor is like a heat exchanger with many pipes inside to separate the flow of fuel and coolant. As a simplified construction compared to other nuclear reactors (e.g. no fuel cladding), DFR needs less construction material. However, these materials must be resistant to the extreme environment inside the core with high radiation, corrosion and high temperatures. Due to the reduction in construction materials, still it is economical to use expensive materials. For DFR promising materials are ceramics such as SiC, TiC and ZrC [4].

Silicon Carbide (SiC) is a promising material for high-temperature reactors [5] [4]. SiC is a high-temperature resistant material, that does not corrode easily and can be used in a radiation environment. Although, radiation effects in SiC have been investigated since the middle of the last century still are some not solved questions. The effects of nuclear stopping power and electronic stopping power in SiC during ion irradiation are well known separately, but the coupling effects of both, nuclear and electronic stopping power are currently under intensive study [6] [7]. Electronic stopping power due to significant temperature increase in ion path may lead to melting or phase change in material, as well as to annealing. Thus, the repair of the crystal lattice can occur. The explanation of this is the thermal spike model [8] [9]. The previous research suggested that threshold energy for ionization-induced annealing in SiC is equal to $1\,\mathrm{keV\,nm^{-1}}$ [10]. This shows that in the case of intermediate energy ions (a few hundred keV to a few tens MeV) in SiC effects of electron stopping cannot be neglected and may be important in the prediction of radiation damage of nuclear materials. Therefore, it seems very important to study the ionization-induced annealing mechanism during intermediate energies ion irradiation of SiC.

1.2 Research hypothesis and the main objectives

The central theme of this research revolves around the fundamental proposition that ions can be used for simulating the effects of neutron-induced radiation on materials. The hypothesis was verified by calculations based on theoretical models and experimentally. The limitations of using ions to surrogate neutrons were pointed out in the thesis. The main point of the work is to focus on the differences between the interaction of ions and neutrons with ceramics, with particular emphasis on research on the impact of ionization on the formation of radiation damage or repair of the crystal lattice.

1.3 Thesis outline

The introductory chapter provides the motivation, hypothesis and objectives of the thesis. The theoretical chapters of this thesis are Chapter 2 and Chapter 3. Chapter 2 describes the materials challenges for nuclear reactors, while Chapter 3 expounds upon the foundational theoretical background concerning radiation-induced damage. The research was conducted using calculations as well as experiments. The computational part has been described in Chapter 4. The SRIM code was used to calculate ion range, nuclear and electronic stopping power and damage dose. This calculation was necessary to plan the experiment. To understand the experimental results, a thermal spike model was used to predict the possible temperature increase at the centre of the ion path. Molecular Dynamics simulations were performed for the predictions of the effects of ion irradiation in the lattice dynamics and described in Chapter 4. The performed experiments with Si and C irradiation of SiC are described in Chapter 5. The discussion of results and conclusions have been presented in the final two chapters.

Chapter 2

Materials challenges for nuclear industry

2.1 Development of nuclear reactors

In the distant past, the atom was considered as an indivisible particle. Experiments performed about 120 years ago showed that the atom is composed of electrons and a nucleus that consists of protons and neutrons. In 1938, Otto Hahn, Lise Meitner and Fritz Strassmann recognized that a Uranium atom can split after being bombarded by a neutron. During this nuclear reaction, significant energy is emitted. The first human-made nuclear reactor, Chicago-Pile, started to operate a few years after the discovery of uranium fission in Chicago (United States). Chicago-Pile was made of pure graphite bricks with uranium pellets. The main role of this device was the production of fission isotopes to create a nuclear bomb, an important device during the time of World War II. After the war, the development of peace application of fission reaction began. In 1951,EBR-1 as the first nuclear reactor produced electricity, and powered four light bulbs [11]. In 1954, the first nuclear power plant (the Obinsk Nuclear Power Plant) was connected to the grid [12]. In 2023 about 410 nuclear power reactors operate in the whole world with the energy production of about 370 GWh, which is approximately 10 % of global energy production [13]. Current operating nuclear power plants are focused on electricity production. From a technical point of view, a nuclear reactor can play the role of a boiler that produces steam and later on this steam can be sent to the turbine to move the generator and produce electricity. The most popular in-use type of nuclear power plant is Pressurised Water Reactor (PWR) [14]. In addition to this, a variety of technological solutions for nuclear power plants are available.

Nuclear Power Plant types are divided into 'generations' that describe the development of the technology. The timeline of nuclear power plants is shown in Fig.2.1. Early

prototypes of nuclear power plants from the 50s and 60s are the first generation. The evolution of the first generation that can be used on a commercial scale gives a second generation with PWR and Boiling Water Reactor (BWR) reactors and is up to 90s. In the next years, the development and advancement of projects offer generation III and III+, which are huge power plants for electricity production. Over the past decade, interest has been put into generation IV of nuclear reactors, which is a new class of advanced nuclear power plants with high temperatures inside. Higher temperatures in the core increase the efficiency of power plant operation and also enables to production of industrial heat.

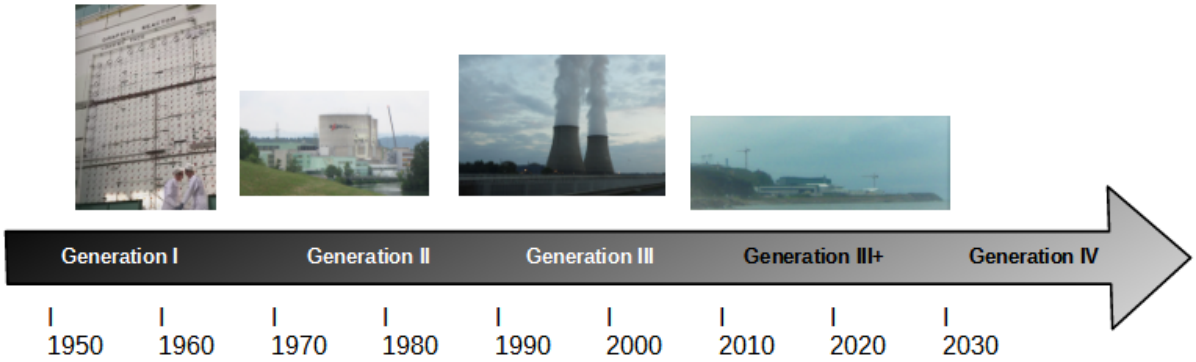

Figure 2.1: The Evolution of nuclear power on timeline. The images above the axis depict of reactor evolution in photos (from left: X-10 Graphite Reactor, Beznau Nuclear Power Plant, Belleville Nuclear Power Plant, EPR workplace).

The Generation IV of nuclear reactors (Gen IV reactors) consists of six technologies selected by the Generation IV International Forum (GIF) as the most promising. These include: Gas-cooled Fast Reactor (GFR), Lead-cooled Fast Reactor (LFR), Molten Salt Reactor (MSR), Supercritical Water-cooled Reactor (SCWR), Sodium-cooled Fast Reactor (SFR) and Very High Temperature Reactor (VHTR) [15]. A summary of the design of Gen IV reactors is presented in Tab. 2.1 and in Fig. 2.2. Each of these reactors differs from the others in terms of technological solutions, but all of them use fuel more efficiently than current operating nuclear power plants, reduce waste production, are safe and economically competitive, proliferation resistant and have physical protection.

Recently, a subject of active interest alongside HTRs are Small Module Reactors (SMRs). SMR is a nuclear reactor with an operational power of up to 300 MW (small) that can be produced in a factory (as a modular). Manufacturing in a factory reduces the cost and time of production. SMR due to its small size can be placed where large nuclear power plants are not suitable. The design of SMR is simplified in comparison with large nuclear power plants and relies most on passive safety systems.

In Poland, the history of the development of nuclear reactors is over 65 years old

Table 2.1: Summary of the design of Generation IV reactors [15]

Type	Neutron Spectrum	Coolant	Outlet Temperature [^oC]
GFR	fast	He / CO_2	850
LFR	fast	Pb / Pb-Bi	550 - 800
MSR	thermal/fast	Fluoride or chloride salts	700 - 850
SCWR	thermal/fast	H_2O	510
SFR	fast	Na	530 - 550
VHTR	thermal	He	1000

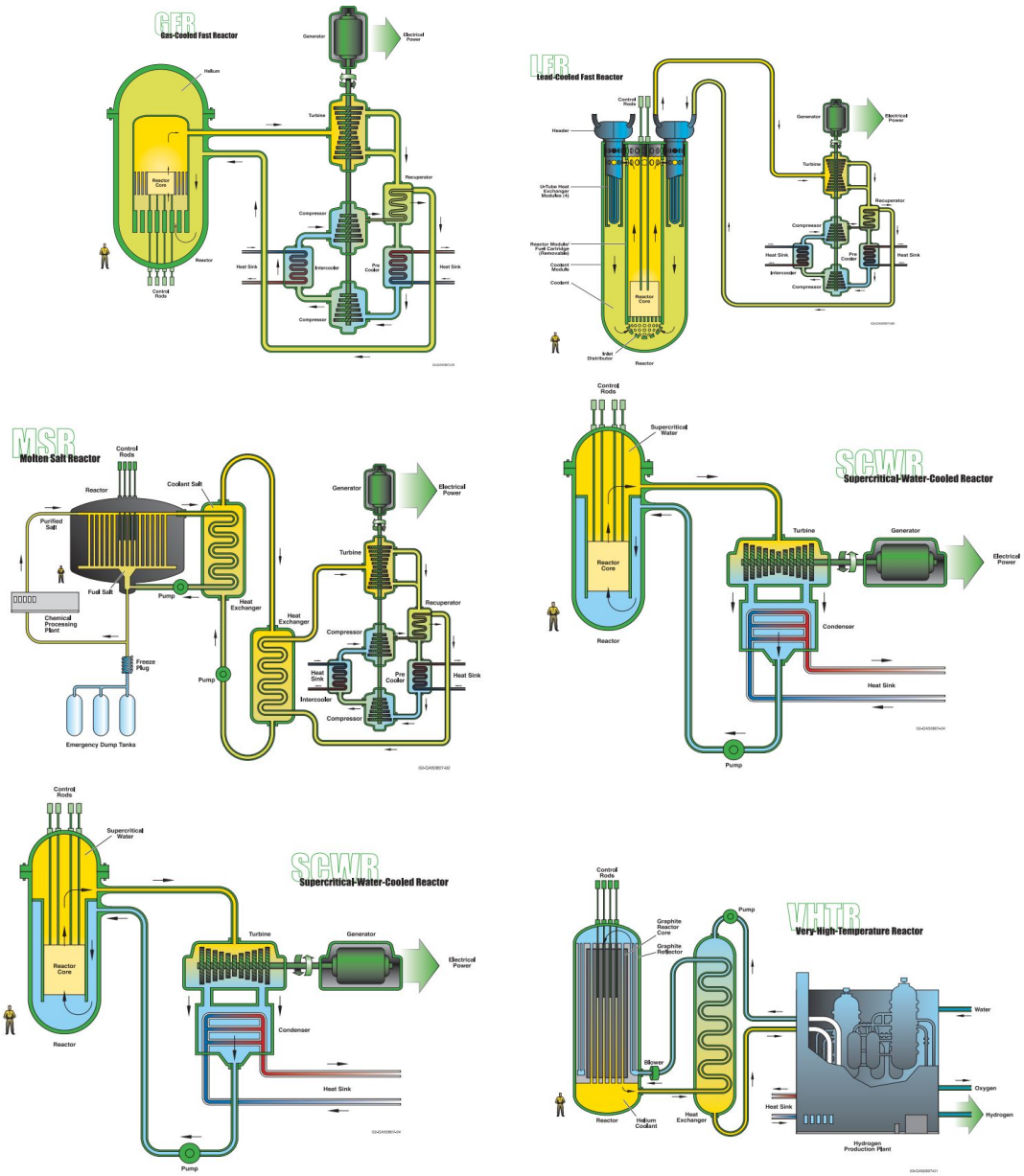

Figure 2.2: Generation IV reactors [15]

[16] [17]. The first nuclear reactor named EWA started operating in 1958 and between 1961-1972 four critical assembles (zero-power reactors): ANNA, MARYLA, AGATA and PANNA were constructed [16] in the Institute of Nuclear Research. Currently, the sole operating nuclear reactor in Poland is the MARIA reactor. MARIA is a research reactor that started to operate in 1974. The main applications of the MARIA reactor are the production of radioisotopes and material testing. In 1984 the construction of the first nuclear power plant in Poland (Zarnowiec Nuclear Power Plant) started but it was never been completed. There has never been an operating nuclear power plant in Poland. Currently, Poland has experienced a renaissance of nuclear energy. The objective of the Polish Nuclear Power Programme (PNP Programme) is to build 6-9 GWe of installed nuclear capacity based on proven, large-scale, Generation III+ PWR technology [18]. The construction of nuclear power will enable the replacement of the ageing high-emission load coal units with zero-emissions units, increasing diversification, energy independence and security, and suppressing the increase of energy costs. In November 2022, The Council of Ministers of Poland announced the plans to build a nuclear power plant up to 3750 MWe based on Westinghouse AP1000 reactor technology in Choczewo district or Gniewino and Krokowa districts [19]. Commissioning of the first reactor in the first nuclear power plant is planned for 2033. Two working nuclear power plants with three nuclear reactors inside each should be working in Poland by 2043 [18].

In Poland, it is also planned to meet the heat demand of the chemical industry by producing energy in HTRs [20]. Currently, there is no HTR design ready for multiplication on an industrial scale. Construction of the first HTGR (High-Temperature Gas Cooled Reactor) prototype in Poland is planned for next years. The Polish national project GOSPOSTRATEG-HTR was launched for the development of a pre-conceptual design of an HTGR. Parallel running nuclear plans are shown in Fig. 2.3.

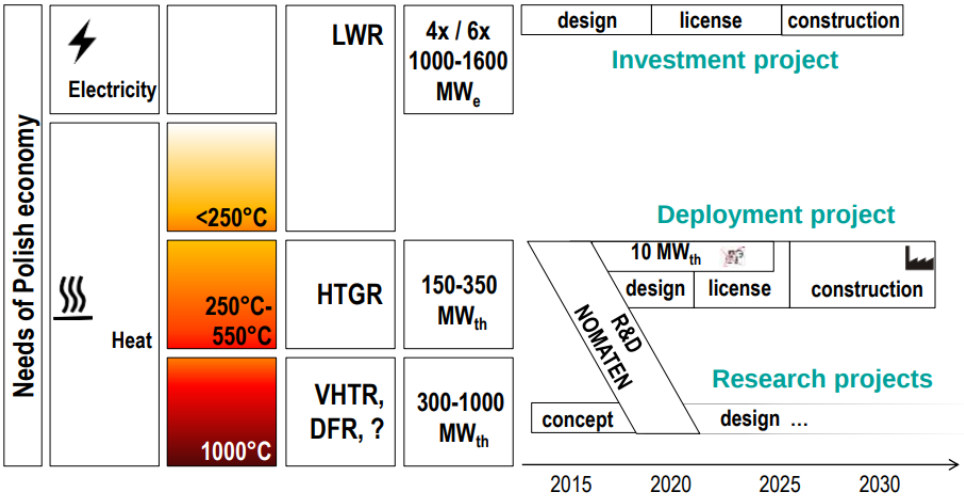

Figure 2.3: Nuclear roadmap for Poland [21]

One of the high-temperature reactor technologies, in which Polish researchers are involved in its development, is the Dual Fluid Reactor (DFR), described in the subsequent part of this chapter.

2.2 Materials for nuclear reactors

The effectiveness of a technological solution is linked to the properties of available materials. Therefore, improvements in nuclear reactor design depend on the development of new materials. The most common material used in currently working nuclear power plants is concrete and steel. In PWRs and BWRs, the fuel is UO_2 or other fissile actinides and is placed in ceramic fuel cladding. The fuel cladding is made of Zircaloy (Zirconium-based alloy) [22]. The interest in Accident Tolerant Fuel began after the Fukushima accident in 2011 [23] [24]. Elevating the operating temperature of the reactor necessitates the use of high-temperature resistant materials that also satisfy other physical, chemical and nuclear properties. A variety of nuclear reactor concepts require different types of materials. It is required that the material does not corrode in the presence of fuel and coolant. The choice of materials for HTR is a challenge due to the temperature that prevails in their core. The summary of materials that can be used in HTR reactors, as well as a material for BWR and PWR is presented in Table 2.2.

Table 2.2: Summary of materials for PWR, BWR and Generation IV reactors [15] [25]

Type	Cladding	Structural materials	
		in core	Out of core
PWR	Zirconium alloy	Stainless steel, nickel-based alloys	Stainless steel, nickel-based alloys
BWR	Zirconium alloy	Stainless steel, nickel-based alloys	Stainless steel, nickel-based alloys
GFR	Ceramic	Refractory metals and alloys, ceramics, ODS	Ni-based superalloys
		Vessel: F-M	Ni-25Cr-20Fe-12.5W-0.05C
			Ni-23Cr-18W-0.2C
			F-M with thermal barriers
LFR	High-Si F-M, ODS,	High-Si F-M, ODS,	High-Si austenics,
	Ceramics, refractory alloys		Ceramics or refractory alloys
MSR	-	Ceramics, refractory metals	High-Mo, Ni-base alloys
		High-Mo Ni-base alloys	
		Graphite, Hastelloy N	
SFR	F-M or ODS	F-M ducts, 316SS grid plat	Ferritics, austenitics
SCWR	F-M (12Cr, 9Cr, etc.),	Same as cladding, low-swelling stainless steel	F-M, low-alloys steel
	Fe-35Ni-25Cr-0.3Ti		
	Incoloy 800, ODS		
	Incoloy 690, 625, 718		
VHTR	SiC or ZrC coating	Graphites	Ni-based superalloys Ni-25Cr-20Fe-12.5W-0.05C
	surrounding graphite	PyC, SiC, ZrC	Ni-23Cr-18W-0.2C, F-M with thermal barriers
	(fuel: TRISO)	Vessel: F-M	low-alloy steels

F-M ferritic-martensitic stainless steels, ODS oxide-dispersion-streghened steels,

2.3 Dual Fluid Reactor

The Dual Fluid Reactor (DFR) is a novel concept of a fast nuclear reactor that employs two separate loops, one for liquid fuel and one for liquid coolant, both flowing through the core [1] [2] [26]. Thus, the DFR core plays the role of the heat exchanger. The DFR combines the advantages of MSR, LFR and VHTR. Two versions differing in fuel were proposed: DFR_m and DFR_s. For the DFR_m fuel is an eutectic mixture (uranium and chromium metals) and for DFR_s molten salts (uranium, thorium or plutonium chlorides) may be used [26] [27]. Pure liquid lead and lead-bismuth eutectic are possible coolants. The temperature in the core is in the order 1000 °C. DFR is characterized by high efficiency and total burnup [1] [2] [28]. DFR can be used for electricity production and also for industrial heat production. A very high temperature in the core enables hydrogen production. DFR can be used as a long-term burner of actinides in spent nuclear fuel (SNF) [3] [29]. The advantage of DFR technology is easy scalability for requirement size. Several designs of DFR with different thermal power output was proposed, for example, 3000 MW_{th}, 250 MW_{th} and 2 MW_{th} [4] [30] [31]. The scheme of the large DFR power plant (3000 MW_{th}) is presented in Fig. 2.4. For the DFR special integrated Pyroprocessing Unit (PPU) unit is proposed to perform fuel processing on-site for separation of transmutation elements and fission products. The principle of PPU operation is pyrochemical distillation that uses differences in the boiling points of different chemical compounds [32]. The flows of liquid can be controlled by MHD pumps [33] [34]. DFR is stable and self-regulating [35]. Passive safety of the DFR will be provided by the negative temperature reactivity coefficient [36]. Additional protection will be the drain tank connected with the loop by melting the fuse. If the temperature increases too much, then the fuse melts and the fuel goes to drain tank and the reaction stops.

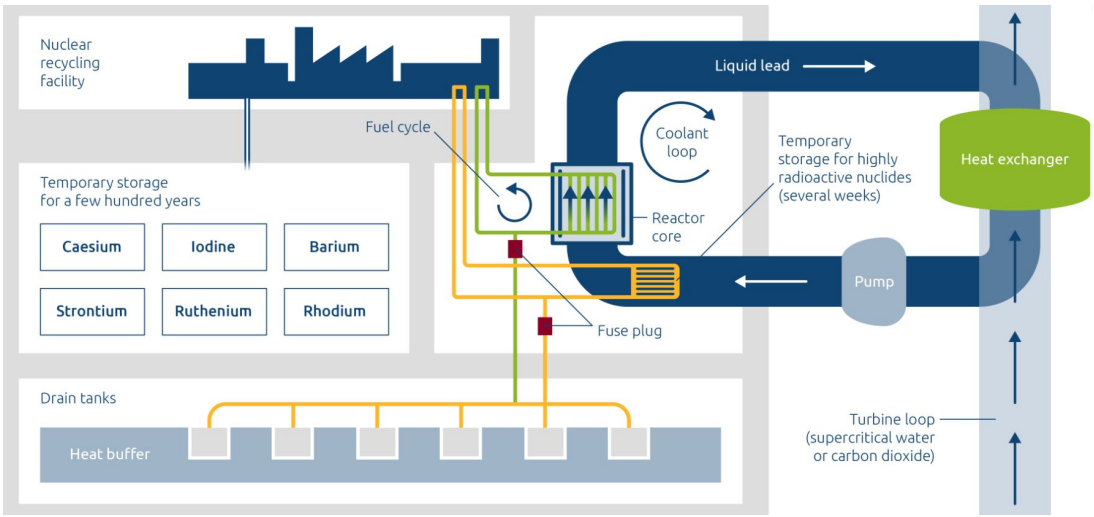

Figure 2.4: DFR power plant with on-site recycling [37].

DFR was initially developed and patented by a researcher from the Institute of Solid-State Nuclear Physics in Berlin, Germany [1]. In February 2021, the existing team with investors started Dual Fluid Energy Inc. company. Preliminary studies have demonstrated the feasibility of this technology. The next step is component testing. The planned timeline for DFR development is presented in Fig. 2.5. A prototype of the reactor is expected within a decade. The DFR micro demonstrator is currently being designed in NCBJ. In the coming years, the construction of a the first DFR test reactor in Rwanda is planned in next years. In September 2023, an agreement was signed with the Rwandan government.

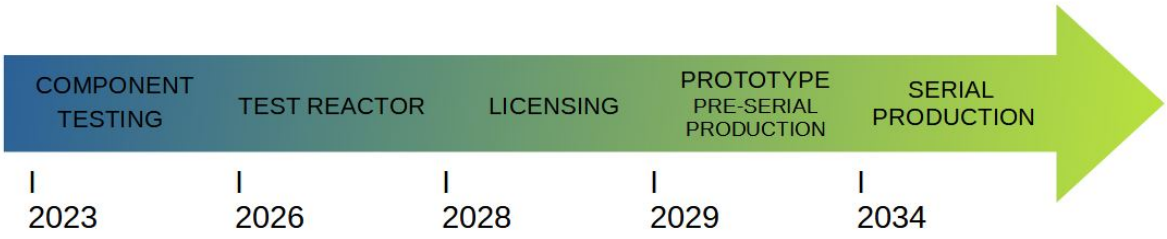

Figure 2.5: DFR timeline.

DFR has not only fulfilled requirements established for Generation IV nuclear reactors but has also gone beyond Generation IV categorization, thereby being recognized as a prospective Generation V reactor.

2.4 DFR materials

The extreme environment inside a DFR means that special materials are required for its construction. The materials should have high thermal conductivity and be corrosion-resistant to coolant (lead) and liquid fuel (molten salt or eutectic mixture). They should retain their properties in high temperature and radiation environments. The spectrum of neutrons in DFR core is presented in Fig. 2.6. The neutron spectrum in the DFR is dominated by fast neutrons. Therefore the materials for DFR should have a low neutron capture cross section for fast neutrons.

Due to the special design of the DFR core, a small quantity of construction materials is needed compared to other nuclear technologies. For this reason, even expensive materials can be used and will have little impact on the total cost of the system.

In the case of fuel and coolant, DFR is a combination of LFR and MSR so materials in the case of corrosion should meet similar requirements, but due to temperature, it will be the most similar to VHTR. Examples of good candidates for structural materials for

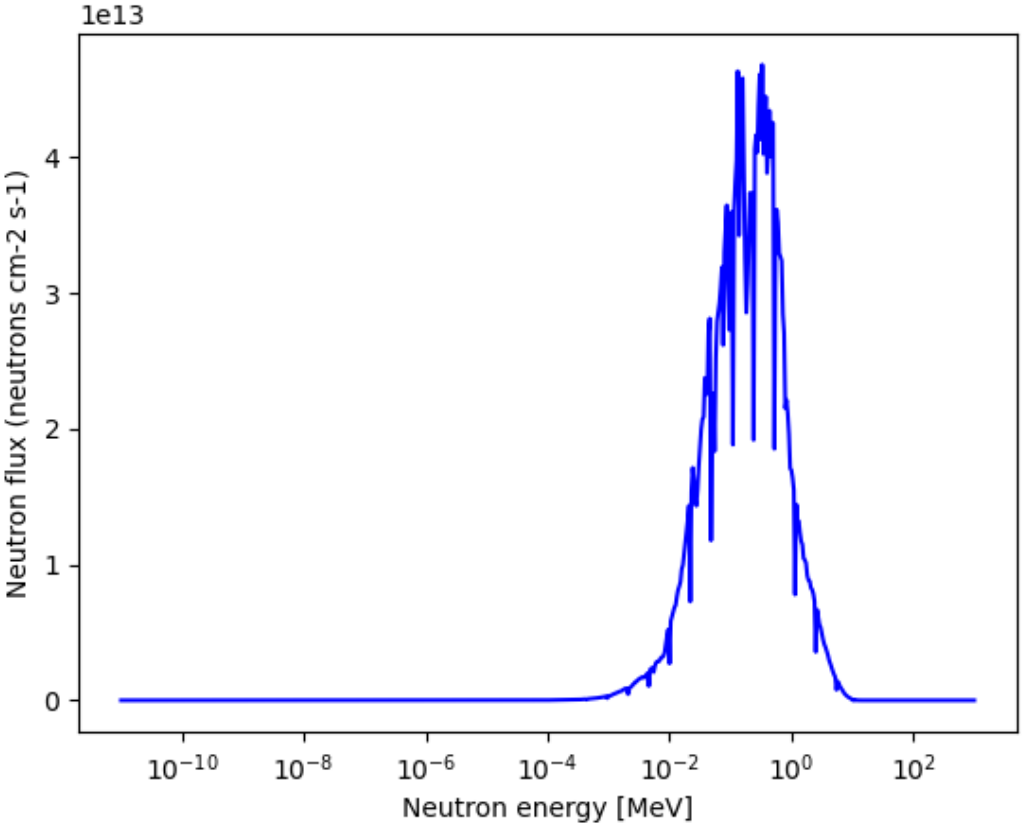

Figure 2.6: DFR mean neutron spectrum [30]

DFR are hard ceramic materials such as Silicon Carbide, Zirconium Carbide and Titanium Carbide or alloys of refractory metals, molybdenum- and tungsten-based alloys [4].

2.5 Silicon Carbide

Silicon Carbide (SiC) is a covalently-bonded material, which consists of 50% silicon and 50% carbon atoms. The possibility of a chemical bond between Si and C was proposed by Berzelius in 1824. Finally, Acheson produced SiC by mixing coke and silica in a furnace in 1893[38]. Production technology has advanced since then and currently, SiC is available in many desired forms. The Silicon Carbide phase diagram is presented in Figure 2.7. SiC is a high-temperature material that is also characterized by high strength and chemical stability [39].

SiC is a promising material for several applications such as nuclear, electronic and space applications [41], [42], [43], [44],[45]. The narrative of SiC in the context of nuclear energy commences around 1960, coinciding with the inception of coated fuel development [41].

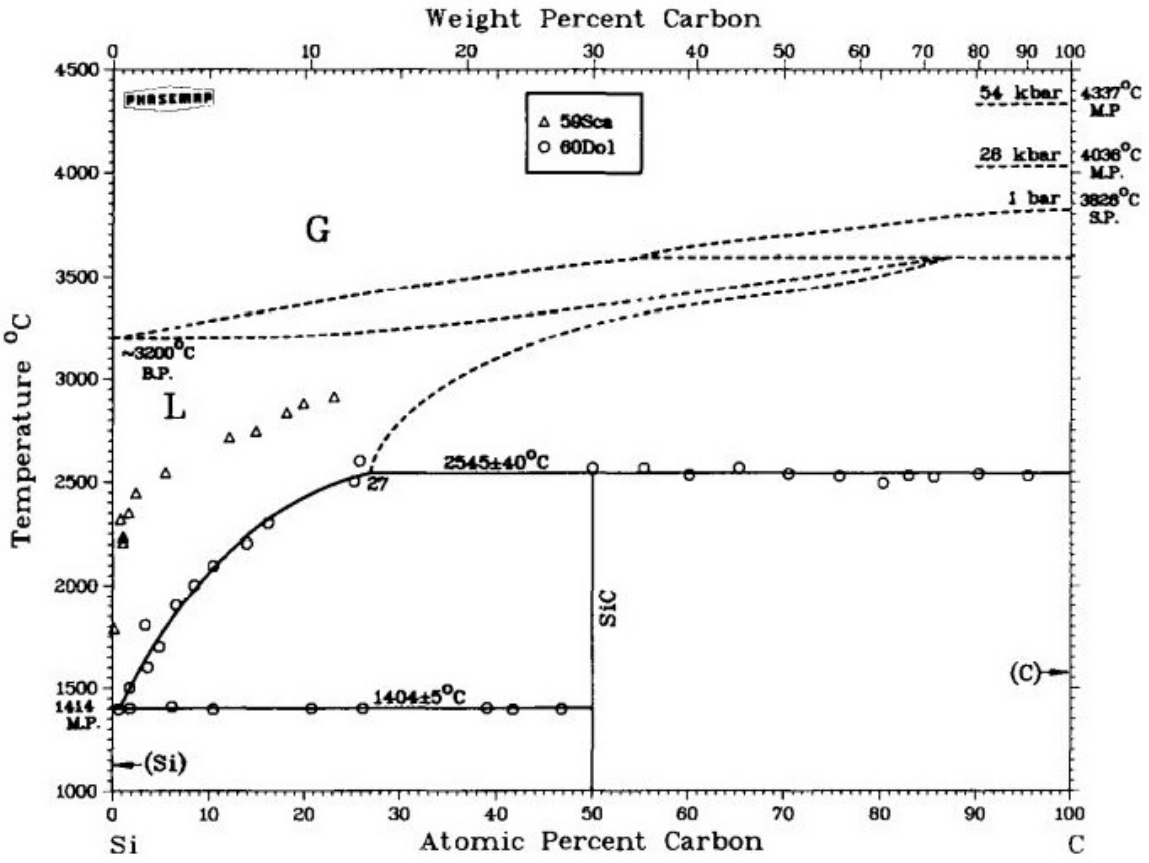

Figure 2.7: SiC phase diagram [40]

SiC can exist in many solid-state forms: as an amorphous form, polycrystal or single crystal. The most common monocrystalline structures of SiC are zinc-blende (3C-SiC) and wurtzite (6H-SiC or 4H-SiC). These polytypes are characterized by the stacking sequence of Si-C bilayers and are visualised in Fig. 2.8.

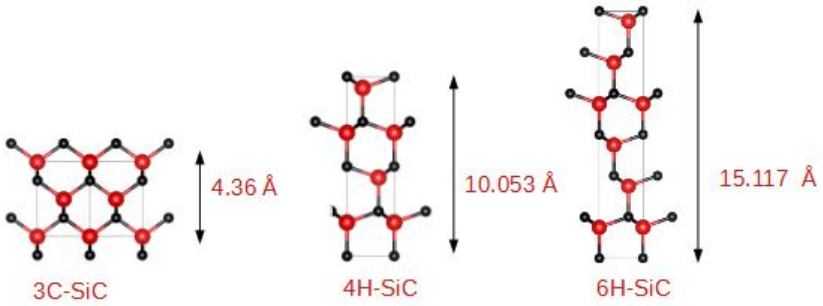

Figure 2.8: SiC polytypes. The crystal structures was visualised by VESTA [46]

Figure 2.9 shows an illustration of the three different positions of SiC layers in the lattice: A, B and C. ABCABC stacking sequence is characterized for cubic 3C-SiC, ABCB stacking sequence is characterized for hexagonal 4H-SiC, ABCACB stacking sequence is characterized for hexagonal 6H-SiC.

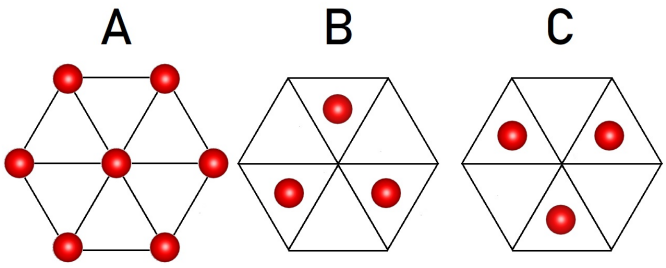

Figure 2.9: SiC stacking

Polytypes of SiC have different electronic properties. The band gap varies from 2.3 eV to 3.3 eV. The most common crystal structure used in nuclear applications is 3C [5].

Chapter 3

Radiation damage

3.1 Primary radiation damage

High-energy particles such as neutrons or ions interact with the material, by transferring energy to atoms. A lattice defect can arise when the atom receives enough energy to jump from its initial position. If transferred energy is sufficient, primary knock-off atoms (PKA) can displace another atom from the lattice called secondary knock-on atoms. Thus a large number of atomic displacements can be produced and this process can be described as displacement cascades (fig. 3.1). Incident particles can also affect the heating of the material and produce phonons, photons, excitons, plasmons, and secondary electrons. Produced defects can create complicated structures inside material like defects clusters, amorphous zones, or dislocation loops, and on the surface: adatoms, craters, or ripples [47]. The primary radiation damage can be described as damage produced right after atomic displacement caused by incident high energy particles and takes place approximately in the first picoseconds. Next, long-time damage evolution happens in timescale from nanoseconds to years. The modification of material macroscopic properties is referred to as radiation defects.

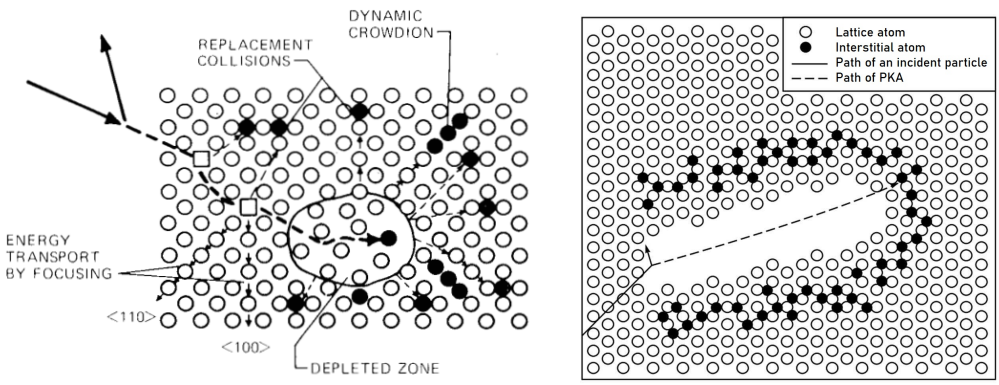

Figure 3.1: Radiation damage [48] [49].

The most fundamental quantity for determining radiation damage in materials is the threshold displacement energy (TDE, E_d), defined as the minimum energy required by an atom in the solid to create stable defect [47] [50], so atomic displacements occur when energy given to atom T_d is greater than E_d.

Radiation damage can be measured using the unit of displacement per atom (dpa). The dpa is the ratio of the number of displacements per unit volume and unit time (R) on the material atomic density (N) and is represented by the equation 3.1, where $\sigma_D(E_i)$ - the energy-dependent displacement cross-section, $\Phi(E_i)$ - the energy-dependent particle flux per unit energy, E_M - the maximum energy of incoming particle, E_m - the minimum energy of incoming particle.

$$R_{dpa} = \frac{R}{N} = \int_{E_M}^{E_m} \sigma_D(E_i)\Phi(E_i)dE_i \tag{3.1}$$

Standardization of the displacement dose calculation method is needed for the comparison of different irradiation experiments and makes it easier to predict the behaviour of irradiated material after irradiation with different particles.

The current international standard definition of dpa is based on Norgett-Robinson-Torrens (NRT) model and because of that sometimes called NRT-dpa [47] [51]. Based on the NRT-dpa model, the number of atomic displacements can be determined by equation 3.2. Although this model is very common for determining dpa, it has certain limitations.

$$N_{NRT} = \begin{cases} 0 & 0 < T_d < E_d \\ 1 & E_d < T_d < \frac{2E_d}{0.8} \\ \frac{0.8T_d}{2E_d} & \frac{2E_d}{0.8} < T_d < \infty \end{cases} \tag{3.2}$$

3.2 Neutron interaction with matter

Neutron radiation damage is crucial for the nuclear reactor, as the main reaction inside it is fission, which produces free neutrons. A unique characteristic of neutrons is that they have no electric charge so the Coulomb barrier does not apply to them. This allows neutrons to collide with nuclei. Defects can be formed by neutrons scattering off the nucleus or neutrons combining with the nucleus. After neutron absorption, some type of particle might be emitted from the nucleus such as alpha particle or gamma particle. Examples of reactions caused by neutrons are: (n, n), (n, n'), (n, 2n), (n, γ), (n, p), (n, np). Neutrons are divided depending on their energy into the following types: thermal, slow, intermediate, and fast. The probability of each reaction (i.e., its cross-section) depends on neutron energy and the type of target nuclei. .

3.3 Ion interaction with matter

An energetic heavy ion loses energy by elastic energy transfer to atomic nuclei (recoil) and inelastic energy transfer to electrons (excitation and ionization). Stopping power is the rate of energy loss per unit length ($S = dE/dx$) and can be separated based on the energy transfer to the target nuclei (nuclear-stopping power S_n) and the energy loss to electrons (electron stopping power S_e) as it is shown in Eq. 3.3. Energy losses are a discrete phenomenon because nuclear collision has an individual character. However, given the many interactions of the incident particle with the target atoms or electrons, statistically, it can be assumed that the ion loses energy in a continuous process and the stopping power can be described in $\mathrm{eV\,nm^{-1}}$.

$$\frac{dE}{dx} = \left(\frac{dE}{dx}\right)_{nuclear} + \left(\frac{dE}{dx}\right)_{electronic} \tag{3.3}$$

The projectile range can be determined from Eq. 3.4. Collisions are statistically independent and the result of it is straggling. Straggling is a small spread in the ion range.

$$R = \int_{E_0}^{0} \frac{1}{\frac{dE}{dx}} dE \tag{3.4}$$

When the incident ions collide with the atoms in the target, the ions can lose energy and change direction. This phenomenon is referred to as an ion-atom collision, although in fact, it is usually not a direct collision, but an indirect one. As a result of the Coulomb interaction, the ions change their trajectory under the influence of the repulsive force exerted on them by the nucleus of the target atom. The scheme of ion-atom interaction is presented in Fig. 3.2.

The maximum energy that can be given from the ion can be described by Eq. 3.5.

$$T = \left[\frac{4M_1M_2}{(M_1+M_2)^2}\right] E_0 \tag{3.5}$$

The energy loss due to ionization can be described as the Bethe-Bloch formula (3.6), where z - atomic number of incident particle, A - atomic mass of absorber, Z - atomic number of absorber, N_A is Avogadro number, r_e - electron radius, m_e - electron mass, I - characteristic ionization constant material dependent, γ - density effect correction, β is the relative velocity (v/c) [53].

$$\left(-\frac{dE}{dx}\right) = 2\pi r_e^2 m_e N_A c^2 z^2 \frac{Z}{A}\frac{1}{\beta^2}\left[ln\left(\frac{2m_e\gamma^2c^2\beta^2}{I^2}\right) - 2\beta^2 - \frac{\gamma}{2}\right] \tag{3.6}$$

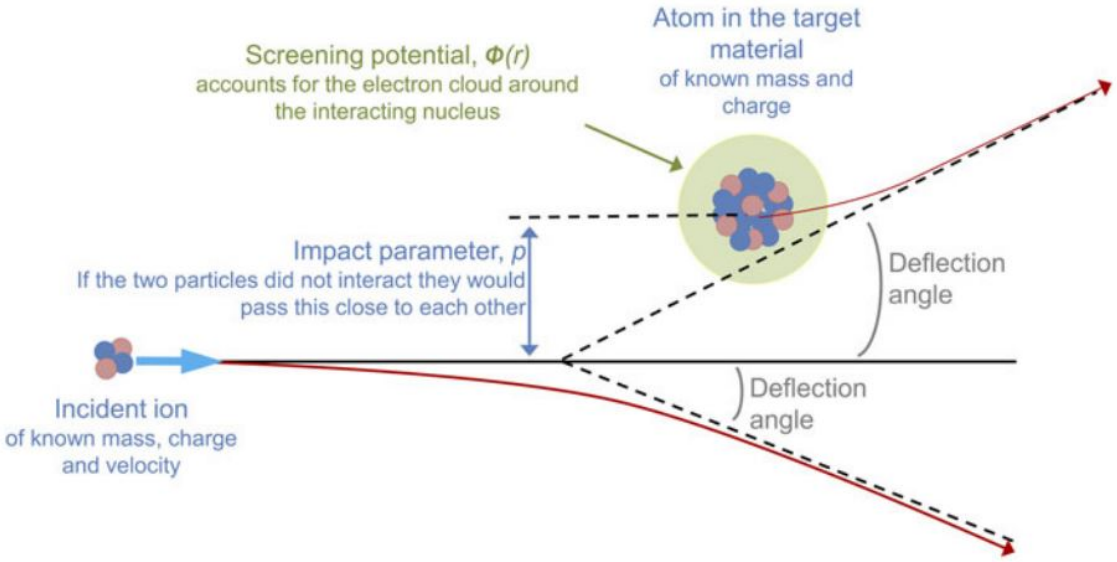

Figure 3.2: Scheme of nuclear collision [52].

As they pass through matter, the ions interact with the electrons of the target objects and can push thousands of electrons out of atoms. If the energy imparted to the electrons is large enough, the electrons can cause secondary ionization. The electrons from the second ionization are called δ rays. The following formula describes the radial distribution of dose from δ rays around the path of heavy ion (Eq. 3.7)[54]. $D(r)$ is the dose deposited in a coaxial cylindrical shell of thickness dr at a distance r from the ion path.

$$D(r) = \frac{N_e e^4 Z^{*2}}{\alpha m_e c^2 \beta^2 r} \left[\frac{\left(1 - \frac{r+\theta}{R+\theta}\right)^{1/\alpha}}{r+\theta} \right] \tag{3.7}$$

The effective charge of an ion of Z elementary charge can be described by the formula:

$$Z^* = Z[1 - exp(-125\beta Z^{-2/3})] \tag{3.8}$$

The ionization effects of ion irradiation on material strictly depend on energy dissipation, the timescale of this energy dissipation and the target material properties (thermal conductivity, phase change temperature). The incident ion deposits energy in a region with a small radius, about 50% of its energy is deposited in the zone within 1 nm [55]. If defects are created in the region along the ion path, this zone can be called an ion track. The impact of electronic energy deposition on lattice dynamics can be elucidated through three distinct mechanisms: Coulomb explosion, lattice relaxation, and the thermal spike [55], [56]. The Coulomb explosion model assumes that high-energy ions can remove electrons from the nuclei of the target. Then, the electrons can escape from the centre of

the ion path. If the charge neutralization time is long, then, repulsion between atoms can occur. This movement of atoms can create defects. The energy that is deposited can affect electronic potential energy and then change interatomic forces. This effect of non-equilibrium is assumed by the lattice relaxation model. Thermal Spike assumes that transferred energy can create hot plasma from electrons and this electron can transfer energy to atoms in the lattice. The heating of atoms in a lattice can influence atom dynamics.

Although there are presumptions of isolation between the stopping power effects of nuclear and electron contributions, the generation of defects could result from the interactions between these stopping power components [57] [58] [59]. Electronic stopping power can anneal defects produced by nuclear-stopping power while electronic stopping power can increase the effects of sputtering, the creation of the defect can cooperate and then the total defects number is less than from electronic stopping power and nuclear-stopping power separately or can be equal to the sum of defects produced by electronic stopping power and nuclear-stopping power.

3.4 Thermal Spike

One of the explanations for the occurrence of ion track is the thermal spike model (TS model) [8]. TS model is a link between the energy deposited in electrons and the resulting effects in the atoms in the target lattice. In a crystal lattice, atoms oscillate around their equilibrium position due to their thermal energy. This atomic vibration energy and heat are transferred through the solid by a quasi-particle named phonon. Electrons can influence phonons by exchanging energy and momentum with them. In this way, the energy that is given to the electrons by the incident ion can be transferred to the electron by electron-phonon coupling to the atoms in the lattice. As the result of energy transfer, lattice temperature can increase and have an effect on local melting in materials, vaporization or phase change. A schematic illustration of the thermal spike model is presented in Fig. 3.4.

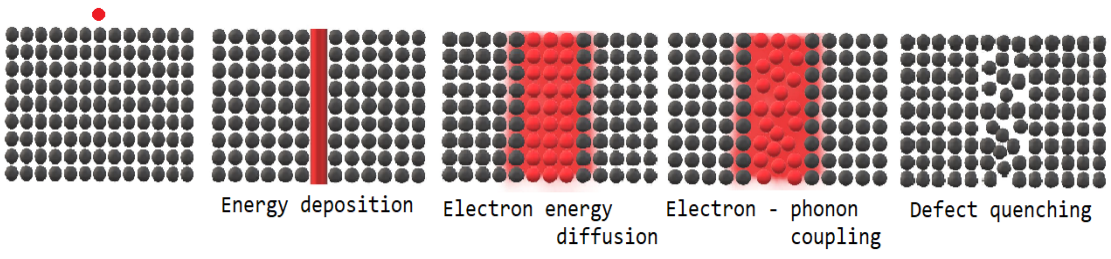

Figure 3.3: Schematic illustration of thermal spike model.

TS model assumes that the target material is a two-component system consisting of the atomic lattice and the electrons, and the ion track is continuous. The underlying postulate of this model is that the nanoscale can be considered as a micro-scale. Thus, the diffusion equation can be used in small timescales and small space-time. These subsystems can be coupled by equations 4.2 and 4.3, where T_a, T_e - lattice and electron temperature, C_a, C_e - lattice and electron specific heat, K_a, K_e - lattice and electrons heat conductivity, g - electron-phonon coupling. A(r, t) is the energy deposited in the electronic subsystem for a specific energy and can be calculated using the formula 3.7 for radial dose distribution and Gaussian distribution for time dependence [54][8].

$$C_a(T_a)\frac{\partial T_a}{\partial t} = \frac{1}{r}\frac{\partial}{\partial r}\left[rK_a(T_a)\frac{\partial T_a}{\partial r}\right] + g(T_e - T_a) \tag{3.9}$$

$$C_e(T_e)\frac{\partial T_e}{\partial t} = \frac{1}{r}\frac{\partial}{\partial r}\left[rK_e(T_e)\frac{\partial T_e}{\partial r}\right] - g(T_e - T_a) + A(r,t) \tag{3.10}$$

Temperature increase in the ion path may affect the material structure, for example, if the energy is high enough melting of a small cylinder near the ion path can occur. This can impact crystal structure and form the amorphous track [60] [61]. The increase in temperature can also repair the disorders in the lattice [62].

3.5 Ion irradiation effects in SiC

Radiation effects in SiC have been studied since the middle of last century [41]. Despite that, there are still many unknowns. Radiation defects production in SiC depends on particle type and mass, temperature, dose and dose rate, and energy deposited in atomic and electronic structure. Currently, well-known are the effects of ion irradiation in low-energy regimes where nuclear stopping dominates and in very high-energy regimes where electronic stopping power dominates. In low-energy damage, ballistic collision produces defects and can lead to the amorphization of SiC. At room temperature, SiC is amorphized at a dose of 0.2 - 0.4 dpa [63] [64] [65] [66]. Irradiation in higher temperatures (about 500 °C) does not produce amorphization [63] [67]. SiC is insensitive to defects production in high energy regimes. No evidence of track was observed until 34 keV/nm [68] [69]. Electronic energy deposition can recover SiC lattice [70] [71] [72] [73] [74], [75], [76], [77], [78]. The previous investigations show that the athermal recovery in SiC with electronic stopping power can occur at 10 - 34 $\mathrm{keV\,nm^{-1}}$ [64].

The lack of knowledge happens in the intermediate energy regimes (from a few hundreds keV to a few tens MeV) where defect productions and ionization occur. It was

suggested that even 4.5 MeV C and 21 MeV Si ions can induce ionization annealing defects [6], [7], [79]. The threshold electronic energy deposition for annealing of pre-existing defects is 1.86 keV/nm for 4.5 MeV C and 5.03 keV/nm for 21 MeV Si, while Xue proposed that ionization 1 keV/nm is enough to in-cascade ionization annealing [10]. As Nucklos et al. suggested the recovery threshold can be determined by extrapolation of the linear dependence of Si disorder on electronic energy loss to zero disorder [79]. The summary of a study of electronic energy threshold for recovery is presented in table 3.1.

Table 3.1: Electron Stopping Threshold [7] [79]

Ion	Atomic number	Ion energy [MeV]	Electronic energy loss [keV/nm]	S_e/S_n at threshold	E_{th} [MeV]	Dose at threshold [dpa]
C	6	4.5	1.86	404	3.25	0.005
O	8	6.5	2.61	334	5.5	0.006
Si	14	18	5.02	403	17.9	0.010
Si	14	21	5.03	439	19.2	0.010
Ti	22	20	7.14	197	22.2	0.028
Ti	22	23	7.38	227	25.5	0.026
Ni	28	21	8.34	127	22.3	0.048
Ni	28	21	7.12	122	15.8	0.076

3.6 Ion as a surrogate for neutron irradiation

In recent years, there has been a growing interest in using ions as surrogates for neutron radiation. This increased interest is due to several advantages associated with using ions instead of neutrons, most notably the simultaneous reduction of experiment time and cost [80] [81] [82]. This idea is not novel, it was proposed in the 1970s [83] [51] [84]. Presently, the majority of available standards and guidelines pertaining to metals and alloys [85] [86]. To simulate neutron-induced damage with ions, a comprehensive understanding of the similarities and differences in the formation of defects generated by these particles is imperative. The fundamental difference between neutron and ion irradiation can be pointed out as follows [83] [87]:

1. Neutrons can be absorbed by atomic nuclei, leading to the initiation of nuclear reactions.

2. Due to the process of absorption, the transmutation of atomic nuclei can ensue and produce impurities, and the release of helium and hydrogen can cause voids.

3. Ions exhibit significantly larger elastic scattering cross-sections than neutrons.

4. The mean free path between collisions is centimetres for neutrons and nanometers for ions.

5. The density of defects is depth-dependent following ion irradiation.

6. The energy deposit depends on the energy of the ions. High-energy ions result in the excitation and ionization of electrons, while lower-energy ions predominantly involve in elastic scattering interactions. However, it is worth noting that low-energy ions, while primarily associated with elastic scattering, exhibit limited range.

To achieve optimal defect production simulation, it is imperative that the ion energies closely approximate the energy levels of primary recoils induced by neutron irradiation. The PKA energy for SiC in DFR is presented in Fig. 3.4.

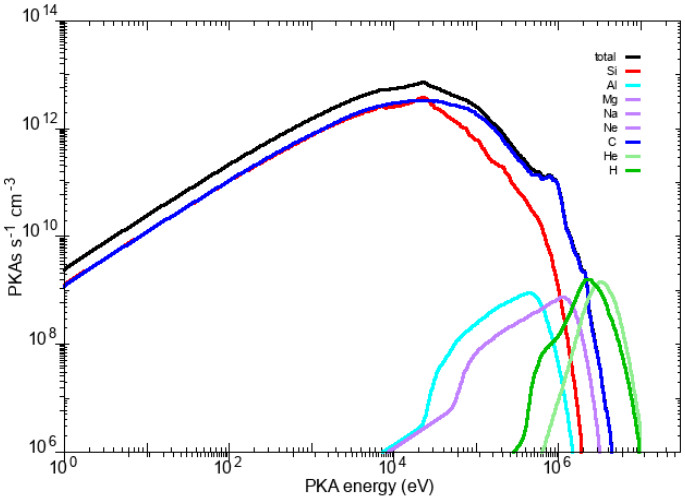

Figure 3.4: Primary recoil spectrum in SiC determined for DFR neutron fluence predicted by SPECTRA-PKA code [88].

For reproduction of release He, He implantation should be used. He should be implanted simultaneously with ions capable of causing primary radiation damage. Therefore, multi-beam irradiation was proposed for the best reconstruction of defects production [89] [90] [91] [92] [93] [94] [81] [95] [87].

Chapter 4

Computational methods

4.1 The Stopping and Range of Ions in Matter

4.1.1 SRIM introduction

The Stopping and Range of Ions in Matter (SRIM) code is a widely used computational tool for calculating ion distribution, nuclear and electron stopping power, and damage production [50]. SRIM employs the Monte Carlo method, specifically the Binary Collision Approximation (BCA), as its computational approach. Nuclear stopping power is calculated based on the collisional scattering of two atoms with electrons screening, while electronic stopping power for the heavy ion is based on Brandt-Kitagawa approximation and Bethe-Bloch theory [96][50]. In SRIM nuclear and electronic stopping powers are calculated as independent and the correlation between nuclear collisions and energy losses to electron excitation is neglected. The designated target material has an amorphous structure, characterized by atoms residing in random positions, the thermal effects are not considered and the target has 0K. For SiC calculation "Detailed Calculation with Full Damage Cascades" (F-C) is recommended for simulations [97] [98].

In this work, SRIM 2008 was used. All calculations were performed in F-C mode with 50000 ions, target density set to $3.21\,\mathrm{g\,cm^{-3}}$, angle of incidence set to 7° (analogous to the conditions of subsequent ion implantation) and displacement energies of 20 eV for C and 35 eV for Si [99]. The lattice parameters used in the calculations are shown in the table 4.1. The results are in the following subsections.

4.1.2 The Stopping Power and Range calculation

Fig. 4.1 presents the nuclear and electronic stopping power as a function of ion energy for both Si and C ions in SiC. Notably, the nuclear-stopping power exhibits significance primarily at lower ion energies, while at higher ion energies, the electronic stopping power

Table 4.1: SiC lattice parameters [99] [100]

	Si	C
Threshold displacement energy	35 eV	20 eV
Lattice binding energy	3.25 eV	2.63 eV
Surface binding energy	4.7 eV	7.4 eV

dominates. The maximum attainable electronic stopping power for Si ions in SiC is $5\,\mathrm{keV\,nm^{-1}}$, whereas for C ions in SiC, it amounts to approximately $1.75\,\mathrm{keV\,nm.^{-1}}$

Fig. 4.2a presents the ratio of electronic stopping power (Se) to nuclear stopping power (Sn). Notably, for C ions, this ratio (Se/Sn) exceeds over that for Si ions by more than twice. It appears judicious to select ion energies of 21 MeV, 5 MeV, and 0.5 MeV for Si ions, and 5 MeV, 1 MeV, and 0.5 MeV for C ions for experimental study. This energy choice corresponds to the peaks in the maximum electronic stopping ratio for both Si and C ions, thereby encompassing a spectrum of distinct electronic-to-nuclear stopping power ratios. The range of Si and C ions in SiC in the function of ion energy is presented in Fig.4.2b. Si ions, being larger, have a shorter range. It is noteworthy that the selected ion energies result in ion ranges within the material of less than 10 μm.

4.1.3 Energy deposition

The energy deposition profile can be calculated from the E2RECOILS.txt and IONIZ.txt files that are produced by the SRIM code. Electronic and nuclear loss predicted for all energies of Si and C ions that have been considered in this research are shown in Fig. 4.3. For the experimental work described in Chapter 5, the most important is the energy deposition in depth from 0 nm to 1000 nm as this is the range of RBS/C analysis spectra. Attention should be drawn to the maximum range and the damage peak. For irradiation using 0.5 MeV ions, the damage peak should be noticed on experimental spectra.

4.1.4 Damage profile

The damage profile is the depth distribution of target atom displacements and can be obtained using two SRIM output files: VACANCY.txt and NOVAC.txt [101]. File VACANCY.txt includes the depth-dependent numbers of C and Si vacancies produced by the incident ion and recoiled atoms as well as target atoms recoiled by the incident ion. The numbers of replacement collisions are saved in the file NOVAC.txt. Displacement per atom (dpa) is a measure of the number of atoms that were set in motion during the collision cascade. Thus, the dpa is the sum of vacancy and replacement collisions [50]. The results of the calculations of displacements per ion and nm are presented in Fig. 4.4.

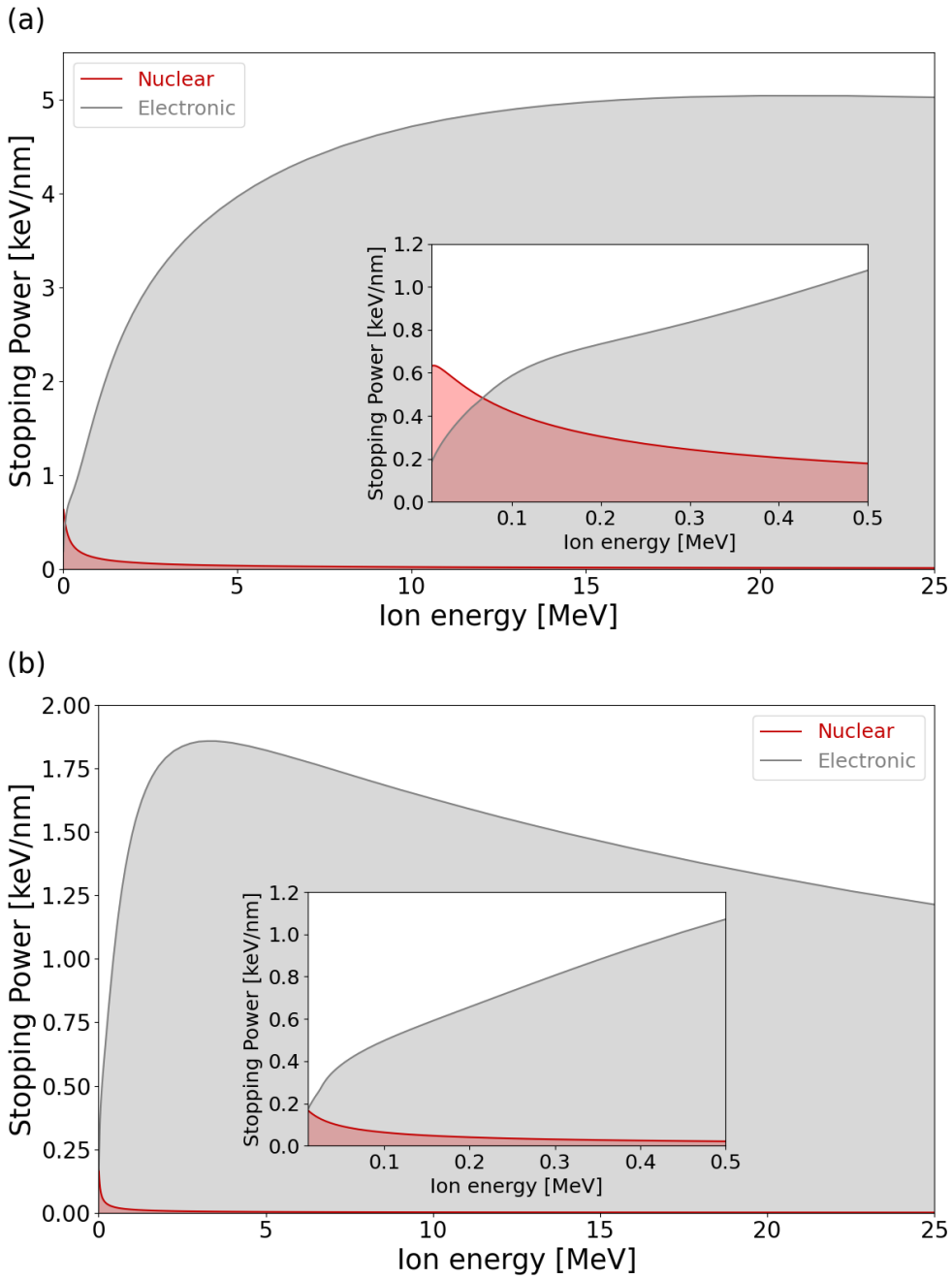

Figure 4.1: SRIM calculation showing the nuclear and electronic energy loss as a function of ion energy (a - Si ion in SiC, b - C ion in SiC). The region where nuclear-stopping power is significant is zoomed in and shown in the inset.

Later on, the values of displacements per ion - nm can be used for the dpa calculation using equation 4.1. In this work, SRIM was used to predict the fluence necessary for a dose equal to 0.01 dpa within depth 300 - 500 nm. The low dose was chosen to be in the range where standard computational models work. The results of these calculations are shown in table 4.2. Dose distribution in SiC upon Si and C ion irradiation up to fluences shown in table 4.2 is presented in Fig. 4.5.

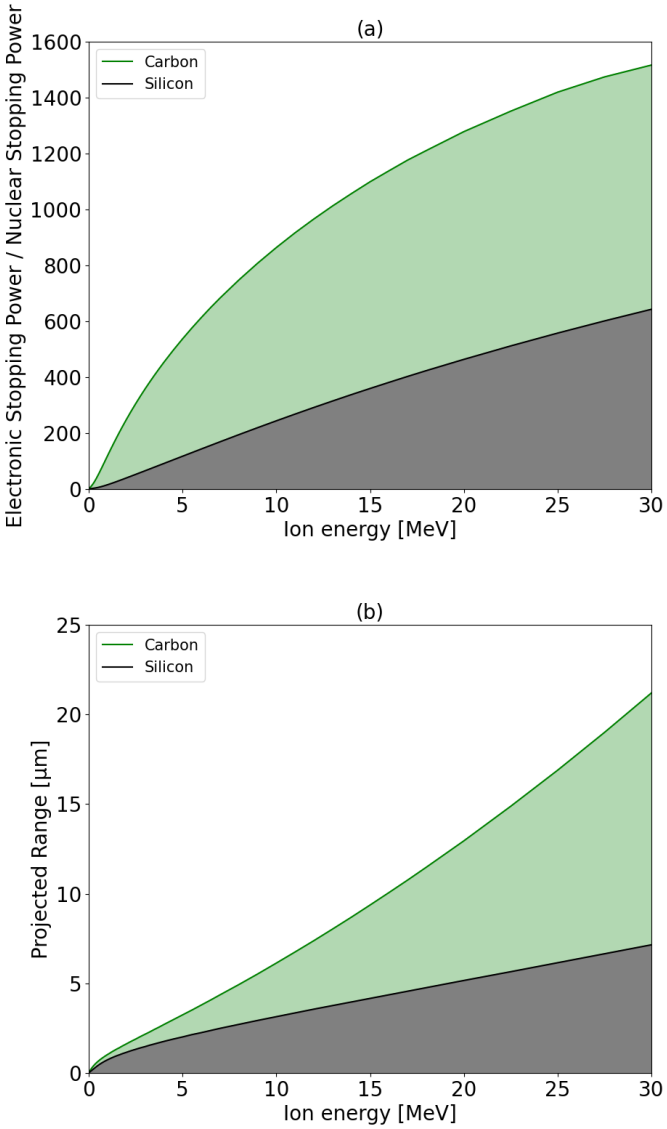

Figure 4.2: Electronic to nuclear stopping power ratio and ion range (b) for Si and C ions in SiC

$$dpa = \left[\frac{i - vpairs}{nm \cdot ion}\right] \frac{1}{10^{-7}} \frac{\phi[ions/cm^2]}{\rho_a[atoms/cm^3]} \tag{4.1}$$

Additional irradiations were performed to achieve a dose of 0.05 dpa at depth of 500 nm for Si ions with energies of 21 MeV, 5 MeV, and 0.5 MeV. In the case of 0.5 MeV Si, it makes it possible to achieve 0.1 dpa at depth 400 nm, which was important for damage production before irradiation with 21 MeV Si. Calculation results of necessary fluences are presented in Tab. 4.6.

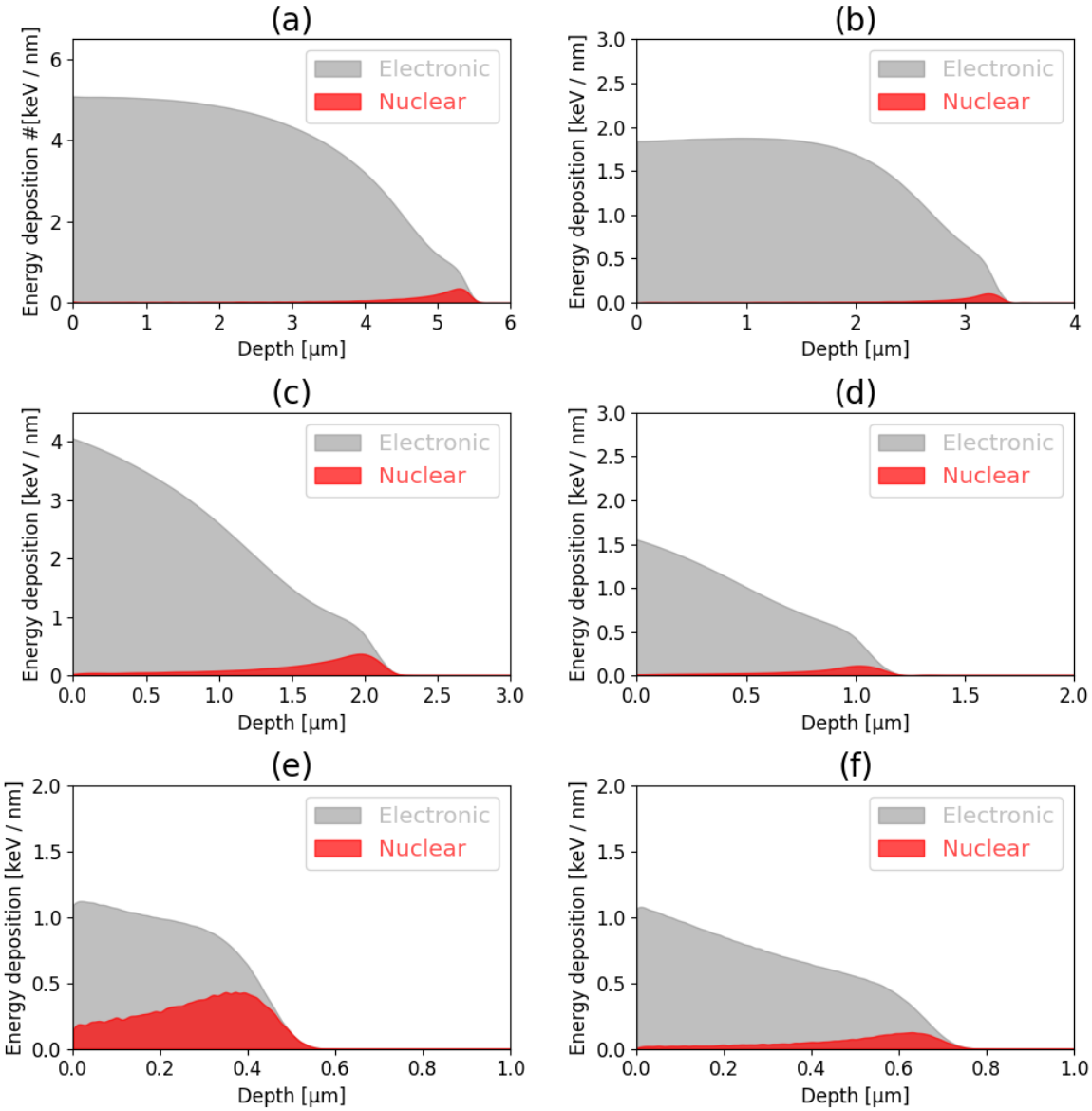

Figure 4.3: SRIM-predicted electronic and nuclear energy loss for 21 MeV Si ions (a), 5 MeV C ions (b), 5 MeV Si ions (c), 1 MeV C ions (d), 0.5 MeV Si ions (e), 0.5 MeV C ions (f)

Table 4.2: Fluence

Si		C	
Energy [MeV]	Fluence [cm^{-2}]	Energy [MeV]	Fluence [cm^{-2}]
21.0	$1.00 \cdot 10^{15}$	5.0	$2.00 \cdot 10^{15}$
5.0	$2.5 \cdot 10^{14}$	1.0	$4.0 \cdot 10^{14}$
0.5	$2 \cdot 10^{13}$	0.5	$1.5 \cdot 10^{14}$

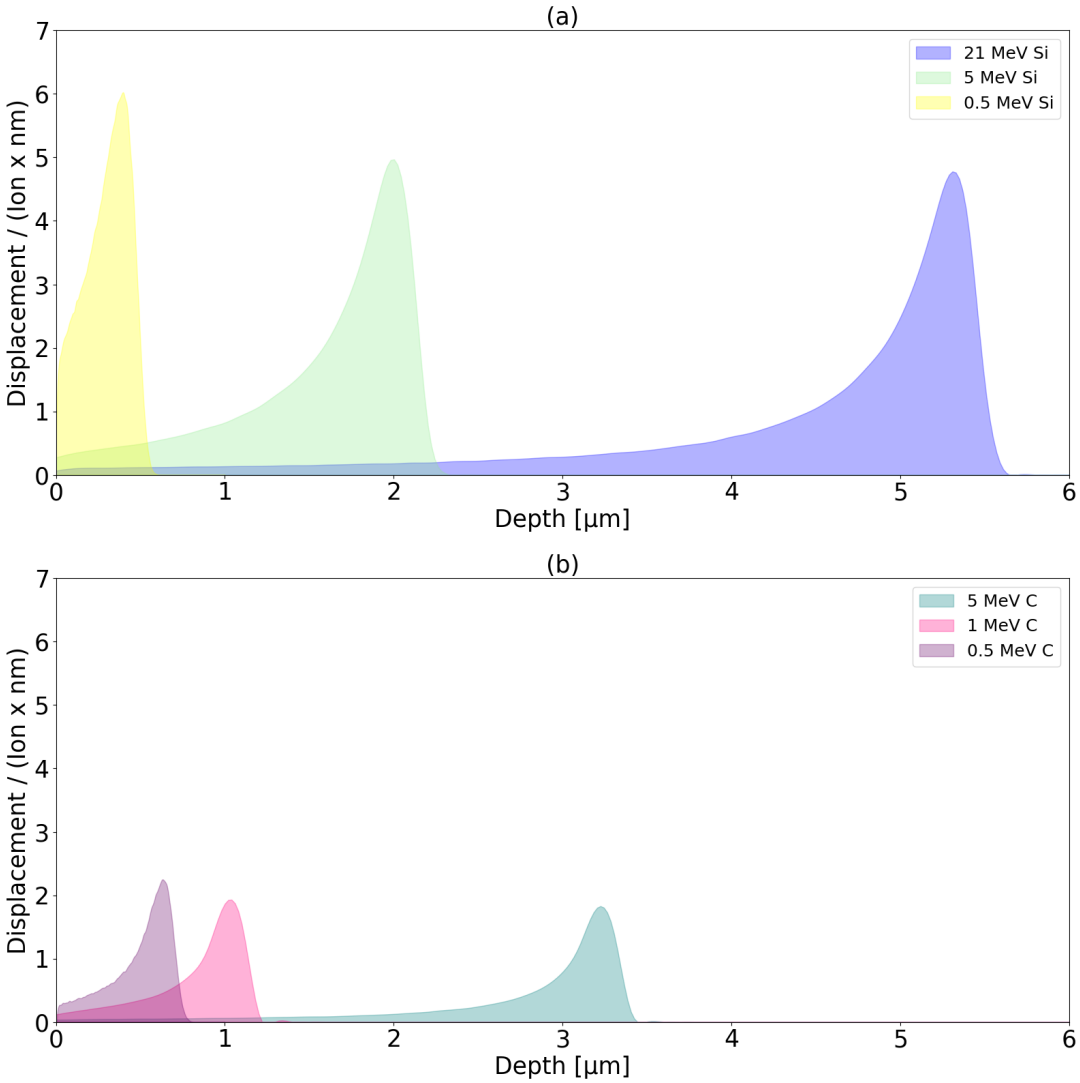

Figure 4.4: SRIM predicted displacement per ion and nm for Si (a) and C (b) in SiC.

Table 4.3: Fluence

	Si
Energy [MeV]	Fluence [cm^{-2}]
21.0	$4.50 \cdot 10^{15}$
5.0	$1.00 \cdot 10^{15}$
0.5	$1.5 \cdot 10^{14}$

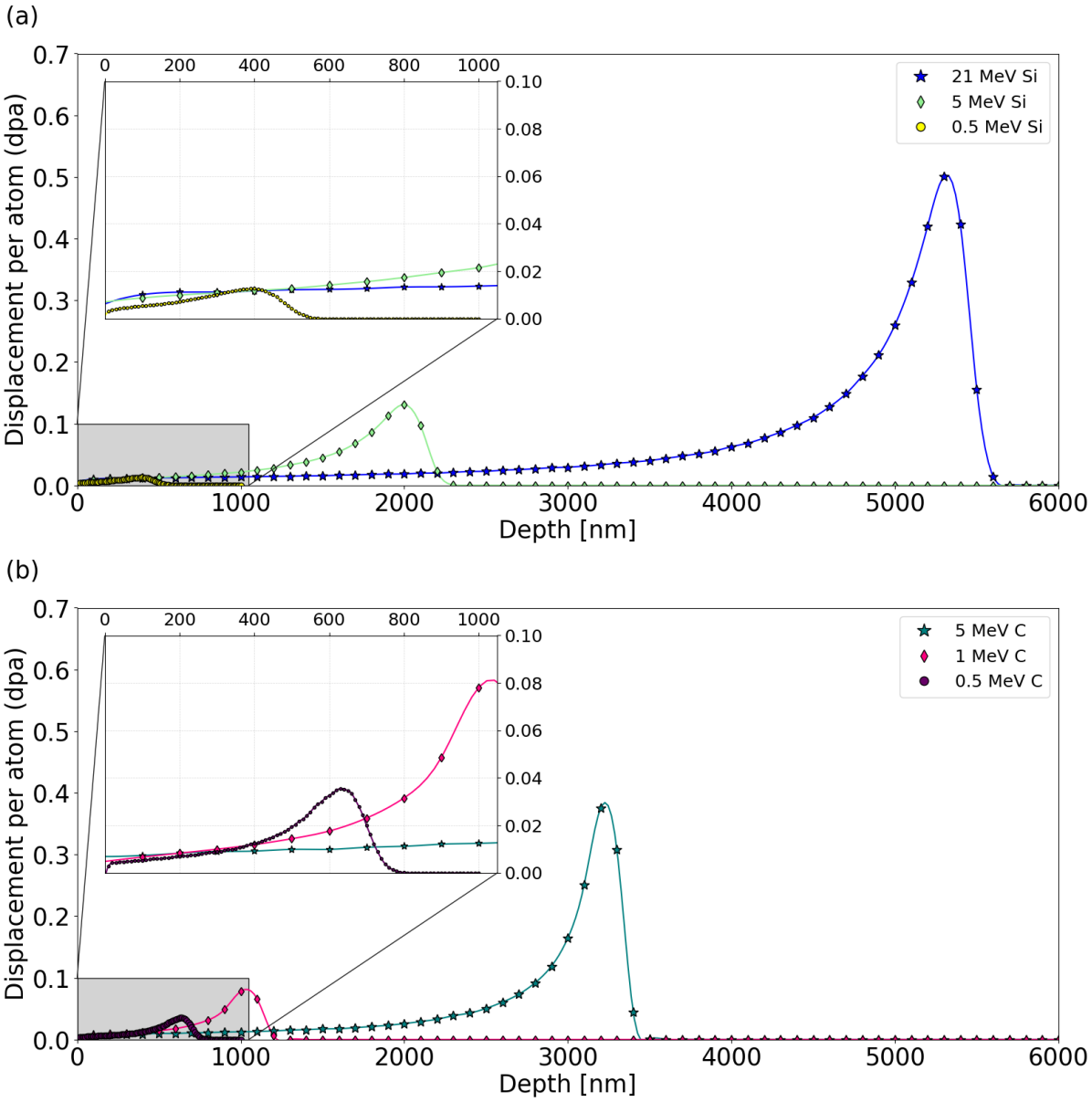

Figure 4.5: SRIM predicted damage dose (dpa) for the SiC samples irradiated with different energies of Si (a) and C (b) ions. An inset plots (highlighted in grey) represents a region investigated by RBS/C analysis.

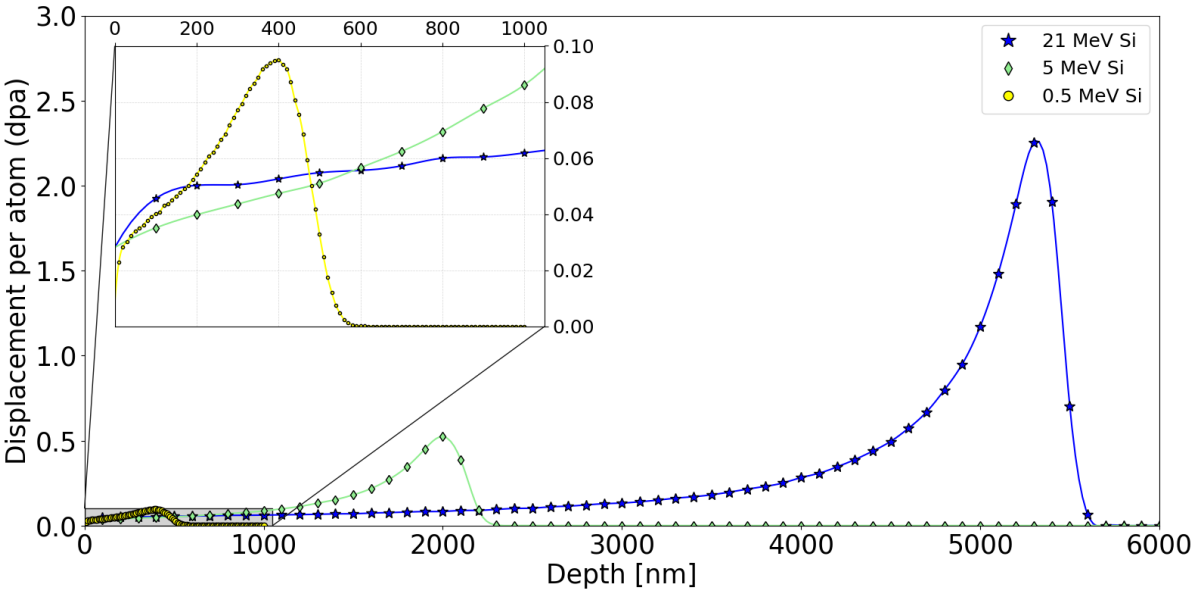

Figure 4.6: SRIM predicted damage dose (dpa) for the SiC samples irradiated with fluence presented in Tab. 4.3.

4.2 Thermal Spike

4.2.1 Thermal Spike code

TS simulations were performed using the Thermal Spike GUI v. 2.15 code developed by C. Dufour, J. Rangama and M. Touldemonde. The conditions of the use of this code are described in reference: [9]. This code solves two differential equations (Eq. 4.2 and 4.3) that calculate the heat diffusion in the atomic and electronic subsystems versus time (t) and space (r) in cylindrical geometry and heat exchange between these two subsystems by electron-phonon coupling (g), where T_a, T_e are temperatures, C_a, C_e are the specific heat and K_a, K_e are thermal conductivity for atomic and electronic subsystems, respectively.

$$C_a(T_a)\frac{\partial T_a}{\partial t} = \frac{1}{r}\frac{\partial}{\partial r}\left[rK_a(T_a)\frac{\partial T_a}{\partial r}\right] + g(T_e - T_a) \tag{4.2}$$

$$C_e(T_e)\frac{\partial T_e}{\partial t} = \frac{1}{r}\frac{\partial}{\partial r}\left[rK_e(T_e)\frac{\partial T_e}{\partial r}\right] - g(T_e - T_a) + A(r,t) \tag{4.3}$$

$A(r,t)$ is the energy deposited in the electronic subsystem and is calculated from Eq. 4.4, where S_e is a total electronic energy loss, F(r) is a radial distribution of the delta-electrons based on the Katz model [54], s is the half-width of the Gaussian time distribution. As the integration of A(r, t) in space and time should be equal to total electronic energy loss, the normalization factor b is added in Eq. 4.4 [102] [8].

$$A(r,t) = bS_e e^{-(t-t_0)^2/2s^2}F(r) \tag{4.4}$$

$$\int A(r,t)2\pi r dr dt = S_e \tag{4.5}$$

The total electronic energy losses S_e were calculated using the SRIM code (4.1). For simulations in this section, the calculations were performed for a surface or a depth of 400 nm and the suitable S_e and ion energies for this depth were used. Time t_0 is the time of the majority energy deposition in electrons and is assumed as 10^{-15} s [8]. $F(r)$ require solving the dose deposition equation (Eq. 3.7).

$$F(r) = \frac{\int_{r_{min}}^{r} 2\pi D(r)dr}{\int_{r_{min}}^{R_{MAX}} 2\pi D(r)dr} \tag{4.6}$$

$D(r)$ is the dose deposited in a coaxial cylindrical shell of thickness dr at a distance r from the ion path. The instruction of the calculation $D(r)$ as well as parameters can be

found in 3.7. In Thermal Spike GUI. v. 2.15 code for the dose calculation, the ionization potential, the mean mass atom and the density of the investigated material should be specified. The mean ionization potential was set to 9.2 eV [103], the mean molar mass of one atom was $20\,\mathrm{g\,mol^{-1}}$ and the density was set to $3.21\,\mathrm{g\,cm^{-3}}$. SiC lattice specific heat (C_a) and SiC lattice thermal conductivity (K_a) were calculated from Eq. 4.7 and Eq. 4.8, respectively [104].

$$C_a(T_a) = 925.65 + 0.3772 \cdot T_a - 7.9259 \cdot 10^{-5} \cdot T_a^2 - 3.1946 \cdot 10^7 \cdot T_a^{-2} \tag{4.7}$$

$$K_a(T_a) = \frac{1.0}{-0.0003 + 1.05 \cdot 10^{-5} \cdot T_a} \tag{4.8}$$

Electrons in SiC are considered as free electron gas with constant specific heat C_e equal to $1\,J\,cm^{-3}$ and constant electronic diffusivity D_e equal to $2\,cm^2\,s^{-1}$. Electron thermal conductivity is $K_e = C_e \cdot D_e$ [8]. Electron density was determined by taking into account one electron per atom. The value of electron-phonon coupling is the only free parameter and can be deduced from dependence on the electron-phonon mean free path (λ) in a relationship: $g = K_e/\lambda^2$. In semiconductor

$$\lambda$$

depends on the energy band gap [9] and for 3C-SiC, λ can be assumed as 5.6 nm [77].

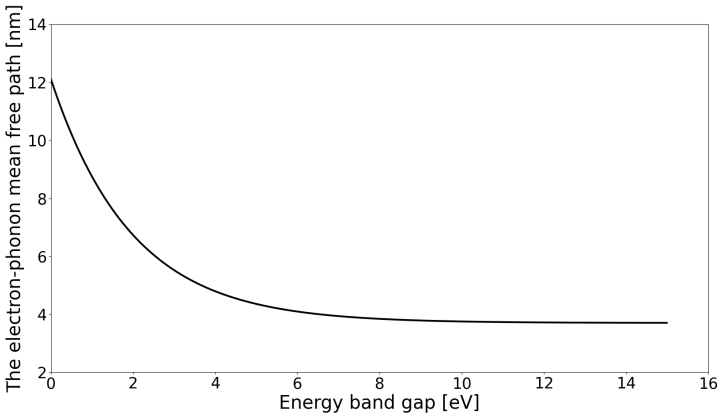

Figure 4.7: The electron-phonon mean free path in the function of energy gap [9].

Simulations were performed with a time step equal to $5 \cdot 10^{-18}$ s and a space step equal to 5 Å. The calculated temperature is equivalent to the energy received by the lattice. To determine melting or phase transformation in a material, superheat must be taken into account [105]. The lattice must reach a temperature higher than the melting point by L/C (L - latent heat, C - heat capacity).

$$(T - T_m)_{th} = L/C \tag{4.9}$$

The performed simulations assume superheating and no occurence of phase change or melting. All the parameters refer to solid SiC. The main point of the performed simulations is to check if the temperature increases up to the decomposition of SiC.

4.2.2 Initial temperature effects

Effects of energy increase on the target lattice strongly depend on the initial temperature. The necessary energy gain to achieve the temperature of melting or phase changing depends on the initial target temperature [106] [107]. Eq. 4.10 shows that the energy necessary to melt the lattice dH_f is a sum of the energy necessary to increase the temperature to melt lattice $\int cdT$ and the latent heat [107].

$$dH_f = \int cdT + L_f \tag{4.10}$$

Temperatures and energies in the centre of the ion trajectory are presented in Table 4.4 and Table 4.5 for the surface, and in Table 4.6 and Table 4.7 at the depth of 400 nm, for the initial target temperature set to 300 K (RT) and 1075 K (HT), respectively.

Table 4.4: Temperatures and energies in the center of the ion trajectory calculated from inelastic thermal spike model for the initial temperature of the SiC sample: 300 K at the surface.

Ion	Ion energy [MeV]	Electronic stopping power [keV/Å]	Temperature [K]	Energy per atom [eV]
Si	21.0	0.51	984	0.22
Si	5.0	0.39	966	0.22
Si	0.5	0.11	522	0.12
C	5.0	0.18	551	0.12
C	1.0	0.15	566	0.13
C	0.5	0.11	515	0.12

For irradiation performed in HT, the maximum temperature that occurs in the ion path is much higher than in the case of irradiation at RT, but still is not enough to melt SiC. However, temperature in the ion path may affect defect dynamics. Taking into account the change in the electron stopping power with depth in the sample, a maximum

Table 4.5: Temperatures and energies in the center of the ion trajectory calculated from inelastic thermal spike model for the initial temperature of the SiC sample: 1075 K at the surface.

Ion	Ion energy [MeV]	Electronic stopping power [keV/Å]	Temperature [K]	Energy per atom [eV]
Si	21.0	0.51	1827	0.48
Si	5.0	0.39	1827	0.48
Si	0.5	0.11	1349	0.35
C	5.0	0.18	1376	0.36
C	1.0	0.15	1397	0.36
C	0.5	0.11	1339	0.35

Table 4.6: Temperatures and energies in the center of the ion trajectory calculated from inelastic thermal spike model for the the initial temperature of the SiC sample: 300 K at depth 400 nm.

Ion	Ion energy [MeV]	Electronic stopping power [keV/Å]	Temperature [K]	Energy per atom [eV]
Si	21.0	0.51	1001	0.23
Si	5.0	0.35	933	0.21
C	5.0	0.18	549	0.12

Table 4.7: Temperatures and energies in the center of the ion trajectory calculated from inelastic thermal spike model for thethe initial temperature of the SiC sample: 1075 K at depth 400 nm.

Ion	Ion energy [MeV]	Electronic stopping power [keV/Å]	Temperature [K]	Energy per atom [eV]
Si	21.0	0.51	1840	0.48
Si	5.0	0.35	1801	0.47
C	5.0	0.18	1365	0.35

temperature in the ion path dependence on depth can be observed.. At 21 MeV, the temperature remains the same at the surface and at the depth of 400 nm, while at 500 keV the temperature difference exceeds 100 K.

4.2.3 The radial distribution of energy per atom in the ion path

This section presents results with thermal conductivity set to 0 and for an initial temperature equal to 300 K. Fig. 4.8 shows the radial distribution of total energy that was deposited in atoms near the surface and Fig. 4.9 shows the radial distribution of total energy at 400 nm. Calculations for ions with low electronic stopping power are omitted. The energy deposition occurs in a small radius around the ion path. The visible increase in energy occurs within a radius of several dozen nanometers. An interesting observation is that the maximum energy loss for 5 MeV Si is greater than that for 21 MeV Si. The same tendency is observed for 1 MeV C and 5 MeV C ions. More energy is deposited in a smaller space. For ions with higher energy, the energy distribution is more dispersed.

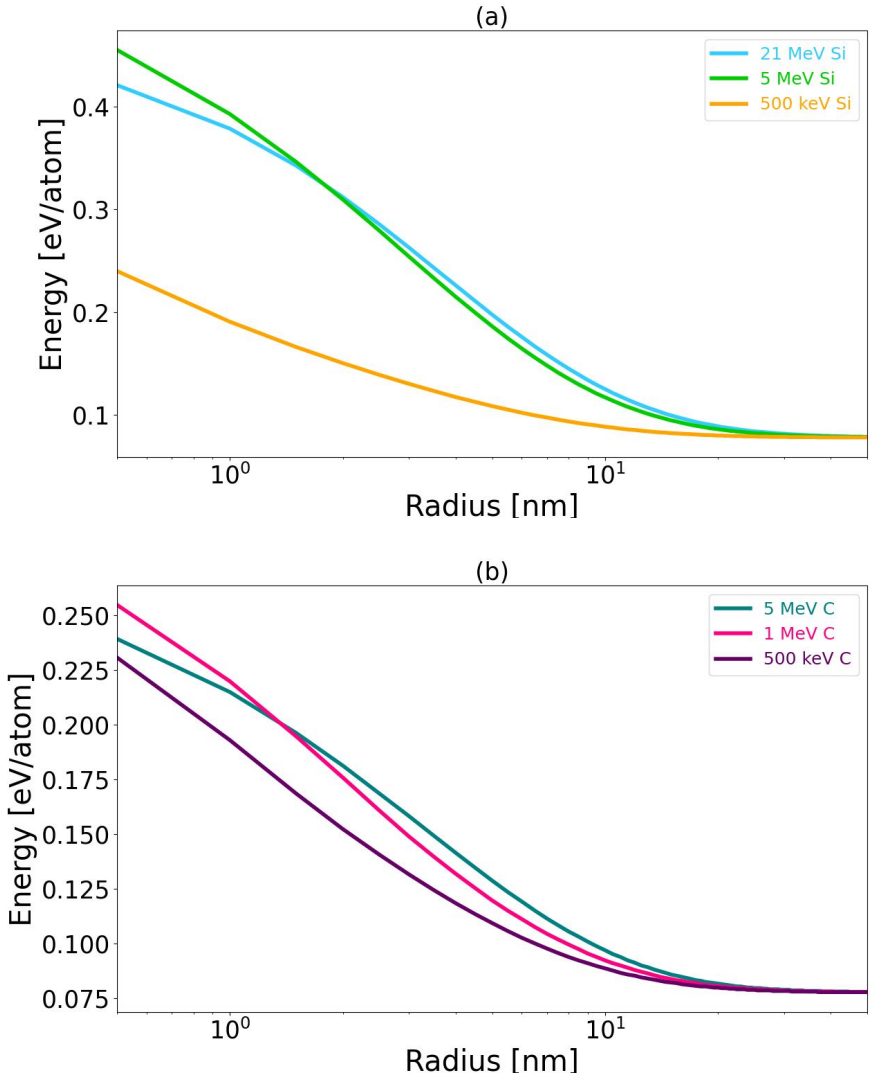

Figure 4.8: Radial distribution of energy after Si and C ion irradiation. Initial temperature of the SiC sample: 300 K near the surface.

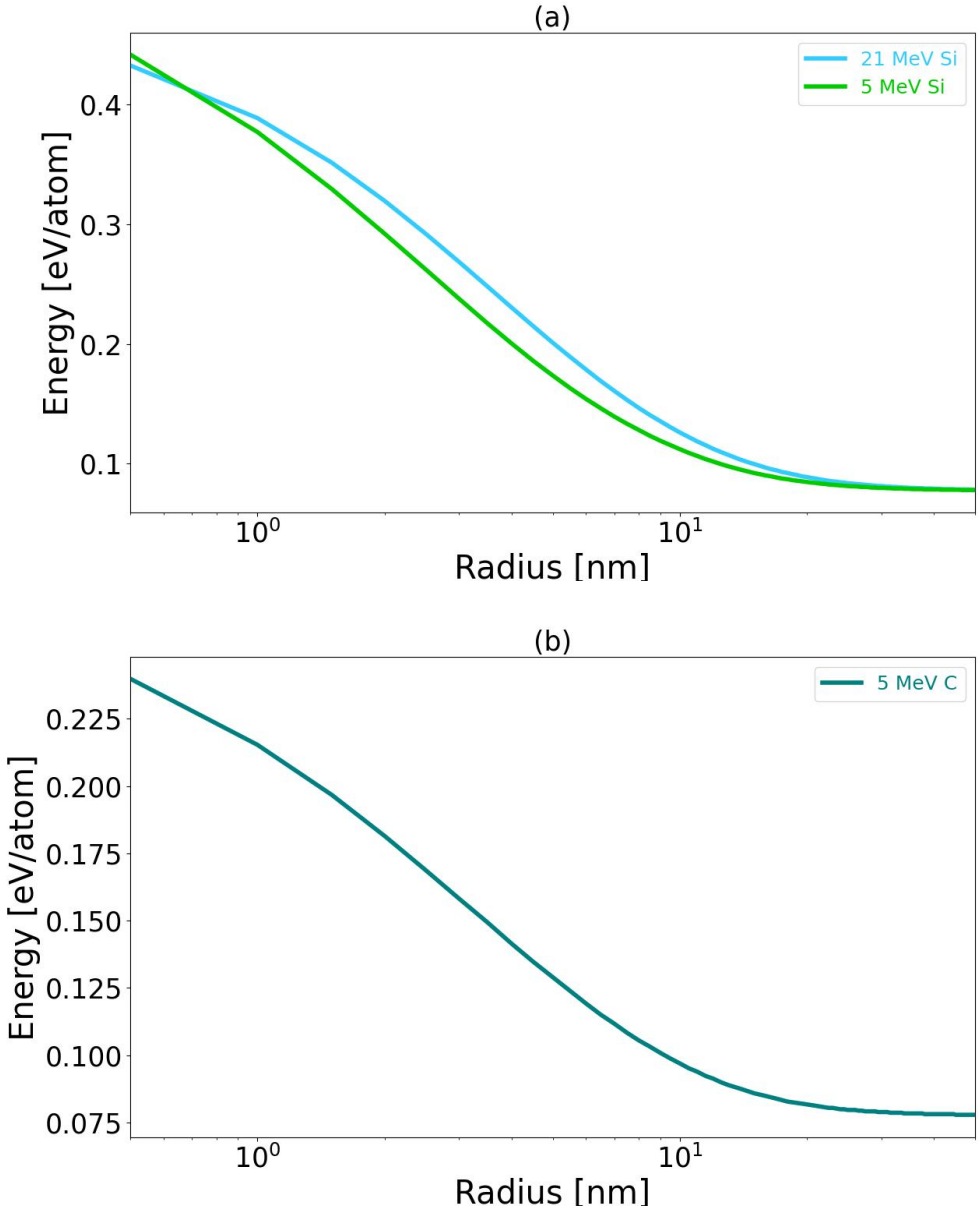

Figure 4.9: The radial distribution of energy after Si and C ion irradiation. The initial temperature of the SiC sample: 300 K at the depth 400 nm.

4.2.4 The radial distribution of temperature in ion track in timescale

Fig. 4.10 presents temperature distribution in the electronic and atomic subsystems in space and time for 21 MeV Si path. The maximum temperature for the electronic subsystem is achieved about 10^{-15} s, while the maximum lattice temperature occurs about between 10^{-14} s to 10^{-13} s.

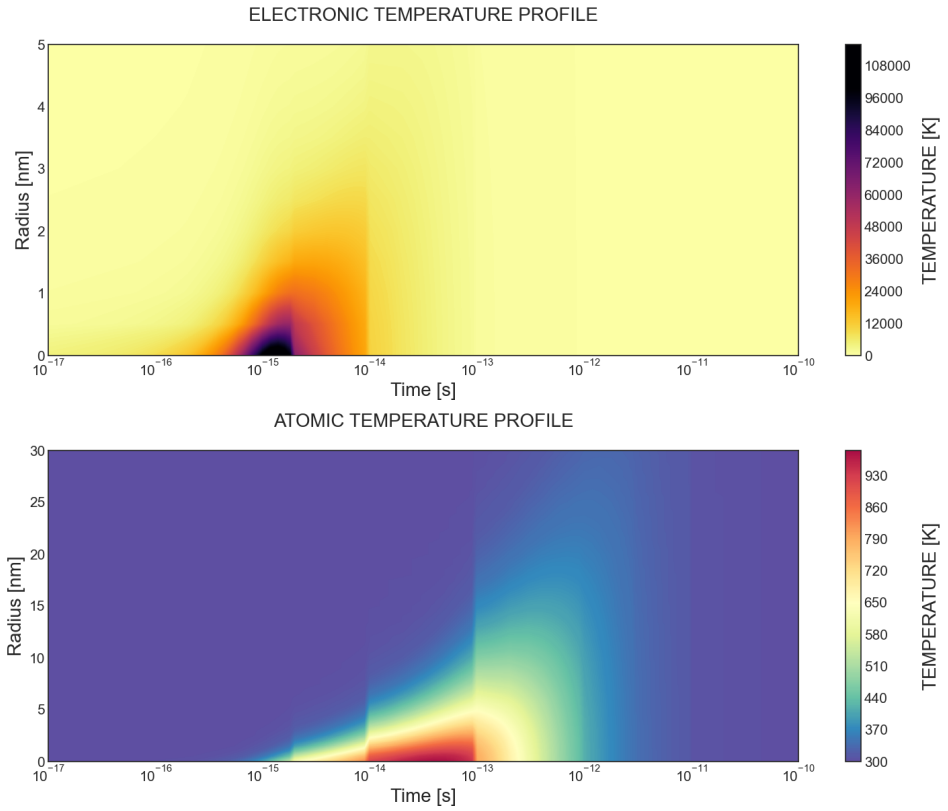

Figure 4.10: Temperature increase after Si and C ion passage 21 MeV Si

4.2.5 Effects of electron-phonon coupling

Amorphous materials are more sensitive to the effects of thermal spike than crystalline materials [9]. Different crystal structures may have different electron-phonon coupling. The influence of thermal spikes depends in particular on the electron-phonon coupling, denoting the effectiveness of energy transference between electronic and atomic subsystems. In antecedent simulations, it was assumed that the electron-phonon coupling has a constant value and can be computed using Eq. 4.11. Mean free path λ is dependent on the inverse of the band gap energy [8] [108]. For λ equal 5.6 nm, g is equal to 6 $\cdot 10^{12}\,\mathrm{W\,cm^{-3}\,K^{-1}}$.

$$g = \frac{C_e D_e}{\lambda^2} \tag{4.11}$$

In fact, the electron-phonon coupling parameter exhibits variability and is contingent upon several factors, including electron temperature and structural defects within the crystal lattice [109] [110] [111] [112]. At RT, the dissimilarity in the g value between pristine SiC and SiC with 12.5 % of vacancies reaches an order of magnitude of 10^6. For pristine SiC, g is equal to $10^7\,\mathrm{W\,cm^{-3}\,K^{-1}}$ and for defective structure is $10^{13}\,\mathrm{W\,cm^{-3}\,K^{-1}}$ at 300 K. However, the transfer of energy from the electron subsystem to the atomic one

occurs when electrons have temperatures of around 10^5 K or several thousand K. Then this difference is smaller. At higher temperatures (at 10^5 K), g for pristine SiC is equal to 10^{16} W cm^{-3} K^{-1}, while for defective SiC is 10^{18} W cm^{-3} K^{-1} [110] [111]. Consequently, in this section, simulations were conducted while manipulating the g values within a specified range. It becomes apparent that defects within SiC can amplify the consequences of thermal spike annealing. The temperature elevation along the ion trajectory is contingent upon the electron-phonon coupling as shown in Fig. 4.11

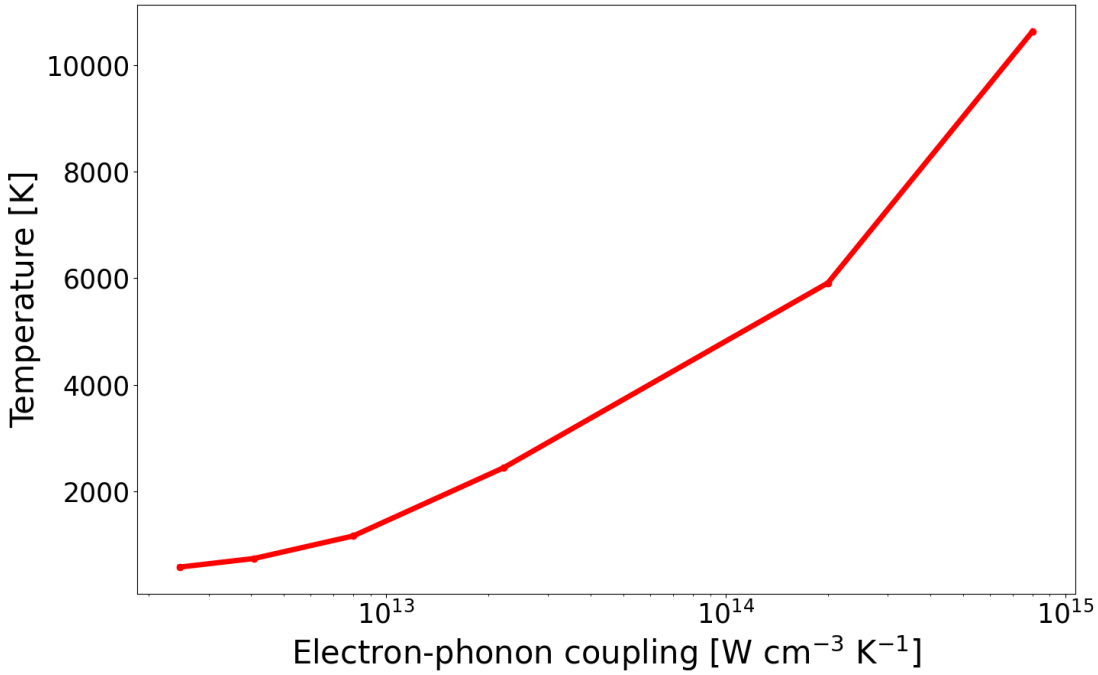

Figure 4.11: The maximum temperature in the centre of the ion path as a function of electron-phonon coupling.

The results of the maximum temperature in the centre of the ion path are also presented depending on the mean free path (Fig. 4.12). A significant impact of the selected electron-phonon coupling value or the electron mean free path on the calculated temperature values in the atomic lattice can be observed. For the higher values of the mean free path, the electron-phonon coupling has smaller values and energy dissipation in the electrons subsystem occurs more rapidly than energy transfer to the atomic lattice. The consequence is the reduction of atomic temperature increase in the ion path. Thus, defects also play a role in the effects of ion irradiation.

Figs. 4.13 and 4.14 show the distribution of electronic temperature in space and time, while in Figs. 4.15 and 4.16 atomic temperature distribution is presented. The simulations show that temperature distribution significantly depends on the mean free path. As the

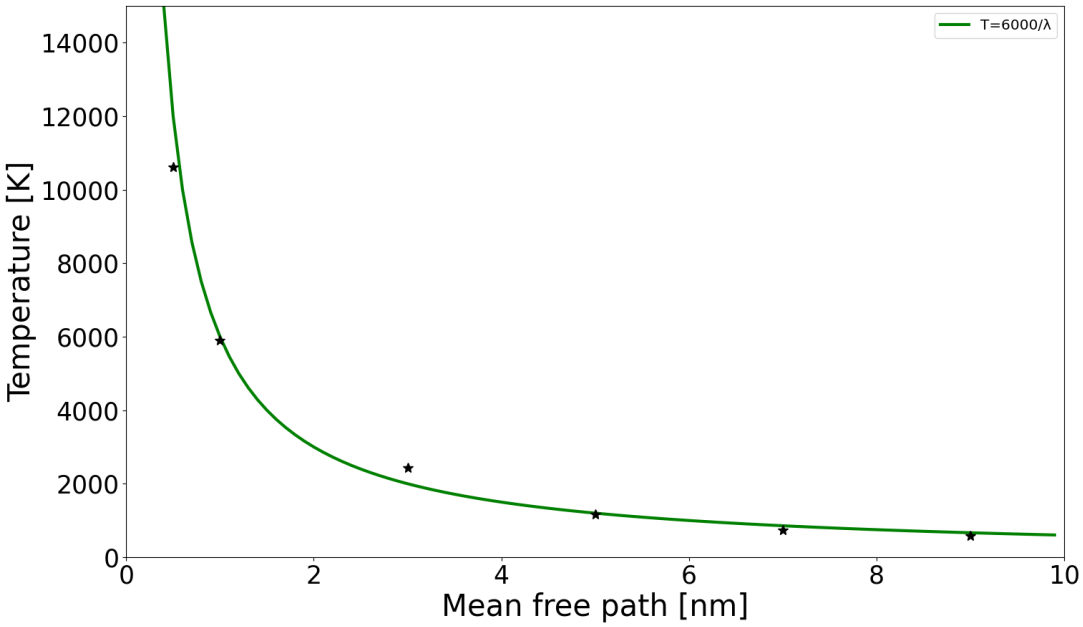

Figure 4.12: The maximum temperature in the centre of the ion path as a function of the electron mean free path.

mean free path is high, there is a greater distribution of heat in the electron lattice and the area in which the transfer of energy from electrons to the atomic lattice occurs is greater. Consequently, there is a lower temperature in the centre, but heating occurs over a larger area. For small values of the mean free path, the energy transfer occurs in a smaller radius, and the temperature at the centre of the ion path is much larger. It should be noted that the calculations were made for mean free path values that exceed the actual range of this value for SiC.

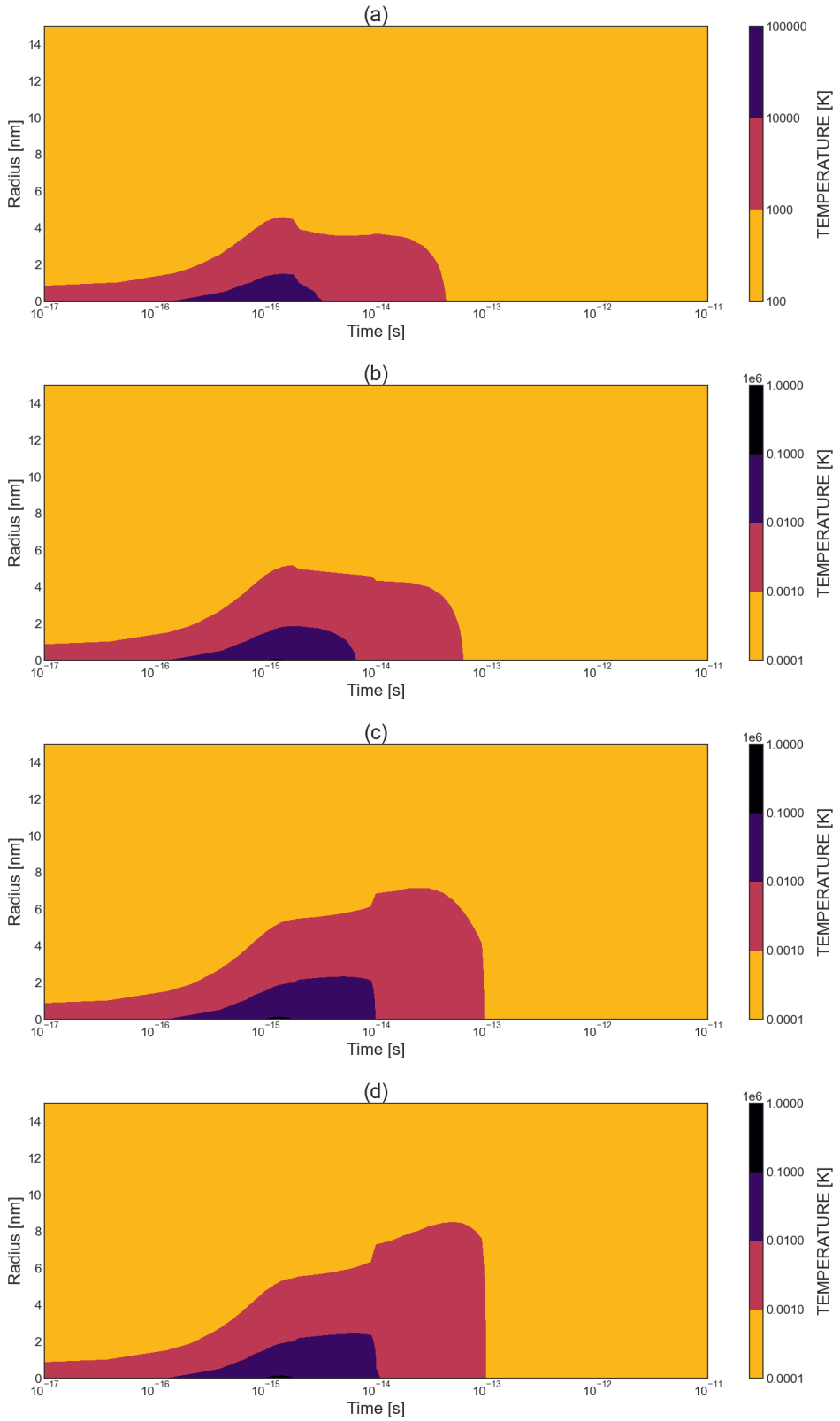

Figure 4.13: Distribution of the electronic temperature in the space and time for 21 MeV Si irradiation with a mean free path equal to a) 0.5 nm, b) nm, c) 3 nm, d) 5 nm, e) 7 nm, f) 9 nm, and g) 50 nm.

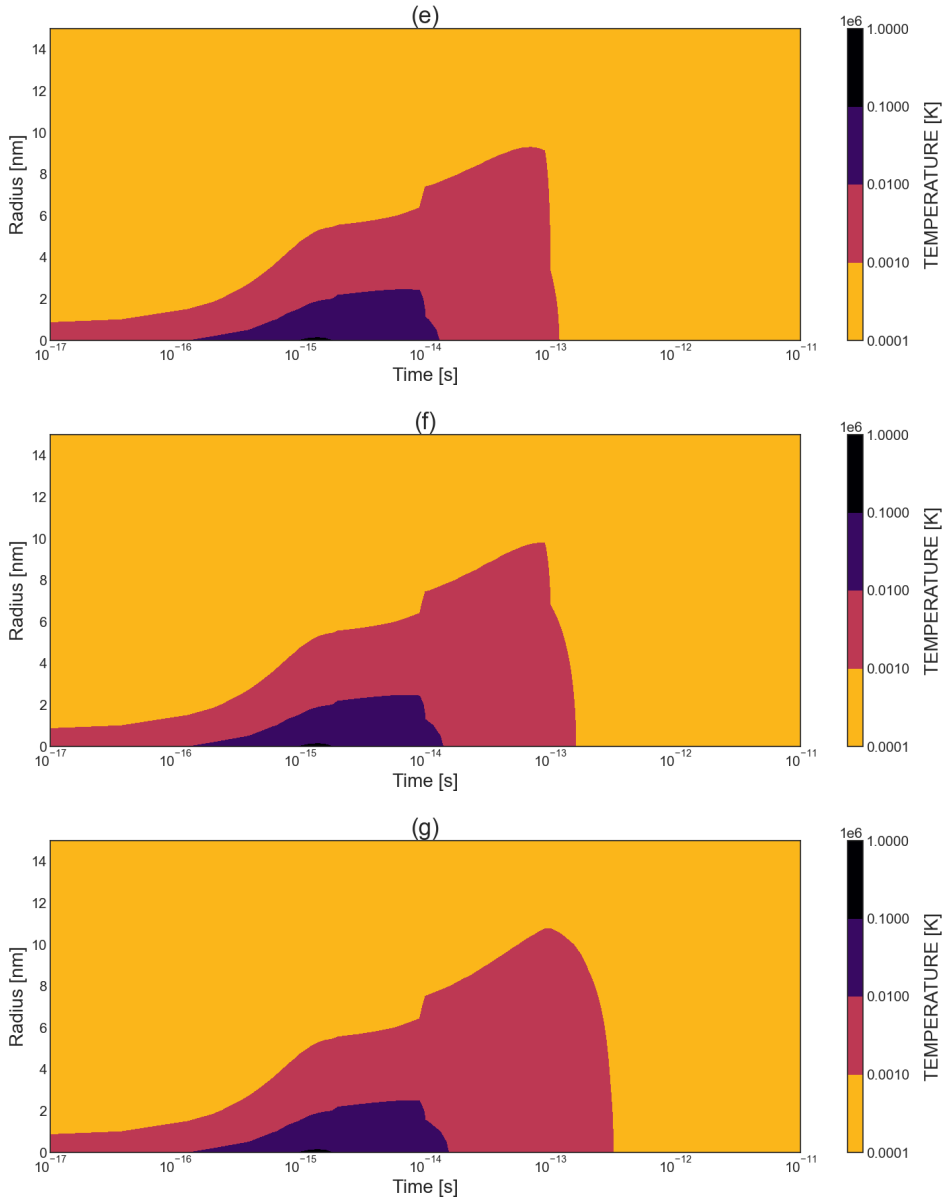

Figure 4.14: Distribution of the electronic temperature in the space and time for 21 MeV Si irradiation with a mean free path equal to a) 0.5 nm, b) 1 nm, c) 3 nm, d) 5 nm, e) 7 nm, f) 9 nm, and g) 50 nm.

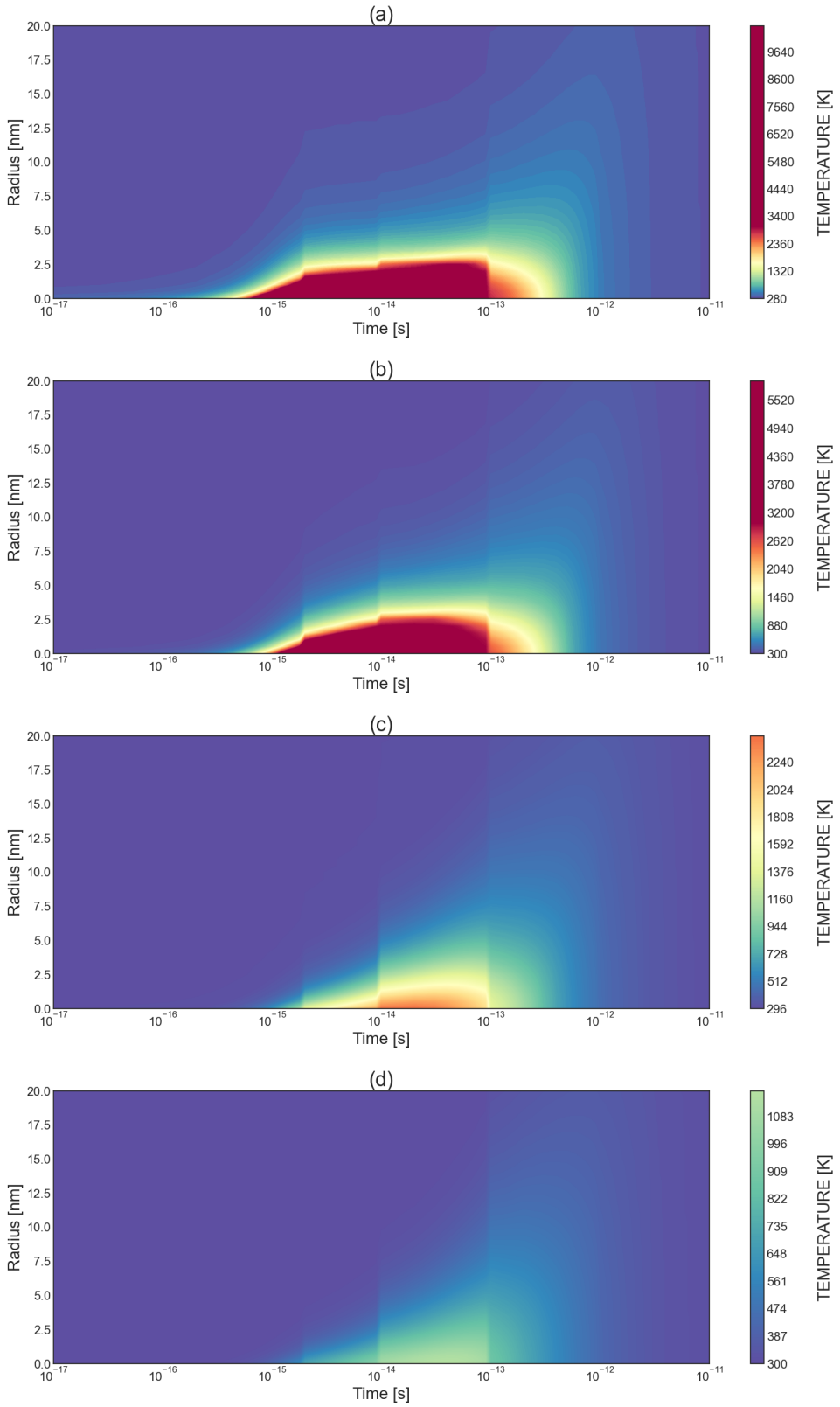

Figure 4.15: Distribution of the atomic temperature in the space and time for 21 MeV Si irradiation with a mean free path equal a) 0.5 nm, b) 1 nm, c) 3 nm, d) 5 nm, e) 7 nm, f) 9 nm, and g) 50 nm

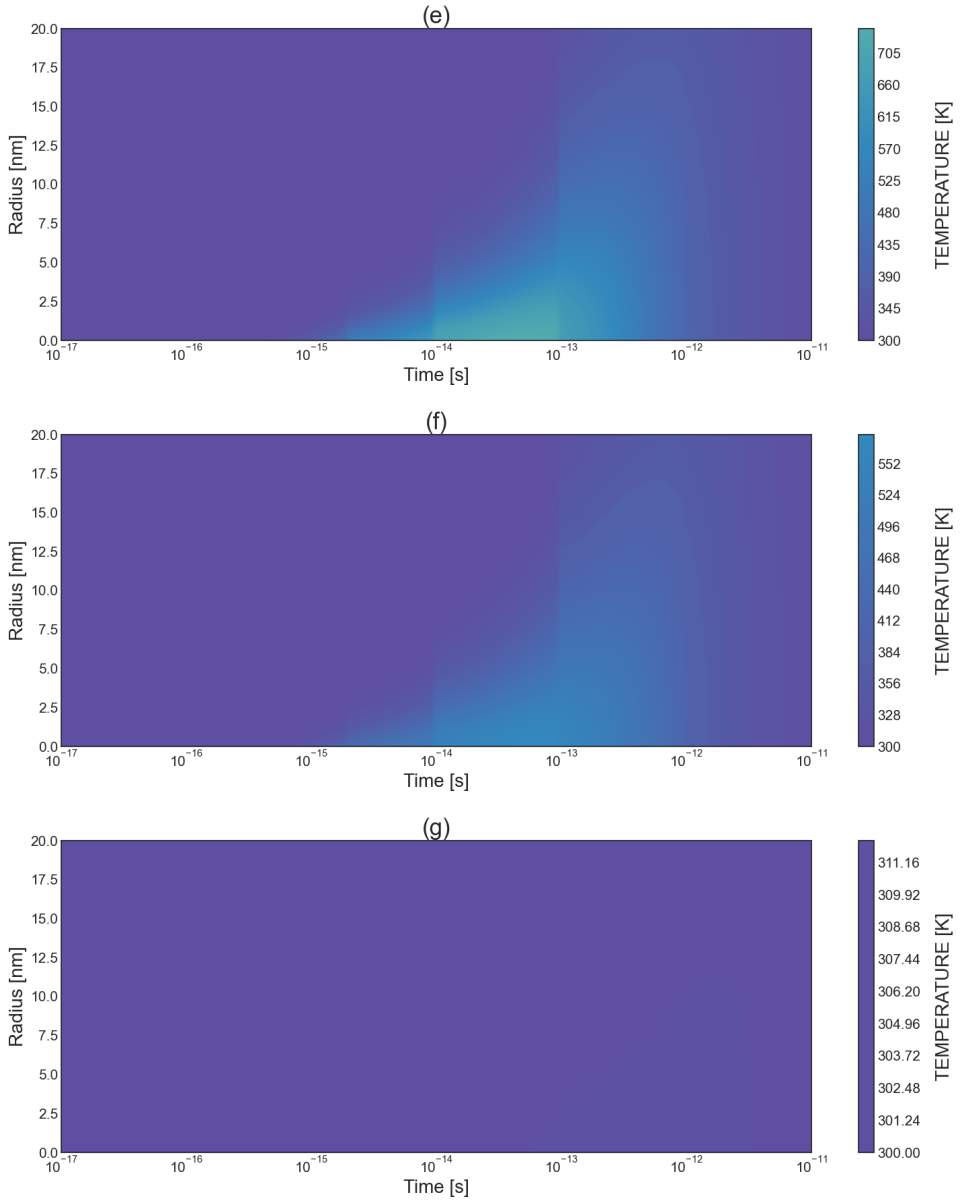

Figure 4.16: Distribution of the atomic temperature in the space and time for 21 MeV Si irradiation with a mean free path equal to a) 0.5 nm, b) 1 nm, c) 3 nm, d) 5 nm, e) 7 nm, f) 9 nm, and g) 50 nm

4.3 Molecular dynamics

4.3.1 LAMMPS introduction

LAMMPS (Large-scale Atomic/Molecular Massively Parallel Simulator) is a classical Molecular Dynamics (MD) simulation code designed to efficiently compute Newton equations of motion for a system of interacting particles [113] [114]. For each step, LAMMPS computes the positions and velocities of each atom by integrating Newton equations of motion. The forces acting on atoms are determined by potentials (force fields) estimated by experiments or quantum mechanics calculations. In LAMMPS, the Varlet algorithm was implemented for integrating Newton equations of motion. LAMMPS is great for computing on parallel processors. Here, most of the simulations were performed using the Świerk Computing Centre (CIŚ) cluster. Performing calculations on a supercomputer allows the use of huge sample sizes containing several or several million atoms. Post-processing of LAMMPS output data was done by Python code and OVITO (Open Visualization Tool) [115]. LAMMPS is widely used for SiC study for irradiation simulation, abrasive etc. [116].

4.3.2 OVITO

OVITO (Open Visualization Tool) is a software for post-processing data obtained from MD simulations [115]. This tool not only allows visualizing the results, but also performs simple calculations as well as more complex processes such as Wigner-Seitz analysis, which identifies point defects in the crystal structure. This method consists of comparing the displaced frame with the reference frame. The Vornoi diagram is determined from the first frame and shows the division of the plane of cells, with each cell surrounding one atom and being a space closer to that atom than any other. In the next step, the program calculates the number of atoms in each Vornoi cell in the displaced frame. The output can be interstitials or vacancies. The Wigner-Seitz analysis scheme is shown in Fig. 4.17.

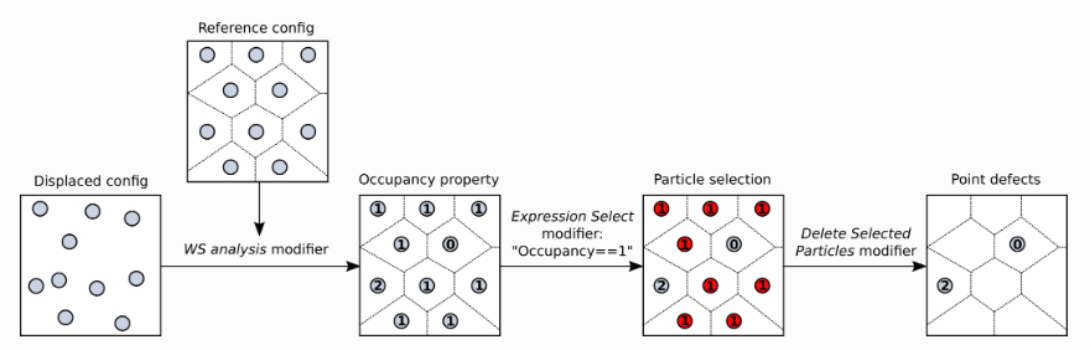

Figure 4.17: Wigner-Seitz cell method [117].

Another method of assessing the quality of a crystal structure is to identify diamond structure (IDS). The description of IDS method can be found in Ref. [118]. Fig. 4.18 shows an example of using the IDS method to detect defects in SiC.

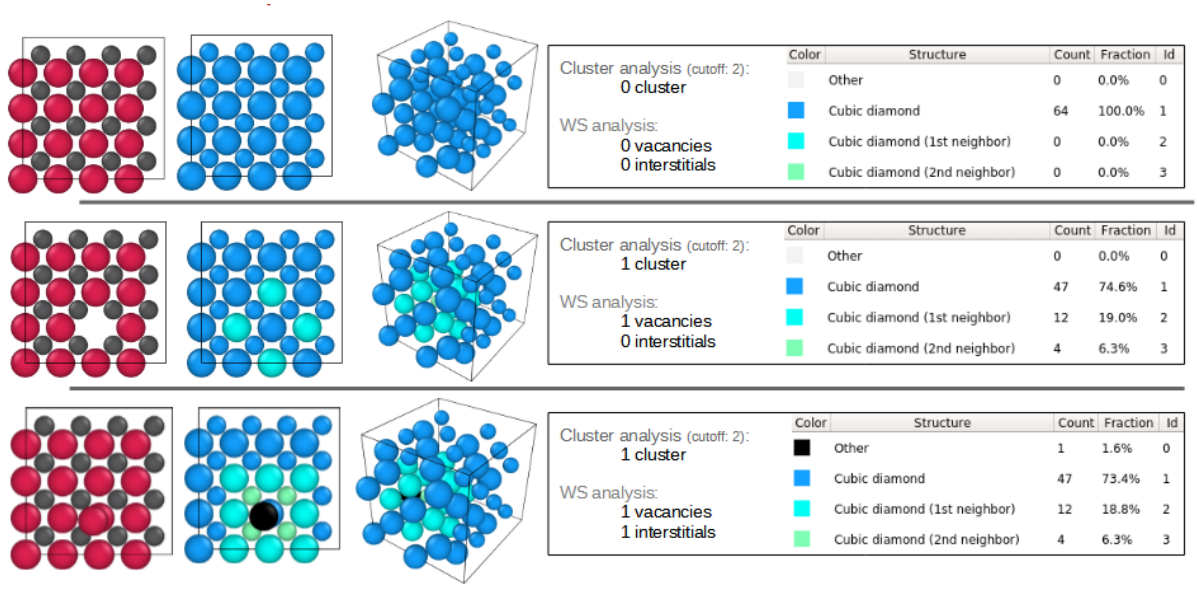

Figure 4.18: Identity diamond structure method. The figure at the top shows a perfect crystal lattice, in the middle part, one atom has been removed, and in the lower part, one atom has been displaced.

4.3.3 Ensembles

Different conditions in MD simulation that can be carried out are referred to ensembles. Ensembles are linked between microscopic quantities that characterize atoms in MD simulations (such as velocities, acceleration, forces, positions and angular momenta) and macroscopic values like temperature and pressure. The most commonly used ensembles are: microcanonical (NVE), canonical (NVT) and isothermal-isobaric (NPT). Each ensemble is characterised by three variables for example NVE (N - number of particles, V - volume and E - total energy). In NVT ensemble, to achieve constant temperature, a temperature control algorithm named a thermostat is needed, and in NPT a pressure control algorithm named a barostat is added, respectively. The sum up of ensembles constant is presented in table 4.8.

In LAMMPS, the total energy can be described by Eq. 4.12, temperature is computed as Eq. 4.13 and pressure is determined by Eq. 4.14, where N_{DIS} is number of degrees of freedom, r_{ij} is a distance and f_{ij} is a force between sites i and j.

Table 4.8: Ensembles

Ensemble	Function of equilibrium	Constant
Microcanocical	S - enthropy	N, V, E
Canonical	F - Helmholtz free energy	N, V, T
Isothermal-isobaric	G - Gibbs free energy	N, P, T

$$E = U_{pot} + E_{kin} = \sum_i \sum_{j>i} U(r_i j) + \sum_i \frac{1}{2} m_i v i^2 \tag{4.12}$$

$$T = \frac{\sum_i \frac{1}{2} m_i v i^2}{3 N_{DOS} k_B} \tag{4.13}$$

$$P = P^{ideal} + P^{conf} = \rho k_B T - \frac{1}{3} \sum_i \sum_{j>i} r_{ij} f_{ij} \tag{4.14}$$

4.3.4 Potentials functions for SiC

The choice of potential is very important for the reliability of MD results and for the accuracy of the calculation. For SiC widely used potentials are: Tersoff [119], modified-embedded atom method (MEAM) and Gao-Weber [120]. These potentials can be joined with Ziegler, Biersack and Littmark (ZBL) potential to improve weak repulsion [121]. Samolyuk et al. published a comparison of interatomic potential for characterizing primary radiation damage and recommended Gao-Weber potential as the most realistic [122]. Thus, in this work Gao-Weber potential with ZBL are applied [123].

The Gao-Weber potential is many body inter-atomic potential based on Brenner potential formalism. The potential energy is a sum over individual bonds, where V^A is attractive potential and V^R is repulsive potential. R^e is distance and D^e is dimer bond energy. β, S, R^1, R^2 are adjustable parameters.

$$E = \sum_i \sum_{j(>i)} f_{ij} r_{ij} \left[V^R(r_{ij}) - \bar{B}_{ij} V^A(r^{ij}) \right] \tag{4.15}$$

$$V^R = \frac{D^e}{S-1} exp\left[\beta \sqrt{2S} (r - R^e) \right] \tag{4.16}$$

$$V^A = \frac{D^e S}{S-1} exp\left[\beta \sqrt{2/S} (r - R^e) \right] \tag{4.17}$$

$$f(r) = \begin{cases} 1 & : \quad r < R^1 \\ 0.5(1 + \cos[\frac{\pi(r-R1)}{R^2-R^1}]) & : \quad R^1 < r <= R^2 \\ 0 & : \quad r > R^2 \end{cases} \tag{4.18}$$

$$\bar{B}_{ij} = 0.5[B_{ij}^{-\delta_j} + B_{ji}^{-\delta_j}] \tag{4.19}$$

$$B_{ij} = 1 + \sum_{k \neq i,j} f_{ik}(r_{ik}) g_i(\theta_{ijk}) \tag{4.20}$$

$$g(\theta) = \alpha \left[1 + \frac{c^2}{d^2} - \frac{c^2}{[d^2 + (1 + \cos\theta)^2]} \right] \tag{4.21}$$

The Ziegler-Biersack-Littmark (ZBL) potential is a screened nuclear repulsion for high-energy collisions between atoms.

$$E_{ij}^{ZBL} = \frac{1}{4\pi\epsilon_0} \frac{Z_1 Z_2 \, e^2}{r_{ij}} \phi(r_{ij}/a) + S(r_{ij}) \tag{4.22}$$

$$a = \frac{0.46850}{Z_i^{0.23} + Z_j^{0.23}} \tag{4.23}$$

$$\phi(x) = 0.18175e^{-3.19980x} + 0.50986e^{-0.94229x} + 0.28022e^{-0.40290x} + 0.02817e^{-0.20162x} \tag{4.24}$$

4.3.5 SiC samples

Silicon Carbide sample was generated for LAMMPS data input file by Atomsk code [124]. For each simulation, SiC is monocrystalline 3C-SiC (zinc-blende structure). The SiC data of crystal structure are taken from Crystallography Open Database [125] [126].

4.3.6 Collision cascade induced by 5 keV Ar

Collision cascade was simulated in LAMMPS with using 5 keV Ar ions. 3C-SiC sample with size of (434 x 434 x 652) Å, including $1.2 \cdot 10^7$ atoms was generated by Atomsk. Before irradiation sample was equilibrated in NPT ensemble at 300 K for 50 ps. Irradiation were performed in NVE ensemble. Scheme of irradiation is presented in Fig. 4.19.

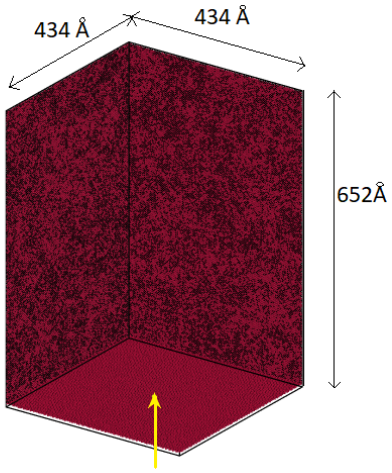

Figure 4.19: Schematic figure of the irradiation model. The yellow arrow represents the Ar ion movement.

The evolution of damage is shown in Fig. 4.20 and in Fig. 4.21. The pristine 3C-SiC sample (Fig. 4.21a) is damaged by the collision cascade. The atoms with kinetic energy higher than 0.5 eV are presented in Fig. 4.22. During simulations, the maximum damage is observed in 0.2 ps, as shown in Fig. 4.20. After the peak, the number of defects decreases to finally achieve a stable number, when the kinetic energy of atoms is less than 0.5 eV (Figs. 4.21d, 4.22d).

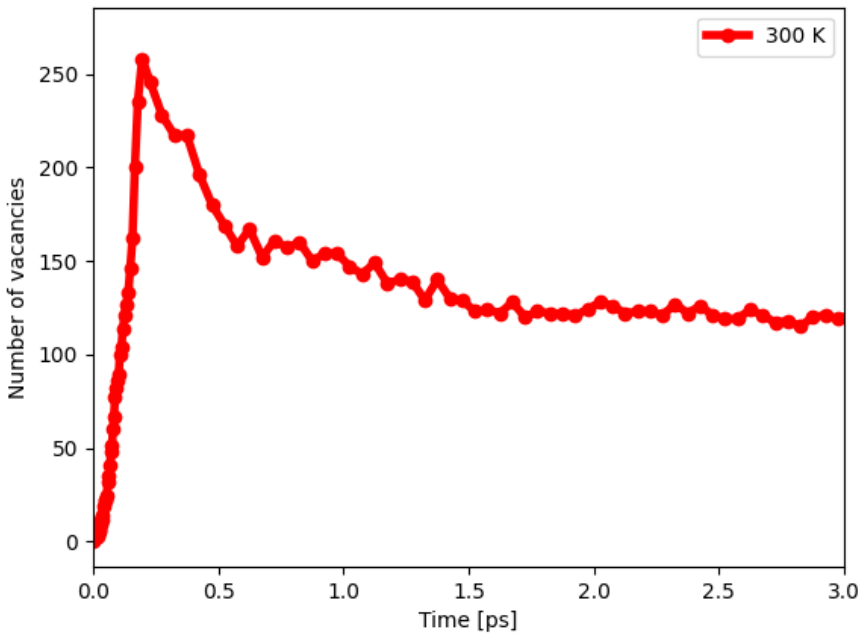

Figure 4.20: Number of vacancies as a function of time during 5 keV Ar irradiation of 3C-SiC.

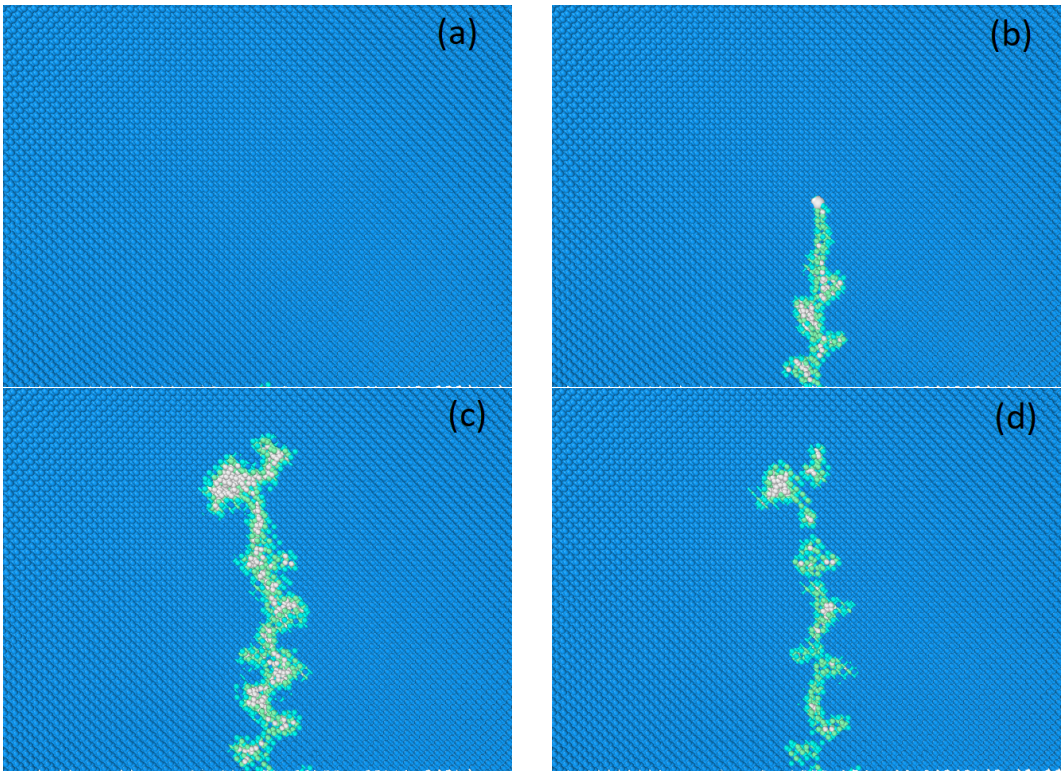

Figure 4.21: SiC structure damage at time: a) 0.00 ps, b) 0.06 ps, c) 0.20 ps, d) 3.20 ps.

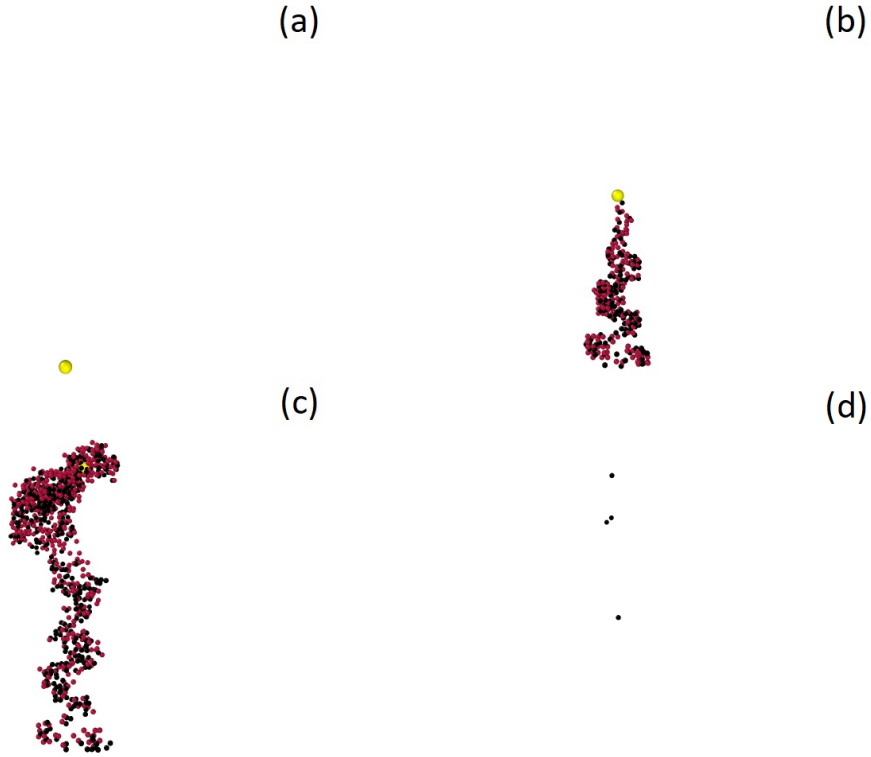

Figure 4.22: Visualisation of kinetic energy - collision cascade induced by 5 keV ions at time: a) 0.00 ps, b) 0.06 ps, c) 0.20 ps, d) 3.20 ps.

The dependence of temperature was also studied. Ar irradiation was simulated in 3C-SiC equilibrated at 600 K. The number of vacancy as a function of time for collision cascade at 300 K and at 600 K is shown in Fig. 4.23. The maximum number of defects is similar for both temperatures, but after the equilibrium, smaller number of defects can be observed at 600 K.

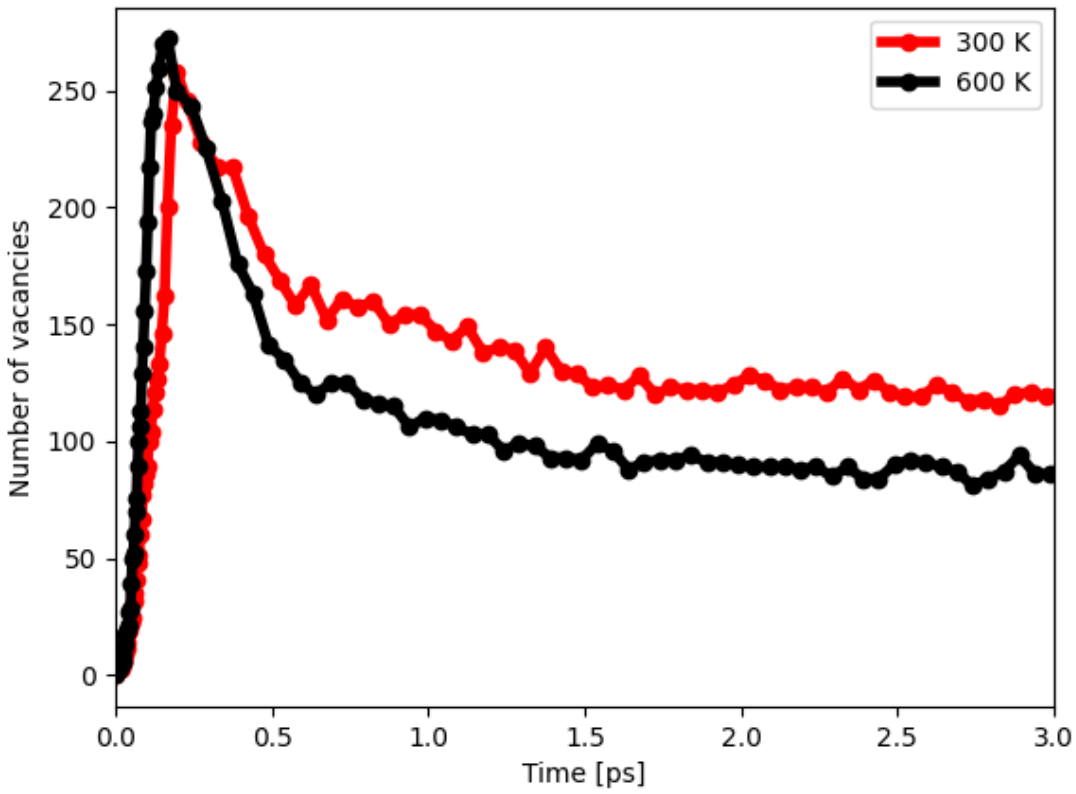

Figure 4.23: Number of vacancies as a function of time during 5 keV Ar irradiation of 3C-SiC at 300 K and at 600 K.

4.3.7 Electronic Stopping

To simulate the electronic stopping effects, the additional force was added to Newton equations of motion to reduce the ion velocity. The electronic stopping power of the incident ions can be determined by using SRIM. Results from simulations with 20 keV Ar ion irradiation are presented in Fig. 4.24. As the effect of reduction of ion velocity, less number of vacancies is produced during collision cascade.

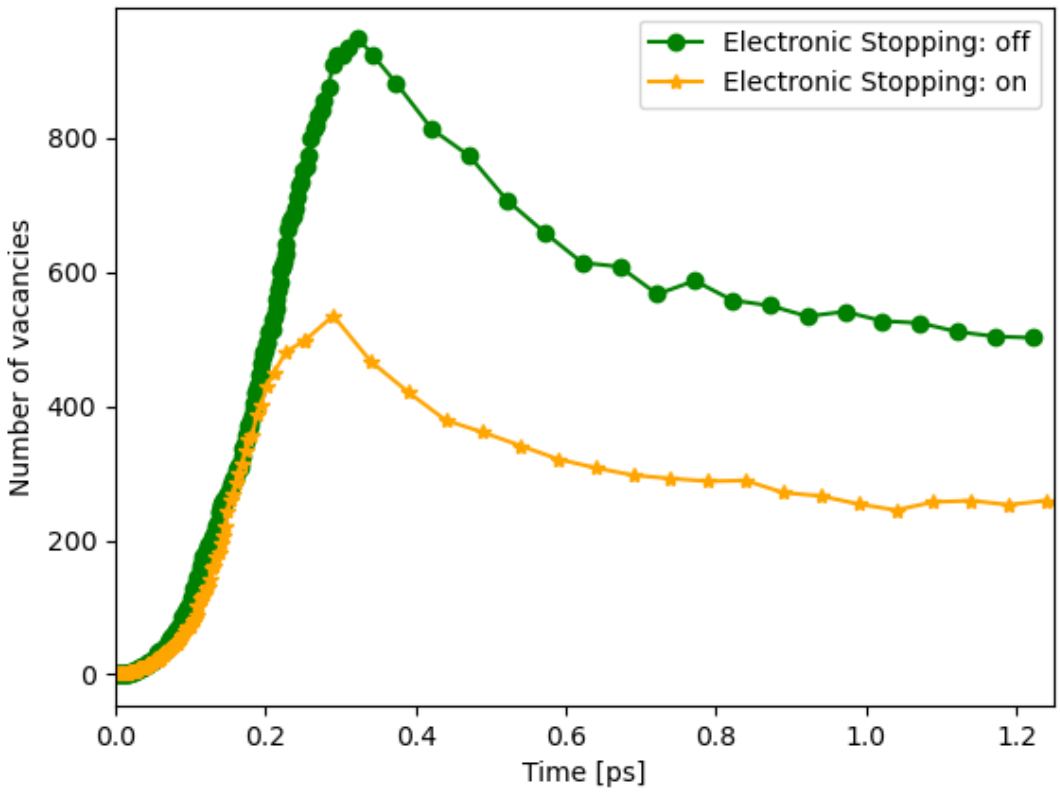

Figure 4.24: Number of vacancies after 20 keV Ar irradiation of 3C-SiC with and without accounting of electronic stopping power effects of ion velocity.

4.3.8 Heating

Heating of the SiC sample with 27000 atoms was performed using fix heat. SiC sample was previously heated to 300 K and equilibrated. Fix heat add kinetic energy to a group of atoms. Here, the added energy flux was 6966 eV ps^{-1} and this value is equivalent to a studied sample temperature increase ratio of 1000 K ps^{-1}. The simulation total time was 10 ps with a timestep equal to 0.001 ps. Fig. 4.25 shows the crystal structure at the beginning of simulations when the crystal structure is perfect and at the end of simulations when Si and C atoms are mixed. The temperature and energy in a function of time are shown in Fig. 4.26 and in Fig.4.27, respectively. Defects in the crystal structure are presented in Fig. 4.28. The determined from the simulation temperature decomposition of the crystal structure of SiC is about 2500 K, while in lower temperatures (about 1500 K - at time 2.5 ps) defects can be created.

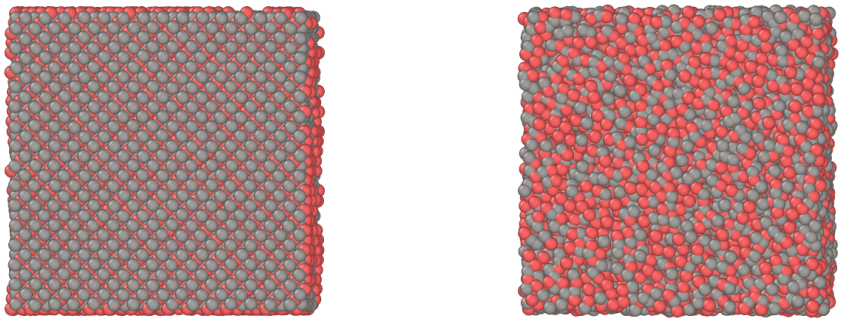

Figure 4.25: SiC sample at the start and at the end of the MD heating simulation.

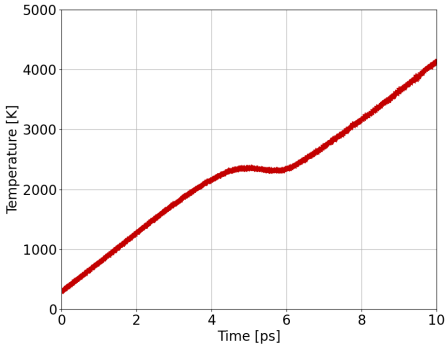

Figure 4.26: Tempreature evolution during the MD heating simulation.

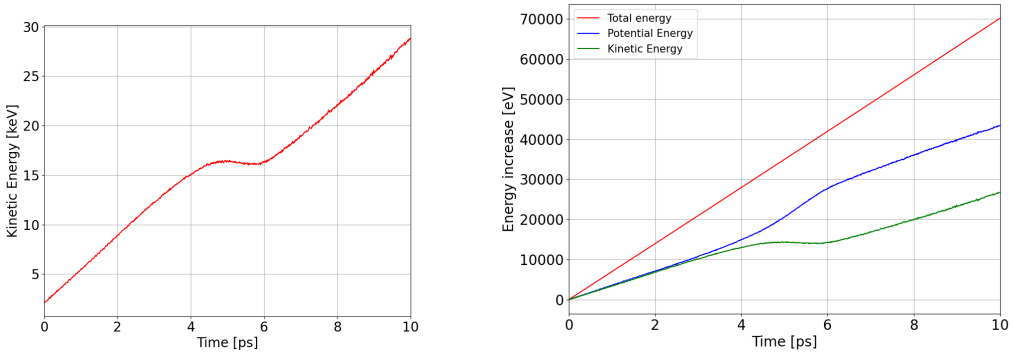

Figure 4.27: Energy increase during the MD heating simulation.

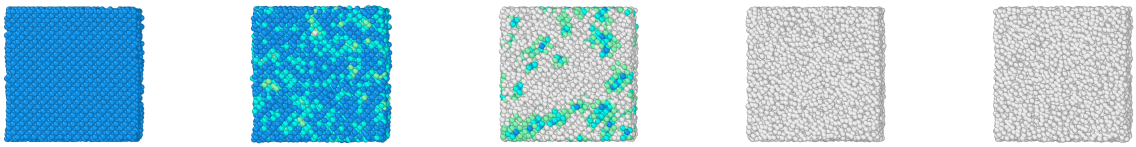

Figure 4.28: Identifying diamond structure (for time: 0.0 s, 2.5 ps, 5.0 ps, 7.5 ps and 10.0 ps)

4.3.9 Thermal Spike

Simulations of the electronic energy deposition during 21 MeV Si irradiation were investigated in MD by adding heat predicted by the thermal spike model to the lattice. Firstly, the atoms in the sample with the size of (1087.00 x 1087.00 x 65.22) Å were grouped into cylindrical zones (Fig. 4.29) differing in radius by 15 Å. The sample was equilibrated at 300 K by NPT ensemble (10 ps). For all simulations described in this subsection, periodic boundary conditions were used.

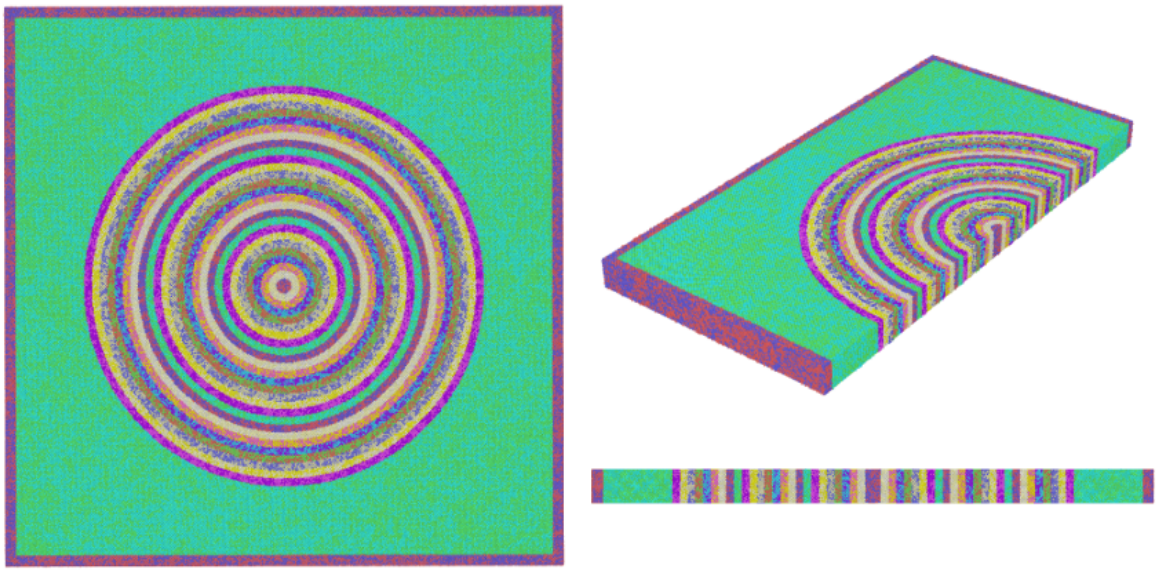

Figure 4.29: 3C-SiC sample divided into zones to reproduce the radial temperature distribution along ion path.

Energy per atom was calculated by Thermal Spike Gui 2.15 code with the lattice thermal conductivity equal to 0 and radius step equal to 15 Å. More details of the calculation are described in the previous section. Energy per atom was determined for the 21 MeV Si irradiation defects at a depth of 400 nm. Simulations were performed of λ equal to 5.6 nm (correspodning to g equal to $g = 6 \cdot 10^{12}\,\mathrm{W\,cm^{-3}\,K^{-1}}$) and λ equal to 1.4 nm (corresponding to g equal to $10^{14}\,\mathrm{W\,cm^{-3}\,K^{-1}}$). To determine the heat that should be added to each group of atoms, the energy per atom was multiplied by the number of atoms in each group.

The energy was deposited in atoms by fix heat. Heating was occurring with constant heat flux during 1 ps. The results are presented in Fig. 4.30.

It is shown that proper λ value may have a significant influence on simulation results. In case of λ equal to 5.6 nm the temperature in the ion path is below 1000 K and has no influence on the crystal lattice defects, while simulations with energy deposition predicted using λ equal to 1.4 nm show evidence of amorphisation of SiC lattice. Later on recrys-

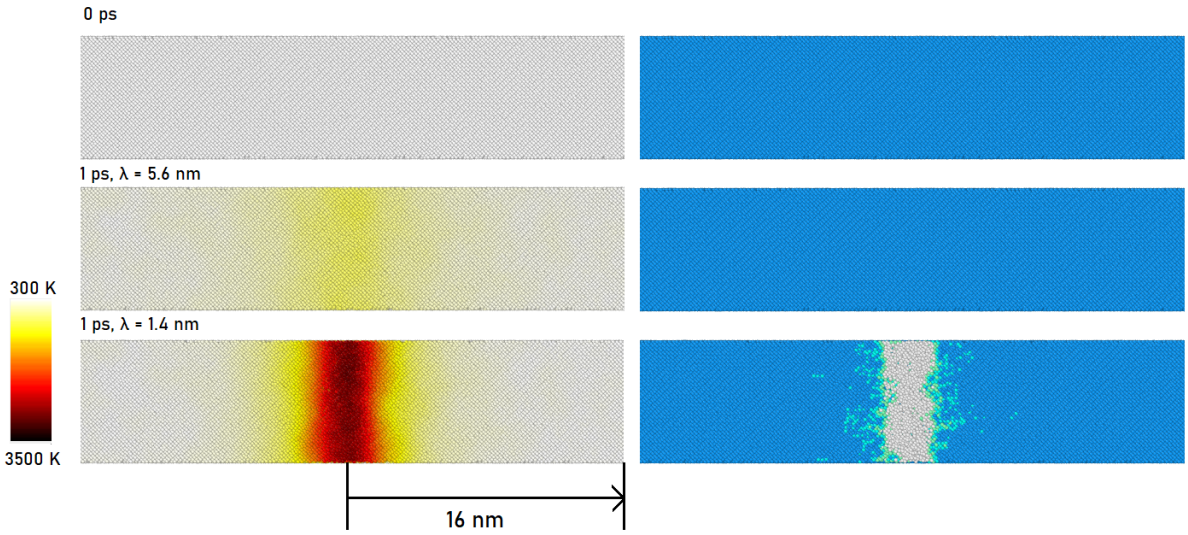

Figure 4.30: Temperature distribution and identifying diamond structure at the beginning (0 ps) and at the end of simulations (1 ps). Results are performed with $\lambda = 5.6$ nm and $\lambda = 1.4$ nm.

tallization may occur and finally no ion track can be found after 21 MeV Si irradiation. Recrystallization is a process strongly time-dependent, thus, this investigation is left for future recommendation. In this work, the evidence of possible amorphization of SiC is presented. There is no clear answer to why defect repair occurs. One reason can be the annealing of defects and the second one is amorphization and subsequent recrystallization. There is an open question if annealing occurs in an extremely short time is enough for defect annealing.

4.4 McChasy code

The 'McChasy' code (Monte Carlo CHanelling Symulation) is a computational software developed by the National Centre for Nuclear Research for the interpretation of experimental data received from RBS/C to determine the depth distribution of defects [127] [128] [129], [130]. The 'McChasy' code uses Monte Carlo (MC) simulations to reproduce trajectories of He ions in crystalline structures.

McChasy simulates the ion passage through a sequence of layers of atoms in the investigated crystal and considers the interactions between the ion and atoms within each atomic layer. For the use of McChasy, a special structure preparation procedure is needed. An external dedicated program divides the investigated crystal into monolayers (atomic slices), based on atomic positions in the unit cell, lattice constants, crystallographic family space properties, and a desired orientation. Such a virtual cell, consisting of sliced atomic layers, is periodically repeated during the MC simulations to reproduce the full penetration depth of the RBS ion beam in investigating materials.

For the calculation of the ion interactions with several atoms from each layer, the Planar Scattering Approximation (PSA) is used. The ion interaction with atoms is calculated based on screened ZBL potential [50] [129].

The energy loss (dE/dx) calculations are based on the stopping power tables: 'trim' or 'rump'. Rump is a formula where a 6-parameter fit XRUMP-2000 is applied, while Trim data use TRIM data calculated by using the SR module [127]. There is also an option for adding correction for stopping-power and multiple dE/dx value by a factor $N\left(1-A\left(1-\frac{E}{E_0}\right)\right)$, where N and A are parameters specified by the user while E_0 and E are energies of the ion at the surface and in the target, respectively. Local energy loss is calculated based on the classical Lindhard approach, assuming that the stopping power is the sum of parameters: one dependent on the local electron density, and the second, the random. For calculation stopping power in compounds, Bragg's rule is applied (the linear addition of dE/dx) [128].

To model real conditions and include temperature influence, McChasy applies random displacements to equilibrium positions of structure atoms as thermal vibrations. These displacements are calculated in all three dimensions x_i using Gaussian distribution (Eq. 4.25) [129]. The standard deviation of the atoms in displacement u_i in the x_i direction. In the McChasy code, the amplitude of thermal vibration is a free parameter and should be fitted before considering defects in a sample.

$$T(x_i) = \frac{1}{\sqrt{2u_i^2}} \exp\left(-\frac{x_i^2}{-2u_i^2}\right) \tag{4.25}$$

To adequately fit the RBS/C spectra of irradiated samples, it is imperative to establish

predefined defect profiles before initiating the simulation process. In this study, structural defects were characterized and represented as randomly displaced atoms (RDAs).

Based on a defined RDA profile (expressed as atomic percentage vs. depth), McChasy applies a random displacement to a certain percent of target atoms during MC simulations. Simulation results can be then compared to the experimental data. If the simulated spectrum does not fit well the experimental one, the RDA profile has to be adjusted until a satisfactory fit is attained (trial-and-error procedure).

Chapter 5

Experimental study

5.1 Methods

5.1.1 SiC samples

In the present work, monocrystalline <100>-oriented 3C-SiC layers manufactured by Chemical Vapor Deposition on a Si substrate were used. The SiC layer has a thickness of 10.3 μm. The samples were prepared in the form of a single plate (wafer) with a diameter of 10 cm, polished and cut into 1 cm x 1 cm pieces by *NOVASIC* company, France (Fig. 5.1).

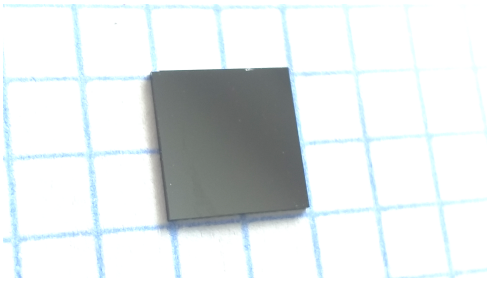

Figure 5.1: 1 cm x 1 cm sample ready for irradiation

5.1.2 Irradiation conditions

The experiment was conducted at the Helmholtz-Zentrum Dresden-Rossendorf (HZDR) in Dresden, Germany. Samples were irradiated with Si and C ions using the Tandem accelerator. Implantations were done with various ion energies: 21 MeV, 5 MeV, and 500 keV for Si and 5 MeV, 1 MeV, and 500 keV for C ions, respectively. Fluences for irradiations (as numbered from 1 to 14 in Tab. 5.1) were selected to achieve doses corresponding to the value of 0.01 dpa determined at a depth of ~400 nm. The fluence and energy deposition calculations are presented in section 4.1. Irradiations labeled 15, 16, and 17 (in Tab.

5.1) were performed with increased fluence of Si ions in order to obtain more defects. The objective was to achieve for all of the energies (irradiation labeled 15, 16, 17) a dose of 0.05 dpa at a depth of 500 nm and for 0.5 MeV Si (labeled 17) a dose of 0.1 dpa at a depth 400 nm. Irradiation labeled 18 involved the use of 21 MeV Si ions on a SiC sample containing pre-existing defects, which were made using 0.5 MeV Si ions. Irradiations were performed at RT and HT of 800°C. To avoid channeling effects, implantation was carried out at 7 ° off the surface. The exception is irradiation with Si ions of 21 MeV energy, where three implantation angles (0 °, 7 °, 20 °) were used. As the SRIM-calculated maximum ion range in the experiment does not exceed 6 μm, the ions did not go beyond the SiC layer. The implantation chamber is shown in Fig. 5.4. The summary of experimental data is shown in Table 5.1.

Table 5.1: Experimental condition.

Number	Ion	Energy [MeV]	Fluence [cm^{-2}]	Temperature [°C]	Tilt angle
1	Si	21	$1.00 \cdot 10^{15}$	25	0^o
2	Si	21	$1.00 \cdot 10^{15}$	25	7^o
3	Si	21	$1.00 \cdot 10^{15}$	25	20^o
4	Si	21	$1.00 \cdot 10^{15}$	800	7^o
5	Si	5	$2.50 \cdot 10^{14}$	25	7^o
6	Si	5	$2.50 \cdot 10^{14}$	800	7^o
7	Si	0.5	$2 \cdot 10^{13}$	25	7^o
8	Si	0.5	$2 \cdot 10^{13}$	800	7^o
9	C	5	$2.00 \cdot 10^{15}$	25	7^o
10	C	5	$2.00 \cdot 10^{15}$	800	7^o
11	C	1	$4.0 \cdot 10^{14}$	25	7^o
12	C	1	$4.0 \cdot 10^{14}$	800	7^o
13	C	0.5	$1.5 \cdot 10^{14}$	25	7^o
14	C	0.5	$1.5 \cdot 10^{14}$	800	7^o
15	Si	21	$4.50 \cdot 10^{15}$	25	7^o
16	Si	5	$1.00 \cdot 10^{15}$	25	7^o
17	Si	0.5	$1.5 \cdot 10^{14}$	25	7^o
18	Si	0.5	$1.5 \cdot 10^{14}$	25	7^o
		21	$1.00 \cdot 10^{15}$	25	7^o

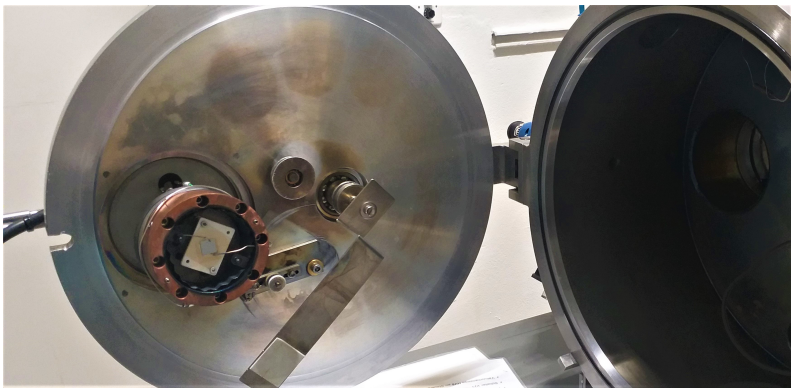

Figure 5.2: Tandem chamber with mounted 3C-SiC/Si sample.

5.1.3 RBC/S analysis

Samples were measured by Rutherford Backscattering Spectrometry in channeling mode (RBS/C). RBS/C is based on the scattering of light particles, such as He ions, with target atoms. The energy of the backscattered ions is measured and the depth profile in the crystal lattice can be determined.

RBS/C was done using a Van de Graaff accelerator with a beam of He ions with an energy of 1.7 MeV. The energy spectrum of the backscattered ions was measured by a silicon surface barrier detector at an angle of 170 ° off the initial ion beam direction. The samples were fixed with copper tape on the sample holder and placed in a vacuum chamber in the accelerator (Fig. 5.3).

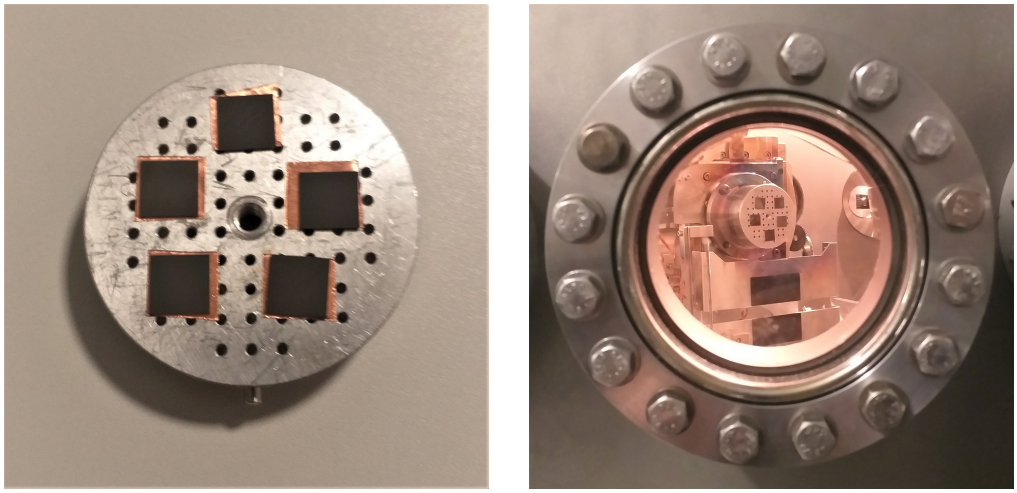

Figure 5.3: Si and C implanted 3C-SiC samples mounted on the sample holder (left) and the sample holder placed in the chamber (right).

The sample holder was mounted at the goniometer that provides rotation in 2-axis directions θ and ϕ (two mutually orthogonal planes) as well as the translate motion. For each sample, two types of spectra were recorded: random and aligned ones. Random

spectra were captured by tilting a sample at angles θ and ϕ of -4° off the normal to the surface and consequently changing one of them within the range (-4°,+4°) with a step of 0.2° while the other one was fixed at -4° or +4°, respectively. Such random measurements also allow the high-precision alignment of the sample along the ion beam by the indication of the main crystallographic planes. The sample orientation for the measurements in channeling mode (aligned spectrum) is determined by the values of the θ and ϕ angles corresponding to the intersection of the crystallographic planes. Due to the lower probability of a direct collision compared to the random orientation, a sharp drop in backscattering efficiency can be observed for aligned spectra. For further analysis, the aligned spectra are important because they provide quantitative information about the disorder of the crystals. Hence, RBS/C analysis allows the evaluation of defect profiles after irradiation. The energy spectrum carries information about the energy transfer during the collision and consequently about the depth profile as additional energy loss occurs in the form of electronic stopping power.

5.2 Results

5.2.1 As-grown sample

The RBS/C aligned and random spectra for the as-grown sample were measured and subsequently employed as a baseline reference. These reference spectra are shown in Fig. 5.4. The signal from the surface of Si and C lattice is very well visible due to different masses of the elements. The maximum energies of He ions backscattered at the surface are 419,29 keV for C and 958,49 keV for Si ions, respectively. The ions backscattered in deeper regions are subject to energy loss, hence, will be detected with lower energies.

The crystalline quality of the as-grown sample was evaluated by calculating the minimum yield χ_{min}, which is the ratio of the backscattering yield for the aligned spectrum to the random one (Eq. 5.1). χ_{min} is less than 3 % which indicates good quality of the crystal. The value of χ_{min} was calculated for the energy range from 850 keV to 950 keV.

$$\chi_{min} = \frac{Y_{aligned}^{as-grown}}{Y_{random}} \tag{5.1}$$

MC simulations in the McChasy code were used to extract defect profiles in the implanted samples. However, the code was first applied to fit the spectra recorded for the as-grown sample as a reference. Figure 5.5 shows the results of the McChasy simple random calculation (i.e., without MC simulations - only energy loss values are applied within the depth) with different formulas for electron stopping calculation. It is evident that

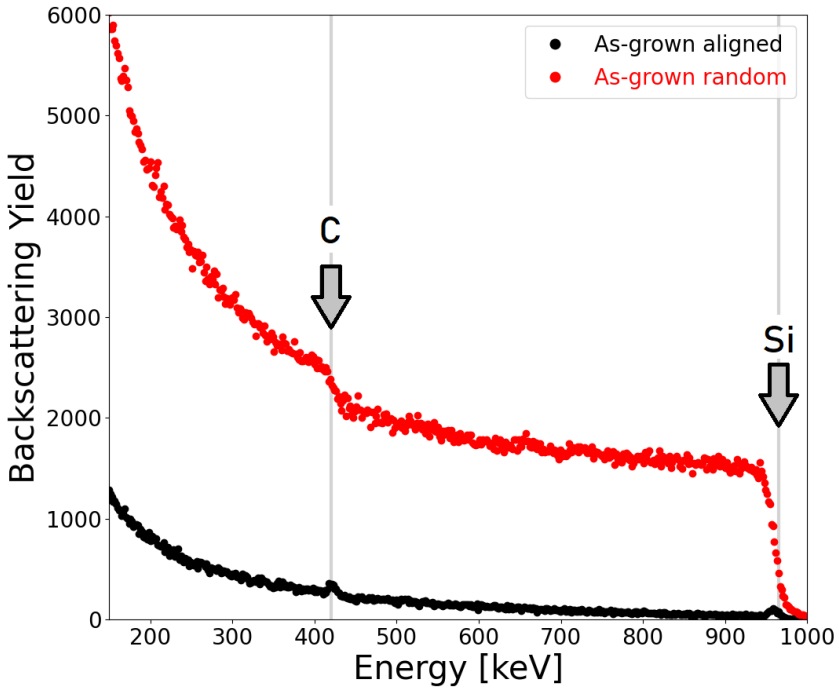

Figure 5.4: RBS/C aligned and random spectra of the as-grown sample. The grey vertical line corresponds to the surface of C and Si.

'trim' stopping power provides the best match for the experimental spectra. Additional dE/dx corrections (with parameters: N = 1.17 and A = 0.25.) were also added to better fit McChasy spectra to the experimental one.

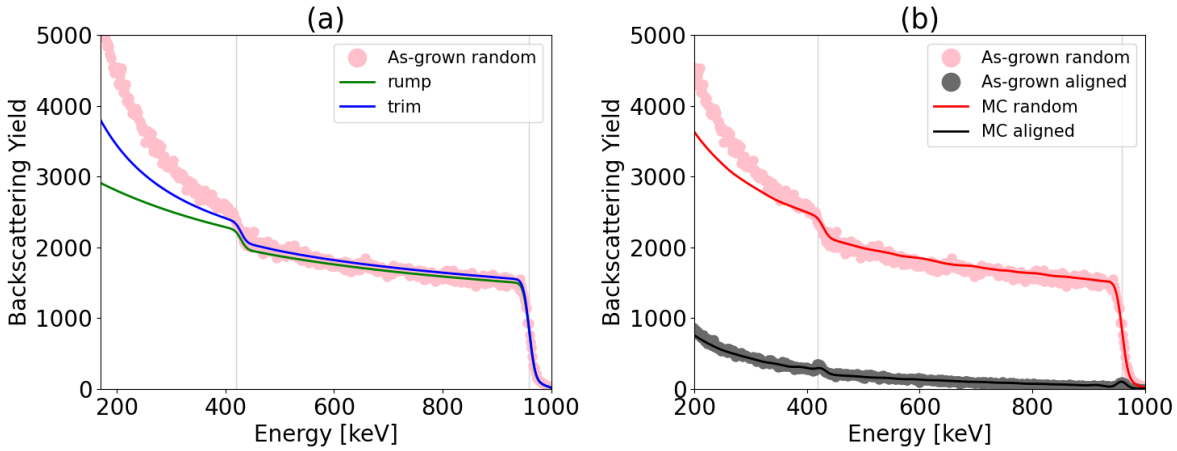

Figure 5.5: McChasy simple random calculations with different stopping power library (a), and finally fitted MC spectra (b).

The fitted amplitudes of thermal vibration values are 6.5 pm for Si and 16 pm for C. The final result of the performed fitting is shown in Fig. 5.5b. MC simulations were performed with 90000 particles to obtain high statistics and relatively smooth simulation

spectra. For low energies that correspond to deeper layers, a weaker fit is evident. Thus, for the deeper layer, the error of the results increases. Subsequent simulations presented in this Chapter were performed with the addition of RDA defects to the input for the simulation of defective crystal structure.

5.2.2 Different tilt angles

Irradiation of the first three samples was performed at different tilt angles: 0 °, 7 °, and 20 ° using 21 MeV Si ions. RBS/C spectra of these three samples after irradiation is presented in Fig. 5.6. The backscattered yield has the highest values for irradiation at 7 °. The results indicate the validity of using a tilt angle of 7 ° to prevent undesired channeling during Si and C irradiation. This demonstrates that, notwithstanding the irradiation with a small dose, the disorder can be noticed.

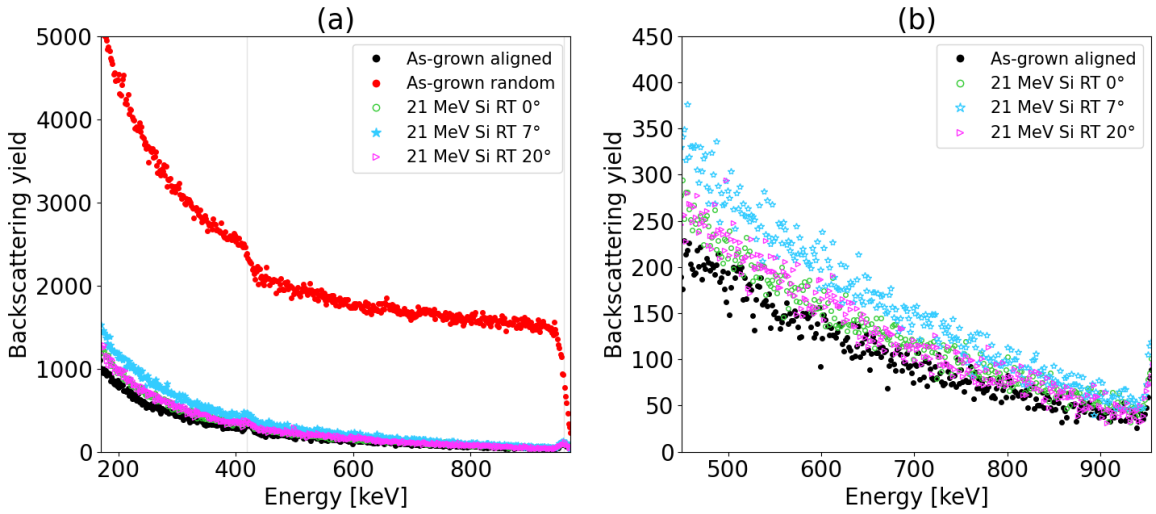

Figure 5.6: RBS/C spectra of 21 MeV Si irradiated samples (0 °, 7 ° and 20 ° tilt angles). The grey vertical line corresponds to the surface of Si and C.

The damage created by 21 MeV Si ion irradiation was evaluated by a factor called relative defect fraction (f_D) given by equation 5.2. Here, f_D is calculated as an average value for every 25 nm depth layer.

$$f_D = \frac{Y_{aligned}^{irradiated} - Y_{aligned}^{as-grown}}{Y_{random}} \tag{5.2}$$

Fig. 5.7 shows the Relative Defect Fraction calculated for 21 MeV Si irradiated samples at different angles. Previous studies suggested that to some depth suppression of damage

can be observed [7] [79]. Here, the linear dependence of the Si-disorder can be observed from the surface.

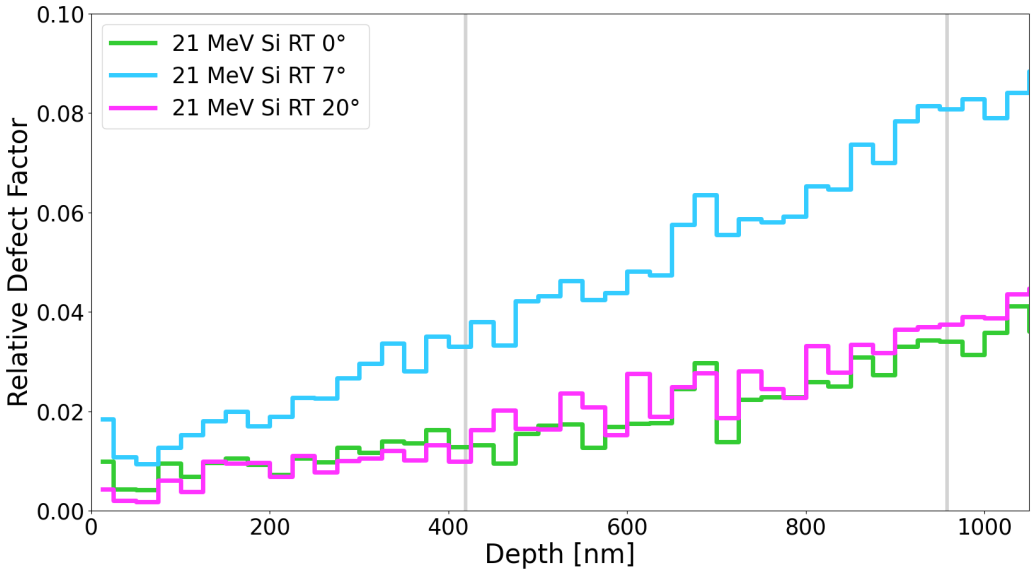

Figure 5.7: Relative Defect Fraction of 21 MeV Si irradiated samples (0 °, 7 ° and 20 ° tilt angles)

5.2.3 0.5 MeV Si and 0.5 MeV C irradiation

Fig. shows RBS/C spectra for irradiation using 0.5 MeV Si and 0.5 MeV C ions with the same fluence ($1 \cdot 10^{15}\,\mathrm{cm}^{-2}$). Si being heavier, has a shorter range, and causes greater damage than C.

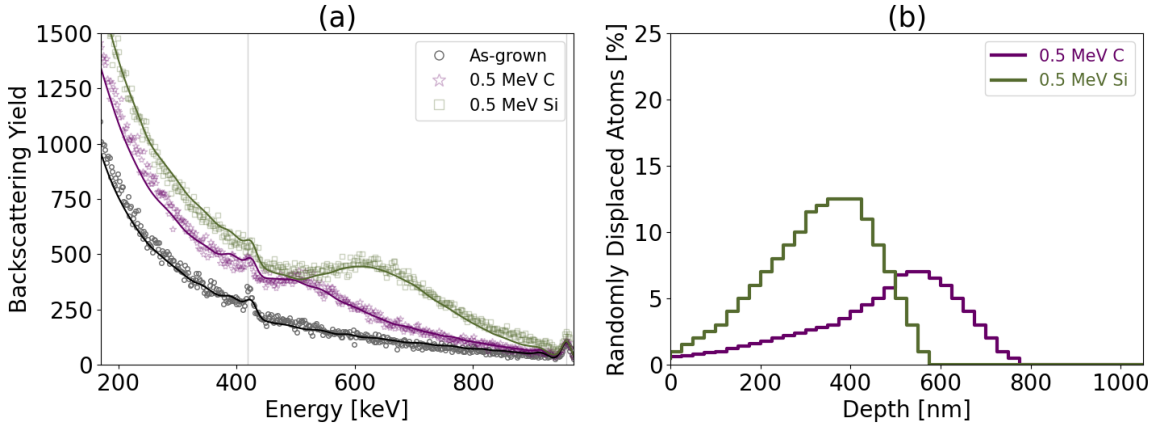

Figure 5.8: RBS/C spectra for 0.5 MeV Si and 0.5 MeV C irradiation with fluency $1.5 \cdot 10^{14}$.

This explains why different fluences were selected for irradiation as an assumption was to receive the same dose at a certain depth.

5.2.4 Low-dose irradiation

The SRIM code is a good tool for brief evaluation of the range of ions and damage profiles. From the calculations presented in Chapter 4.1, the irradiation fluences were determined to achieve 0.01 dpa at the depth of 400 nm. Therefore, the intersection of damage curves should be obtained at this depth. Randomly Displaced Atoms are determined by fitting results from the McChasy simulations of the backscattering yield. Results of simulations for Si and C irradiation at RT (with dose 0.01 dpa at depth 400 nm) are presented in Fig. 5.9. The damage profiles are in good agreement with those predicted by SRIM.

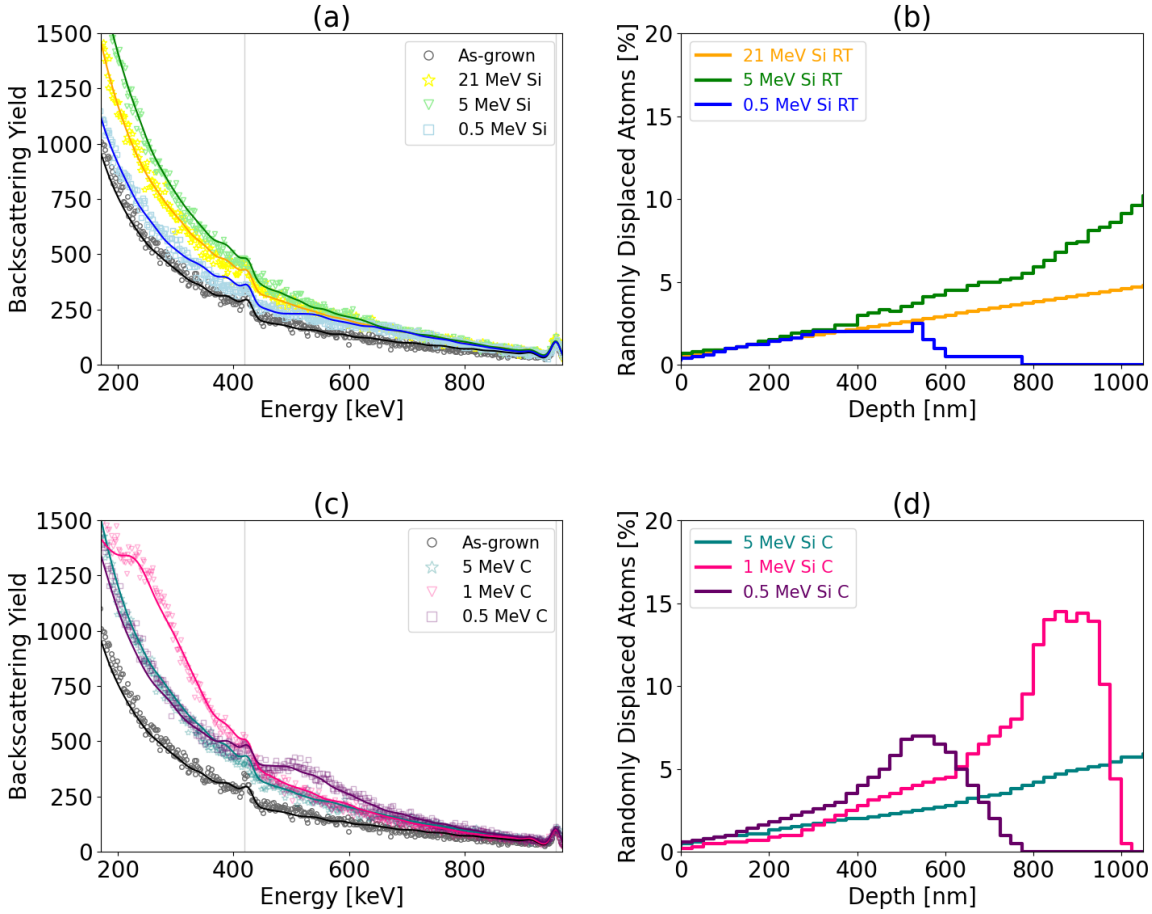

Figure 5.9: Channeling spectra simulated by McChasy code (a, c) and corresponding RDA profiles (b, d). Irradiation was performed to achieve dose of 0.01 dpa at a depth of 400 nm.

Irradiation with Si ions was performed with increased fluences in order to achieve the dose of 0.05vdpa in the same depth (500 nm). Fig. 5.10 shows RBS/C spectra with RDA

determined by MC simulations for irradiation with Si ions to achieve the dose 0.05 at the depth of 500 nm. When increasing the dose, it can be observed that the damage profiles do not conform to the expectations from SRIM calculations. At a depth of 500 nm, 21vMeV Si irradiation produces fewer defects than 5 MeVSi and 0.5vMeV Si.

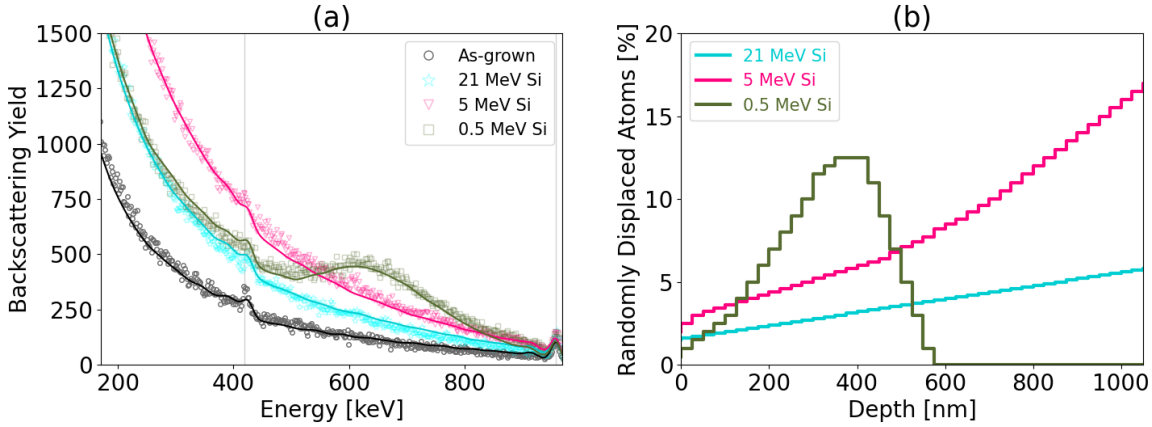

Figure 5.10: Channeling spectra simulated by McChasy code and corresponding RDA profiles for irradiation performed with Si ions (0.05vdpa at the depth of 500vnm)

These results indicate that for irradiation with 21 MeV Si, there is a reduction in defect formation with an increased flux. This can be explained by the thermal spike model. During 21 MeV Si passage through the material, temperature increases in a small cylinder around the ion path and may affect the dynamics of defects, potentially leading to the repair of previously formed defects and hence, partial recrystallization.

5.2.5 Temperature of irradiation

The temperature effects on Si and C irradiation are presented in Fig. 5.11. At RT, the damage was measured in each case. HT irradiation reduces damage that was measured after irradiation.

The irradiation temperature influences the formation of defects. In the case of SiC, this is clearly seen when comparing RT and HT irradiation. The HT temperature is close to the temperature that can be reached in the middle of the ion path. In this case, the formation of defects does not suggest that thermal spike effects are present and suppress the formation of defects. While previous studies have suggested that full supress can occur up to a certain depth [7] [79]. The increase in temperature according to the thermal spike model occurs in an extremely short time scale and within a limited radius. Recovery is limited to pre-existing damage.

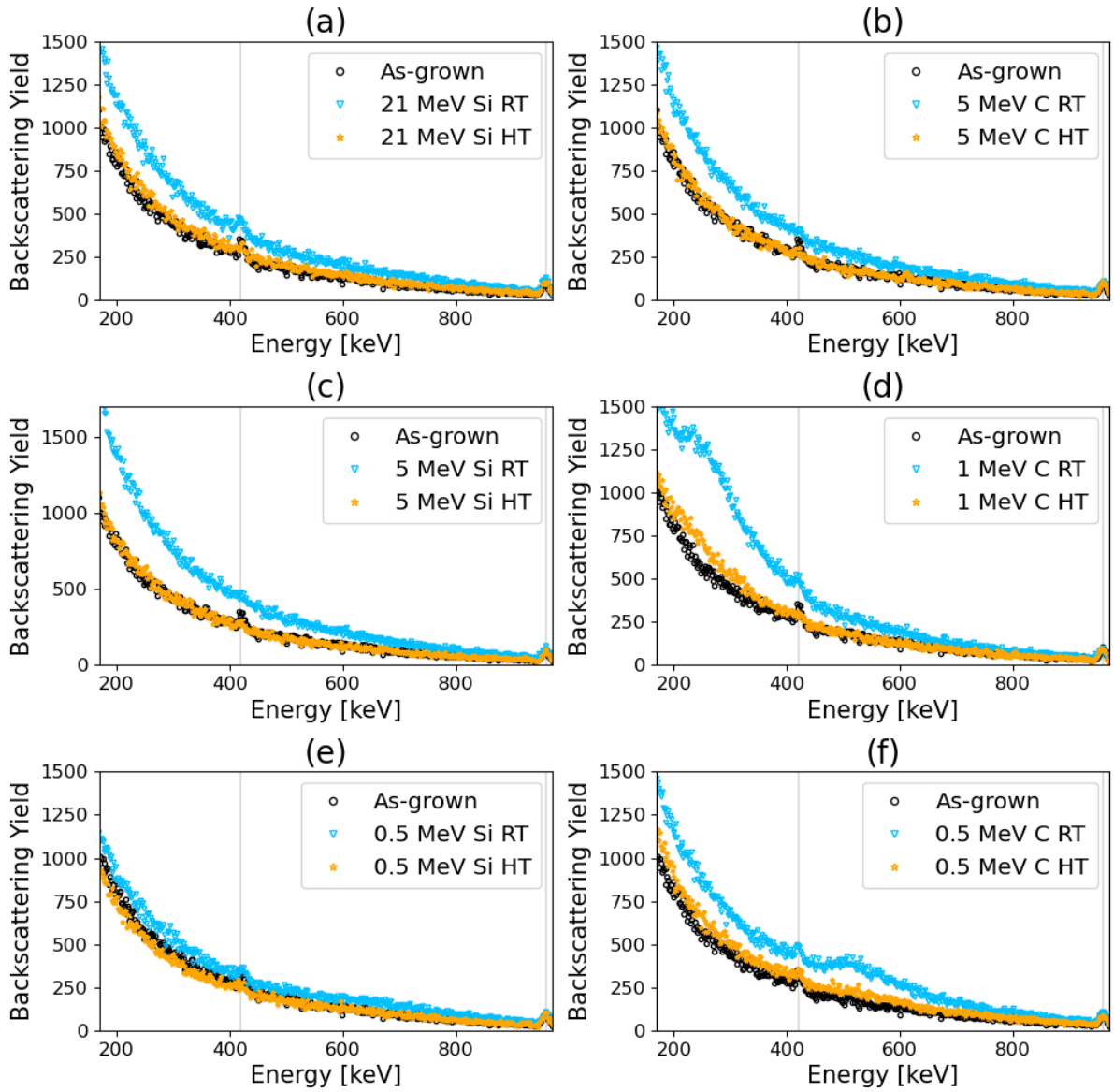

Figure 5.11: RBS/C spectra for irradiation at RT and HT. As a baseline, aligned spectra of as-grown samples are shown as black dots.

5.2.6 Thermal annealing

Fig 5.12 shows a thermally-induced recovery study made by annealing at 800 °C the as-grown sample and the sample damaged by 500 keV C ions. The samples were annealed during the same time as the irradiation time. Heating during irradiation gives the same effects in defect reductions as the annealing of the already irradiated sample. It can be observed that the sample with 500 keV C ion irradiation at RT followed by annealing at 800 °C has a similar RBS/C spectrum as the sample with 500 keV C ion irradiation at 800 °C. Dynamic annealing (during irradiation) led to the annealing of lattice disorder similar to the annealing after irradiation. The heating of the as-grown sample suggests a

small number of existing defects.

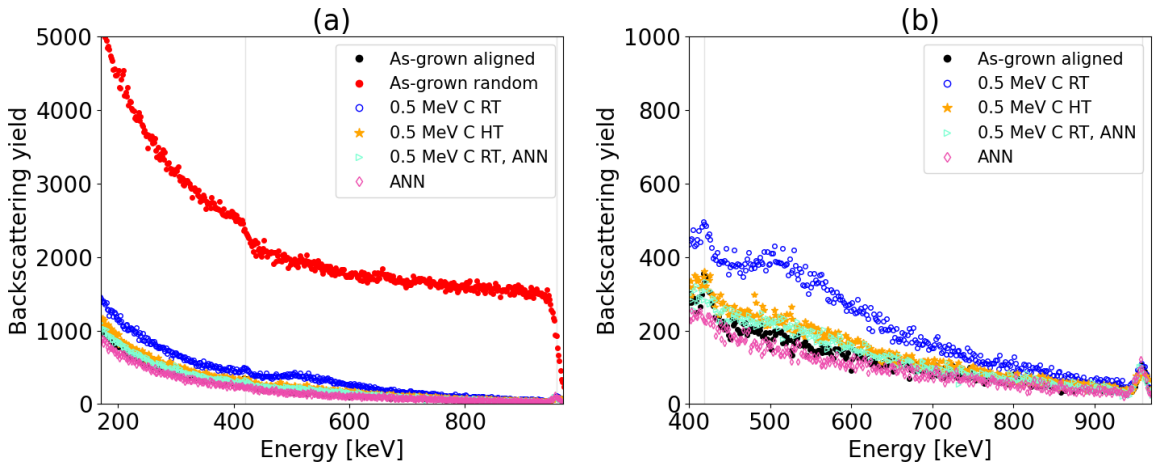

Figure 5.12: RBS/C spectra for different 500 keV C irradiation conditions. Blue dots denote irradiation at RT, whereas orange stars represent irradiation at HT. HT annealing after RT irradiation is represented by aquamarine triangles and HT annealing is represented by pink diamonds. Note that grey color lines correspond to the Si and C surface.

5.2.7 21 MeV Si irradiation of pre-damage sample

Pre-damage samples with 0.5 MeV Si ions were irradiated with 21 MeV Si ions (Fig. 5.13).

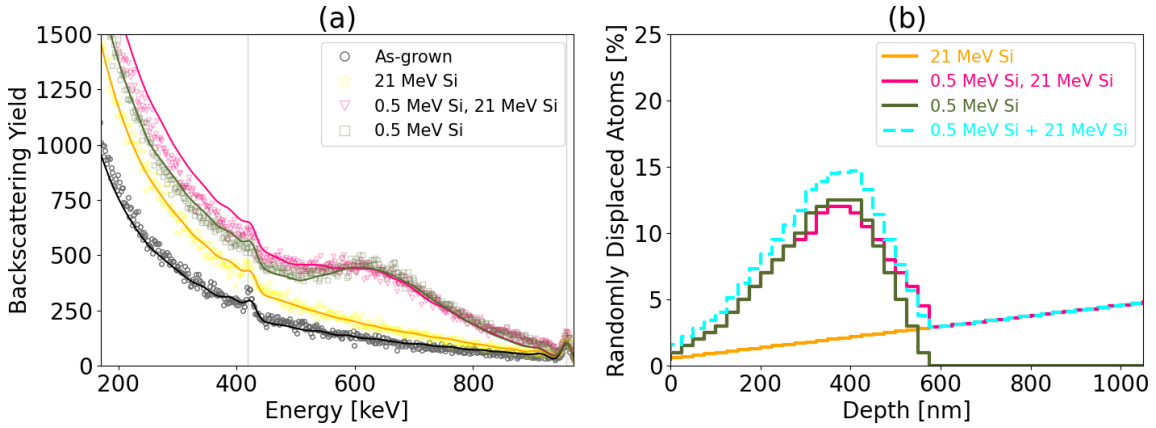

Figure 5.13: Channeling spectra for Si irradiation fitted by the McChasy code (a) and corresponding RDA profiles (b). The turquoise dotted stepline corresponds to the sum of RDA produced by 0.5 MeV Si and 21 MeV Si, separately.

Fig. 5.13b shows the RDA profiles determined from McChasy simulations for Si ion

irradiation and the sum of RDA predicted for 21 MeV Si and 0.5 MeV Si, separately. The total damage number does not increase after irradiation in depth range from 0 nm to 600 nm (corresponding to the range of 0.5 MeV Si). Analyzing Fig. 5.13, one can discern a potential reduction in the number of defects in regions where they were previously generated due to the previous ion passage. Nevertheless, it is apparent that at greater depths, 21 MeV ions induced defects. It looks like the repair mechanism occurs only in defective structures. The ionization annealing recovery occurs only when the structure is defective. In the shallow depth, there is no evidence of repair, only damage suppression occurs.

Chapter 6

Discussion

Silicon carbide has a wide range of applications in the nuclear industry, electronics and space. Due to its properties and many applications, the effects of SiC irradiation have been the subject of research for several decades. However, this is still not fully understood. A knowledge gap exists in the effects of electron energy deposition in intermediate energy regimes. Ionization-induced annealing may affect SiC damage or the electronic properties of SiC devices. Subsequently, it will have an impact on operational lifetime of SiC devices in nuclear reactors or space instruments. Therefore, it is important to improve understanding of this phenomenon.

Since one of SiC applications is in the nuclear industry, for example as a construction material for Dual Fluid Reactors or as a layer in TRISO fuel, the prediction of lifetime SiC devices in neutron radiation environmentally is very important. To reduce the cost and time of experiments for predictions the neutron radiation damage, ions can be used as surrogates of neutrons. For using ions to simulate neutrons the most important is to deeply understand the mechanism of production of defects, defects cluster, and also damage saturation conditions. Thus, the effects of ionization and excitation knowledge are crucial for modelling the neutron radiation effect using ions.

In this work investigation of the effects of electronic and nuclear energy deposition of ion irradiation damage production was performed. During irradiation incident ions deposit energy in the nuclei subsystem and electron subsystem. Deposition in the nuclei subsystem occurs during the ballistic collision and is the reason for the knock-off atoms from their lattice sites. Excitation and ionization is caused by the energy deposition in the electronic subsystem. Later on, the transfer of energy from electrons to atoms in the lattice can occur and lead to the heating of the ion path. This temperature increase has an influence on damage production and also on the recovery of already existing defects in the target. Previous studies have suggested that in SiC, ionization annealing effects can be caused by ions with energies as low as 450 keV. In this work, the electronic

energy deposition effects study in SiC for intermediate energy regimes was performed by experimental and computational methods.

According to the calculations based on the thermal spike model, it was determined that irradiation of SiC at both 300 K and 1075 K, using Si ions with the energy of 21 MeV and C ions with the energy of 5 MeV, which corresponds to the highest electronic stopping power, may not generate ion tracks in the SiC crystal due to insufficient temperature increase in the centre of the ion path, but may anneal defects in the lattice. Within the ion path temperature at the depth of 400 nm is greater than near the surface. However, at a depth of 400 nm, the temperature rises more significantly in the centre of the path but with a smaller radius.

The only free parameter in the thermal spike model is the electron-phonon coupling, In the case of SiC this can be deduced from the bandgap relationship, but it is an open question, whether this value is appropriate. The electron-phonon coupling may depend on the defects or the electron temperature. The simulations with different values of electron-phonon coupling were performed for 21 MeV Si. The simulations showed a very high dependence of the temperature that can be reached in the centre of the ion on the electron-phonon coupling. The temperature within the ion path exhibits an elevation with an increased electron-phonon coupling factor. The electron-phonon coupling depends on the number of defects in SiC. Therefore, in defective SiC structures, the effect of the thermal spike should be more significant. If the temperature causes repairs in the crystal lattice, greater repairs can be expected in the case of a more defective crystal.Moreover, amorphization and recrystallization can be expected for a defective structure.

The maximum reached temperature in the ion path dependence on the mean free path was also determined with the thermal spike simulation. The higher the mean free path lead to the higher the maximum electron temperature, and the dissipation of electron energy takes place over a longer time and a larger radius. The dissipation of electron energy into a smaller space leads to a higher lattice temperature. This is consistent with the theory that insulators are more sensitive to the effects of thermal spike than metals.

Molecular Dynamics simulations of heavy ion irradiation are still an open topic. This work demonstrates a solution for coupling thermal spike simulations and MD, but this research needs to be continued. Simulations of the passage of Si ions with the energy of 21 MeV through SiC were performed by heating the sample to the temperature calculated from the thermal spike model. Simulations show no changes for the pristine SiC. The temperature in the ion path is not sufficient to cause damage to the pristine SiC. Simulations were also performed with electron-phonon coupling values for defective structures. In this case, amorphization of the ion path occurs. In the future, simulations should be performed with damaged samples and the results for different electron-phonon couplings

should be investigated.

The thermal spike simulations for Si irradiation with an energy of 21 MeV show that the maximum temperature in the electron subsystem is reached within femtoseconds, while in the atomic subsystem, the maximum temperature occurs in the range of 10 fs - 100 fs. Collision cascade simulations with 5 keV Ar and 20 keV Ar show that the maximum peak damage occurs within less than 1 ps and within a few picoseconds equilibrium is reached with fewer defects than at the maximum. Exposure to higher temperatures reduces the number of defects at the end (after stabilization), but the maximum number of defects achieved is similar. Collision cascade occurs with a delay compared to thermal spike temperature increase.

The RBS/C method with the support of the McChasy code was used to analyze sample damage. The penetration range of the method was approximately 1050 nm. The damage peaks for 500 keV Si and 500 keV C were clearly visible, and the damage peak for 1 MeV C appeared close to the limit of the visible range. No damage peaks were observed for 21 MeV Si, 5 MeV Si, and 5 MeV C because they were created deeper than the maximum visible range. The damage and ion range profiles determined from the McChasy experiment are consistent with the SRIM predictions for low doses (0.01 dpa). It appears that with an increase in dosage (0.05 dpa), the number of defects caused by 21 MeV Si tends to reach saturation. The explanation is the thermal spike model.

Irradiation was performed at room temperature and at high temperatures. Results show evidence that high temperatures used during irradiation suppress damage production. The temperature during irradiation was similar to the temperature that can be reached in the centre of the ion path (determined by the thermal spike model). It can be seen that the temperature in the ion path may be sufficient to influence the dynamics of defects. As the time of thermal spike is extremely short and the area where temperature increases is small, the ionization-induced annealing can occur only in a small area and the fluence must be high to hit a defective place.

The defective SiC sample was additionally irradiated with 21 MeV Si (0.01 dpa). No damage produced due to the 21 MeV Si bombardment occurs from the surface to 600 nm. This may be evidence that a defective structure lead to a greater temperature increase in the ion path. Due to the small doses used in the experiment, it is necessary to repeat the experiment with higher fluencies.

Chapter 7

Conclusions

The main goal of the dissertation was to develop a physical understanding of ion radiation damage in SiC as an important aspect of using ion irradiation as a surrogate for neutron radiation damage. In the case of SiC, predicting damage from ion irradiation is complicated and depends on many parameters, especially when using ions in intermediate energy regimes (from several hundred keV to several 10 MeV), where annealing of defects or suppression of damage formation may occur.

Performed experiments show that it is possible to predict the defects produced by ion irradiation for low-dose irradiation. The doses predicted by SRIM make it possible to achieve the same number of defects at different energies at depths up to 400 nm. After increasing the dose, in case of 21 MeV Si, saturation of defects production can be observed. The mechanism of this phenomenon can be explained by the thermal spike model. Energy deposited in electrons can be transferred to the atoms heating the lattice in a small area around the ion path. If the energy is sufficient, defects annealing, or melting can occur. Furthermore, it has been observed that in the case of the irradiation performed on the pre-damaged structure, suppression of defects production and lattice repair can occur even at lower doses of 21 MeV Si irradiation. This suggests that defects can enhance the effects of thermal spike, which is also consistent with the results obtained from simulations. Thus, it is possible to use ions to simulate neutron damage in SiC, but the limits of the current state of knowledge about intermediate energy ions irradiation damage should be taken into consideration during planning experiments and interpretation of results. To avoid the effects of defect annealing or repair mechanism electronic energy loss should be relative low. Since SiC is a promising material for application in radiation environments, it is very important to develop models for damage calculations that account for possible annealing, reparation and the possible melting/recrystallization. The repair effects caused by ion irradiation support the use of SiC as a material for high-temperature reactors.

Performed research has shown how important it is to combine experiments with sim-

ulations. Future work should focus on experiments to see how the number of defects affects reparation efficiency, with simultaneous MD simulations. MD simulations should be used for investigation of the effect of the thermal spike on defective crystal structures, taking into account the dependence of electron-phonon coupling from a defect number. The simulation time should be extended to enable analysis of the lattice dynamics after heating, and the defects annealing efficiency or recrystallization.

List of Figures

List of Tables

Bibliography

1. Huke, A. *et al.* The Dual Fluid Reactor – A novel concept for a fast nuclear reactor of high efficiency. *Annals of Nuclear Energy* **80,** 225–235 (2015).
2. Huke, A. *et al.* in *Molten Salt Reactors and Thorium Energy* (ed Dolan, T. J.) 619–633 (Woodhead Publishing, 2017). ISBN: 978-0-08-101126-3.
3. Weibach, D., Sierchuła, J., Dąbrowski, M. P., Czerski, K. & Ruprecht, G. Dual Fluid Reactor as a long-term burner of actinides in spent nuclear fuel. *International Journal of Energy Research* **45,** 11589–11597 (2021).
4. Lewitz, J.-C. *et al.* The dual fluid reactor An innovative fast nuclear-reactor concept with high efficiency and total burnup. *Atw Internationale Zeitschrift fuer Kernenergie* **65,** 145–154 (2020).
5. Katoh, Y., Snead, L., Szlufarska, I. & Weber, W. Radiation effects in SiC for nuclear structural applications. *Current Opinion in Solid State and Materials Science* **16,** 143–152 (2012).
6. Zhang, Y. *et al.* Ionization-induced annealing of pre-existing defects in silicon carbide. *Nature Communications* **6** (2015).
7. Zhang, Y. *et al.* Coupled electronic and atomic effects on defect evolution in silicon carbide under ion irradiation. *Current Opinion in Solid State and Materials Science* **21,** 285–298 (2017).
8. Toulemonde, M. *et al.* in, 263–292 (2006). ISBN: 87-7304-330-3.
9. Dufour, C. & Toulemonde, M. in *Ion Beam Modification of Solids: Ion-Solid Interaction and Radiation Damage* (eds Wesch, W. & Wendler, E.) 63–104 (Springer International Publishing, Cham, 2016). ISBN: 978-3-319-33561-2.
10. Xue, H., Yanwen, Z. & Weber, W. In-cascade ionization effects on defect production in 3C silicon carbide. *Materials Research Letters* **5,** 1–7 (2017).
11. Jezierski, G. *Energia jądrowa wczoraj i dziś* ISBN: 978-83-7926-297-7 (Wydawnictwo WNT, Warszawa, 2014).

12. Semenov, B. *Nuclear power in the Soviet Union* https://www.iaea.org/sites/default/files/25204744759.pdf. Sept. 2023.

13. *The Power Reactor Information System (PRIS)* https://pris.iaea.org/pris/home.aspx. Sept. 2023.

14. *Nuclear Power Reactors in the World Reference Data Series* **2.** ISBN: 978-92-0-137123-2. https://www.iaea.org/publications/15485/nuclear-power-reactors-in-the-world (International Atomic Energy Agency, Vienna, 2023).

15. *Generation IV* https://www.gen-4.org/. Feb. 2023.

16. Mikulski, A. Zestawy krytyczne (reaktory mocy zerowej) w Instytucie Badań Jądrowych. *Postępy Techniki Jądrowej* **58** (4 2015).

17. Strupczewski, A. *Zaufajmy energetyce jądrowej* (PGE EJ 1 Sp. z o.o., Warszawa, 2016).

18. Uchwała nr 141 Rady Ministrów z dnia 2 października 2020 r. w sprawie aktualizacji programu wieloletniego pod nazwą "Program polskiej energetyki jądrowej". https://isap.sejm.gov.pl/isap.nsf/download.xsp/WMP20200000946/O/M20200946.pdf (2020).

19. Uchwała nr 215/2022 Rady Ministrów z dnia 2 listopada 2022 r. w sprawie budowy wielkoskalowych elektrowni jądrowych w Rzeczypospolitej Polskiej. https://monitorpolski.gov.pl/MP/2022/1124 (2022).

20. Possibilities for deployment of high-temperature nuclear reactors in Poland, Ministry of Energy, Warsaw. www.tiny.cc/htr-pl (2017).

21. Wrochna, G. *HTGR for heat market Plans in Poland* https://www.ncbj.gov.pl/sites/default/files/htgr_in_poland.pdf. 2019.

22. Zinkle, S. J. & Was, G. S. Materials challenges in nuclear energy. *Acta Materialia* **61.** The Diamond Jubilee Issue, 735–758 (2013).

23. Zinkle, S., Terrani, K., Gehin, J., Ott, L. & Snead, L. Accident tolerant fuels for LWRs: A perspective. *Journal of Nuclear Materials* **448,** 374–379 (2014).

24. Tan, Z. & Cai, J. Neutronic analysis of silicon carbide cladding accident-tolerant fuel assemblies in pressurized water reactors. *Nuclear Science and Technology* **30** (2019).

25. Guérin, Y., Was, G. & Zinkle, S. Materials Challenges for Advanced Nuclear Energy Systems. *MRS Bulletin* **34** (2009).

26. Dąbrowski, M. P. Reaktor dwupłynowy jako nowa i rewolucyjna koncepcja reaktora jądrowego. *Postępy Techniki Jądrowej* **3,** 25–32 (2018).

27. Sierchuła, J. *et al.* Determination of the liquid eutectic metal fuel dual fluid reactor (DFRm) design – steady state calculations. *International Journal of Energy Research* **43,** 3692–3701 (2019).

28. Weißbach, D. *et al.* Energy intensities, EROIs (energy returned on invested), and energy payback times of electricity generating power plants. *Energy* **52,** 210–221 (2013).

29. Bak, S., Hong, S. & Kadi, Y. Design of an accelerator-driven subcritical dual fluid reactor for transmutation of actinides. *Eur. Phys. J. Plus* **134** (2019).

30. Sierchuła, J. *Determination of the liquid eutectic metal fuel Dual Fluid Reactor design* PhD thesis. PhD thesis (2021).

31. Wang, X. *et al. Neutron physical feasibility of small modular design of Dual Fluid Reactor* in. **2019.27** (2019), 1229.

32. Böhm, D. *et al.* New Methods for Nuclear Waste Treatment of the Dual Fluid Reactor Concept. *Acta Physica Polonica B* **51,** 893 (2020).

33. Nowak, M., Spirzewski, M. & Czerski, K. Optimization of the DC magnetohydrodynamic pump for the Dual Fluid Reactor. *Annals of Nuclear Energy* **174,** 109142 (2022).

34. Elgendy, H. & Czerski, K. Numerical Study of Flow and Heat Transfer Characteristics in a Simplified Dual Fluid Reactor. *Energies* **16** (2023).

35. Hanusek, T. & Macian-Juan, R. Analyses of the shutdown system and transients scenarios for the dual fluid reactor concept with metallic molten fuel. *International Journal of Energy Research* **46,** 17230–17246 (2022).

36. Sierchuła, J., Dabrowski, M. P. & Czerski, K. Negative temperature coefficients of reactivity for metallic fuel Dual Fluid Reactor. *Progress in Nuclear Energy* **146,** 104126 (2022).

37. *DFR* `https://dual-fluid.com/resources/`. Sept. 2023.

38. Acheson, G. Production of artificial crystalline carbonaceous materials. *US patent: US492767A* **5 No. 492, 767** (1893).

39. Koyanagi, T., Katoh, Y. & Nozawa, T. Design and strategy for next-generation silicon carbide composites for nuclear energy. *Journal of Nuclear Materials* **540,** 152375 (2020).

40. Olesinski, R. & Abbaschian, G. The CSi (Carbon-Silicon) system. *Bulletin of Alloy Phase Diagrams 5, 486–489* (1984).

41. Katoh, Y. & Snead, L. L. Silicon carbide and its composites for nuclear applications – Historical overview. *Journal of Nuclear Materials* **526,** 151849 (2019).

42. Wang, F. F. & Zhang, Z. Overview of silicon carbide technology: Device, converter, system, and application. *CPSS Transactions on Power Electronics and Applications* **1,** 13–32 (2016).

43. Bausier, F., Massetti, S. & Tonicello, F. *Silicon Carbide for Space Power Applications* in *ESA Special Publication* (ed Ouwehand, L.) **719** (2014).

44. Zhang, X., Hu, H. & et al., X. W. Challenges and strategies in high-accuracy manufacturing of the world's largest SiC aspheric mirror. *Light: Science Applications* **11** (2022).

45. Millán, J., Godignon, P., Perpiñà, X., Pérez-Tomás, A. & Rebollo, J. A Survey of Wide Bandgap Power Semiconductor Devices. *IEEE Transactions on Power Electronics* **29,** 2155–2163 (2014).

46. Momma, K. & Izumi, F. *VESTA3* for three-dimensional visualization of crystal, volumetric and morphology data. *Journal of Applied Crystallography* **44,** 1272–1276 (2011).

47. Nordlund, K. *et al.* Primary radiation damage: A review of current understanding and models. *Journal of Nuclear Materials* **512,** 450–479 (2018).

48. Olander, D. R. Fundamental aspects of nuclear reactor fuel elements. `https://www.osti.gov/biblio/7343826` (1976).

49. Jóźwik, P. *Zastosowanie kanałowania jonów w analizie deformacji w kryształach* PhD thesis. PhD thesis (2017).

50. Ziegler J. F. Biersack J. P., Z. M. D. *SRIM: The Stopping and Range of Ions in Matter* ISBN: 9780965420716, 096542071X (Chester (Md.), 2008).

51. Norgett, M., Robinson, M. & Torrens, I. A proposed method of calculating displacement dose rates. *Nuclear Engineering and Design* **33,** 50–54 (1975).

52. Leay, L. & Harrison, M. T. Bubble formation in nuclear glasses: A review. *Journal of Materials Research* **34,** 905–920 (2019).

53. Szeflinski, Z. & Skrzypczak, E. *Wstęp do fizyki jądra atomowego cząstek elementarnych* ISBN: 83-01-11755-9 (Wydawnictwo Naukowe PWN, 1995).

54. Waligórski, M., Hamm, R. & Katz, R. The radial distribution of dose around the path of a heavy ion in liquid water. *International Journal of Radiation Applications and Instrumentation. Part D. Nuclear Tracks and Radiation Measurements* **11,** 309–319 (1986).

55. Schiwietz, G., Czerski, K., Roth, M., Staufenbiel, F. & Grande, P. Femtosecond dynamics – snapshots of the early ion-track evolution. *Nuclear Instruments and Methods in Physics Research Section B: Beam Interactions with Materials and Atoms* **225,** 4–26 (2004).

56. Toulemonde, M., Paumier, E. & Dufour, C. Thermal spike model in the electronic stopping power regime. *Radiation Effects and Defects in Solids* **126,** 201–206 (1993).

57. Toulemonde, M. *et al.* Material Transformation: Interaction between Nuclear and Electronic Energy Losses. *Procedia Materials Science* **7** (2014).

58. Backman, M. *et al.* Cooperative effect of electronic and nuclear stopping on ion irradiation damage in silica. *Journal of Physics D Applied Physics* **45** (2012).

59. Zarkadoula, E., Toulemonde, M., Weber, W. J., Science, M. & Technology Division Oak Ridge National Laboratory, O. R. T. Additive effects of electronic and nuclear energy losses in irradiation-induced amorphization of zircon. *Applied Physics Letters* **107** (2015).

60. Saifulin, M., O'Connell, J., Skuratov, V. & van Vuuren, A. J. Conicity of latent tracks in the near surface region as a factor affecting the correct evaluation of track size. *Physica Status Solidi C* **13,** 908–912 (2016).

61. Kamarou, A., Wesch, W., Wendler, E., Undisz, A. & Rettenmayr, M. Swift heavy ion irradiation of InP: Thermal spike modeling of track formation. *Phys. Rev. B* **73,** 184107 (2006).

62. Weber, W. J., Duffy, D. M., Thomé, L. & Zhang, Y. The role of electronic energy loss in ion beam modification of materials. *Current Opinion in Solid State and Materials Science* **19.** Ion Beam Modification of Materials, 1–11 (2015).

63. McHargue, C. J. & Williams, J. Ion implantation effects in silicon carbide. *Nuclear Instruments and Methods in Physics Research Section B: Beam Interactions with Materials and Atoms* **80-81,** 889–894 (1993).

64. Benyagoub, A. & Audren, A. Mechanism of the swift heavy ion induced epitaxial recrystallization in predamaged silicon carbide. *Journal of Applied Physics* **106** (2009).

65. Thomé, L. *et al.* Radiation Effects in Nuclear Ceramics. *Advances in Materials Science and Engineering* (2012).

66. Debelle, A *et al.* Characterization and modelling of the ion-irradiation induced disorder in 6H-SiC and 3C-SiC single crystals. *Journal of Physics D: Applied Physics* **43,** 455408 (2010).

67. Heft, A., Wendler, E., Bachmann, T., Glaser, E. & Wesch, W. Defect production and annealing in ion implanted silicon carbide. *Materials Science and Engineering: B* **29,** 142–146 (1995).

68. Zinkle, S., Skuratov, V. & Hoelzer, D. On the conflicting roles of ionizing radiation in ceramics. *Nuclear Instruments and Methods in Physics Research Section B: Beam Interactions with Materials and Atoms* **191,** 758–766 (2002).

69. Benyagoub, A. & Audren, A. Study of the damage produced in silicon carbide by high energy heavy ions. *Nuclear Instruments and Methods in Physics Research Section B: Beam Interactions with Materials and Atoms* **267,** 1255–1258 (2009).

70. Audren, A. *et al.* Effects of electronic and nuclear interactions in SiC. *Nuclear Instruments and Methods in Physics Research Section B: Beam Interactions with Materials and Atoms* **267,** 976–979 (2009).

71. Skuratov, V., O'Connell, J., Sohatsky, A. & Neethling, J. TEM study of damage recovery in SiC by swift Xe ion irradiation. *Nuclear Instruments and Methods in Physics Research Section B: Beam Interactions with Materials and Atoms* **327,** 89–92 (2014).

72. Thomé, L. *et al.* Recovery effects due to the interaction between nuclear and electronic energy losses in SiC irradiated with a dual-ion beam. *Journal of Applied Physics* **117,** 105901 (2015).

73. Debelle, A. *et al.* Ionization-induced thermally activated defect-annealing process in SiC. *Physical Review Materials* **3** (2019).

74. Debelle, A. *et al.* Combined experimental and computational study of the recrystallization process induced by electronic interactions of swift heavy ions with silicon carbide crystals. *Phys. Rev. B* **86,** 100102 (10 2012).

75. Chakravorty, A. *et al.* Recovery of ion-damaged 4H-SiC under thermal and ion beam-induced ultrafast thermal spike-assisted annealing. *Journal of Applied Physics* **130,** 165901 (2021).

76. Chakravorty, A. *et al.* Intense ionizing irradiation-induced atomic movement toward recrystallization in 4H-SiC. *Journal of Applied Physics* **128** (2020).

77. Backman, M. *et al.* Molecular dynamics simulations of swift heavy ion induced defect recovery in SiC. *Computational Materials Science* **67,** 261–265 (2013).

78. Abdelbagi, H. A. A. *et al.* Effects of swift heavy ion irradiation and annealing on the microstructure and recrystallizationof SiC pre-implanted with Sr ions. *Frontiers in Nuclear Engineering* **1** (2022).

79. Nuckols, L. *et al.* Coupled effects of electronic and nuclear energy deposition on damage accumulation in ion-irradiated SiC. *Acta Materialia* **199,** 96–106 (2020).

80. Was, G. S. Challenges to the use of ion irradiation for emulating reactor irradiation. *Journal of Materials Research* **30,** 1158–1182 (2015).

81. Predicting structural material degradation in advanced nuclear reactors with ion irradiation. *Scientific Reports.*

82. Zinkle, S. J. & Snead, L. L. Opportunities and limitations for ion beams in radiation effects studies: Bridging critical gaps between charged particle and neutron irradiations. *Scripta Materialia* **143,** 154–160 (2018).

83. Nelson, R., Mazey, D. & Hudson, J. The use of ion accelerators to simulate fast neutron-induced voidage in metals. *Journal of Nuclear Materials* **37,** 1–12 (1970).

84. Lewis, M., Packan, N., Wells, G. & Buhl, R. Improved techniques for heavy-ion simulation of neutron radiation damage. *Nuclear Instruments and Methods* **167,** 233–247 (1979).

85. Shao, L. *et al.* Standardization of accelerator irradiation procedures for simulation of neutron induced damage in reactor structural materials. *Nuclear Instruments and Methods in Physics Research Section B: Beam Interactions with Materials and Atoms* **409,** 251–254 (2017).

86. Röder, F. *et al.* Nanoindentation of ion-irradiated reactor pressure vessel steels – model-based interpretation and comparison with neutron irradiation. *Philosophical Magazine* **98,** 911–933 (2018).

87. Fluss, M. J., Hosemann, P. & Marian, J. in *Characterization of Materials* 1–17 (John Wiley Sons, Ltd, 2012). ISBN: 9780471266969.

88. Gilbert, M. & Sublet, J.-C. Differential dpa calculations with SPECTRA-PKA. *Journal of Nuclear Materials* **504,** 101–108 (2018).

89. Taller, S. *et al.* Multiple ion beam irradiation for the study of radiation damage in materials. *Nuclear Instruments and Methods in Physics Research Section B: Beam Interactions with Materials and Atoms* **412,** 1–10 (2017).

90. Hamada, S. *et al.* Development of a triple beam irradiation facility. *Journal of Nuclear Materials* **258-263,** 383–387 (1998).

91. Chen, Y. *et al.* Establishment of multi-beam irradiation facility at Wuhan University. *Nuclear Instruments and Methods in Physics Research Section A: Accelerators, Spectrometers, Detectors and Associated Equipment* **1040,** 167202 (2022).

92. Toader, O. *et al.* Technical Aspects of Delivering Simultaneous Dual and Triple Ion Beams to a Target at the Michigan Ion Beam Laboratory. *Physics Procedia* **90,** 385–390 (2017).

93. Kohyama, A, Katoh, Y, Ando, M & Jimbo, K. A new Multiple Beams–Material Interaction Research Facility for radiation damage studies in fusion materials. *Fusion Engineering and Design* **51-52,** 789–795 (2000).

94. Serruys, Y. *et al.* Multiple ion beam irradiation and implantation: JANNUS project. *Nuclear Instruments and Methods in Physics Research Section B: Beam Interactions with Materials and Atoms* **240,** 124–127 (2005).

95. Kaschny, J. *et al.* Facility for simultaneous dual-beam ion implantation. *Nuclear Instruments and Methods in Physics Research Section A: Accelerators, Spectrometers, Detectors and Associated Equipment* **551,** 200–207 (2005).

96. Brandt, W. & Kitagawa, M. Effective stopping-power charges of swift ions in condensed matter. *Phys. Rev. B* **25,** 5631–5637 (9 1982).

97. Weber, W. J. & Zhang, Y. Predicting damage production in monoatomic and multielemental targets using stopping and range of ions in matter code: Challenges and recommendations. *Current Opinion in Solid State and Materials Science* **23,** 100757 (2019).

98. Agarwal, S., Lin, Y., Li, C., Stoller, R. & Zinkle, S. On the use of SRIM for calculating vacancy production: Quick calculation and full-cascade options. *Nuclear Instruments and Methods in Physics Research Section B: Beam Interactions with Materials and Atoms* **503,** 11–29 (2021).

99. Devanathan, R., Weber, W. J. & Gao, F. Atomic scale simulation of defect production in irradiated 3C-SiC. *Journal of Applied Physics* **90,** 2303–2309 (2001).

100. Chang, J., Cho, J.-Y., Gil, C.-S. & Lee, W.-J. A simple method to calculate the displacement damage cross section of silicon. *Nuclear Engineering and Technology* **46,** 475–480 (2014).

101. Mieszczynski, C. *et al.* Defect evolution in Ni and solid-solution alloys of NiFe and NiFeCoCr under ion irradiation at 16 and 300 K. *Journal of Nuclear Materials* **534,** 152138 (2020).

102. Dufour, C. in. PhD thesis (1993).

103. Drowart, J., De Maria, G. & Inghram, M. G. Thermodynamic Study of SiC Utilizing a Mass Spectrometer. *The Journal of Chemical Physics* **29,** 1015–1021 (1958).

104. Snead, L. L. *et al.* Handbook of SiC properties for fuel performance modeling. *Journal of Nuclear Materials* **371,** 329–377 (2007).

105. Hermes, P. *et al.* Evaporation of atoms from femtosecond laser-heated gallium arsenide. *Applied Physics A* **39,** 9–11 (1986).

106. Houpert, C., Studer, F., Pascard, H., YunFan, J. & Toulemonde, M. Influence of the substrate temperature on the latent track damage cross section in magnetic insulators. *International Journal of Radiation Applications and Instrumentation. Part D. Nuclear Tracks and Radiation Measurements* **19,** 85–90 (1991).

107. Dufour, C., Beuneu, F., Paumier, E. & Toulemonde, M. Experimental evidence of the irradiation temperature effect in bismuth under swift heavy-ion irradiation. *Europhysics Letters* **45,** 585 (1999).

108. Meftah, A. *et al.* Experimental determination of track cross-section in Gd3Ga5O12 and comparison to the inelastic thermal spike model applied to several materials. *Nuclear Instruments and Methods in Physics Research Section B: Beam Interactions with Materials and Atoms* **237,** 563–574 (2005).

109. Al Smairat, S. & Graham, J. Vacancy-induced enhancement of electron–phonon coupling in cubic silicon carbide and its relationship to the two-temperature model. *Journal of Applied Physics* **130,** 125902 (2021).

110. Al Smairat, S. & Graham, J. The temperature-variable electron-phonon coupling and its role in the inelastic thermal spike in 3C-SiC. *Nuclear Instruments and Methods in Physics Research Section B: Beam Interactions with Materials and Atoms* **518,** 23–28 (2022).

111. Al-Smairat, S. Effects of vacancies and electron temperature on the electron phonon coupling in cubic silicon carbide and their connection to the inelastic thermal spike. *Doctoral Dissertations. 3143* (2022).

112. Leino, A. A. *et al.* GeV ion irradiation of NiFe and NiCo: Insights from MD simulations and experiments. *Acta Materialia* **151,** 191–200 (2018).

113. Thompson, A. P. *et al.* LAMMPS - a flexible simulation tool for particle-based materials modeling at the atomic, meso, and continuum scales. *Comp. Phys. Comm.* **271,** 108171 (2022).

114. *LAMMPS Molecular Dynamics Simulator* `https://www.lammps.org/`. 2021.

115. Stukowski, A. Visualization and analysis of atomistic simulation data with OVITO-the Open Visualization Tool. *Modeling and simulation in material science and engineering* **18** (2010).

116. Yan, Z., Liu, R., Liu, B., Shao, Y. & Liu, M. Molecular Dynamics Simulation Studies of Properties, Preparation, and Performance of Silicon Carbide Materials: A Review. *Energies* **16** (2023).

117. *OVITO, Wigner-Seitz defect analysis* `https://www.ovito.org/docs/current/reference/pipelines/modifiers/wigner_seitz_analysis.html`. 2023.

118. Maras, E., Trushin, O., Stukowski, A., Ala-Nissila, T. & Jónsson, H. Global transition path search for dislocation formation in Ge on Si(001). *Computer Physics Communications* **205,** 13–21 (2016).

119. Tersoff, J. Modeling solid-state chemistry: Interatomic potentials for multicomponent systems. *Phys. Rev. B* **39,** 5566–5568 (8 1989).

120. Gao, F. & Weber, W. J. Empirical potential approach for defect properties in 3C-SiC. *Nuclear Instruments and Methods in Physics Research Section B: Beam Interactions with Materials and Atoms* **191,** 504–508 (2002).

121. Ziegler, J. F. & Biersack, J. P. in *Treatise on Heavy-Ion Science: Volume 6: Astrophysics, Chemistry, and Condensed Matter* (ed Bromley, D. A.) 93–129 (Springer US, Boston, MA, 1985). ISBN: 978-1-4615-8103-1.

122. Samolyuk, G., Osetsky, Y. & Stoller, R. Molecular dynamics modeling of atomic displacement cascades in 3C–SiC: Comparison of interatomic potentials. *Journal of Nuclear Materials* **465,** 83–88 (2015).

123. Miller, R. LAMMPS Gao-Weber potential combined with a modified repulsive ZBL core function for the Si-C system developed by German Samolyuk (2016) v000. *OpenKIM* (2019).

124. Hirel, P. Atomsk: A tool for manipulating and converting atomic data files. *Computer Physics Communications* **197,** 212–219 (2015).

125. Braekken, H. Zur Kristallstruktur des kubischen Karborunds. *Zeitschrift fuer Kristallographie, Kristallgeometrie, Kristallphysik, Kristallchemie (-144,1977)* **75** (1930).

126. Vaitkus, A., Merkys, A. & Gražulis, S. Validation of the Crystallography Open Database using the Crystallographic Information Framework. *Journal of Applied Crystallography* **54,** 661–672 (2021).

127. Nowicki, L., Turos, A., Ratajczak, R., Stonert, A. & Garrido, F. Modern analysis of ion channeling data by Monte Carlo simulations. *Nuclear Instruments and Methods in Physics Research Section B: Beam Interactions with Materials and Atoms* **240,** 277–282 (2005).

128. Turos, A., Jozwik, P., Nowicki, L. & Natarajan, S. Ion channeling study of defects in compound crystals using Monte Carlo simulations. *Nuclear Instruments and Methods in Physics Research Section B: Beam Interactions with Materials and Atoms* **332,** 50–55 (2014).

129. Jozwik, P. *et al.* in *Theory and Simulation in Physics for Materials Applications: Cutting-Edge Techniques in Theoretical and Computational Materials Science* (eds Levchenko, E. V., Dappe, Y. J. & Ori, G.) 133–160 (Springer International Publishing, Cham, 2020). ISBN: 978-3-030-37790-8.

130. Jozwik, P. *et al.* Monte Carlo simulations of ion channeling in crystals containing dislocations and randomly displaced atoms. *Journal of Applied Physics* **126,** 195107 (2019).